uc3m | Universidad Carlos III de Madrid

DOCTORAL THESIS

Power and Frequency Control of an Offshore Wind Farm Connected to Grid through an HVDC Link with LCC-based Rectifier

Author:

Miguel Ángel Cardiel Álvarez

Supervisors:

Santiago Arnaltes Gómez
José Luis Rodríguez Amenedo

Tutor:

Santiago Arnaltes Gómez

Electrical Engineering, Electronics and Automation

Leganés, June 2018

A mi familia / To my family

Acknowledgements

My deepest gratitude goes to my supervisors Santiago and José Luis because of this opportunity and all their clear ideas and support. Thank you very much!

I also owe my gratitude to many other people. These people have helped me during my life. These people have shared with me not only very nice moments but also the difficulties that have arisen. These people have taught me plenty of things and are responsible for what I am nowadays. These people do not need their names to be written in this sheet of paper because these few words are enough for them to realize that my gratitude goes to them. Thanks a lot!

Abstract

There is an increasing interest in the use of line-commutated converter (LCC) technology to connect large offshore wind farms (OWFs) placed far from the coast by means of a high voltage direct current (HVDC) link. This is due to the better features of LCCs compared to voltage-source converters in terms of cost, reliability and efficiency. However, this technology requires a frequency control in the OWF to allow the operation of both the wind turbine generator systems (WTGSs) and the LCC rectifier. Therefore, this Thesis presents two frequency control proposals. First, a centralized voltage and frequency control for an OWF connected through LCC-rectifier-based HVDC link is proposed. It is derived from an enhanced LCC-rectifier station average-value model which indicates that the active power balance at the point of common coupling drives the OWF voltage while the corresponding reactive power balance drives the OWF frequency. Even though voltage control cannot be applied in case of using a diode rectifier, the voltage magnitude variation is clamped between acceptable values. As a second proposal, a decentralized frequency control for the diode-rectifier-based HVDC link connection of OWFs is also presented. This control is based on a reactive power / frequency droop which allows the WTGSs to reach synchronous operation and equally share the reactive power without the need of communications among the WTGSs. Moreover, the control proposals do not rely on a phase-locked loop, so controls are not subject to grid disturbances or measurement noise. Another important specification of the proposed control strategies is that they do not modify the active power control channel of the WTGSs. Finally, the stability and the simulation results to assess the performance of both control proposals are studied.

Contents

List of Figures

List of Tables

Chapter 1

Introduction

1.1 State of the art and motivation

There are several factors that have recently pushed renewable energies, being the most relevant one the contribution of greenhouse gas emissions to global warming. The concern about these emissions has brought some limitations on them which have turned into a significant growth in renewable energies [1]. This growth can be appreciated nowadays, given that global renewable power capacity was increased by near 9 % in 2016 [2]. In fact, the aforementioned increment becomes higher than 17 % if the well-known and well-established hydropower renewable energy is not considered.

Renewable energy capacity is led by wind power capacity just after hydropower capacity [2]. This impact reveals not just its relative importance among the renewables but also its global influence in electricity production. Moreover, wind power is recently experiencing a growth which increases the global wind power installed as it can be extracted from the cumulative wind power capacity shown in Figure 1.1 [3].

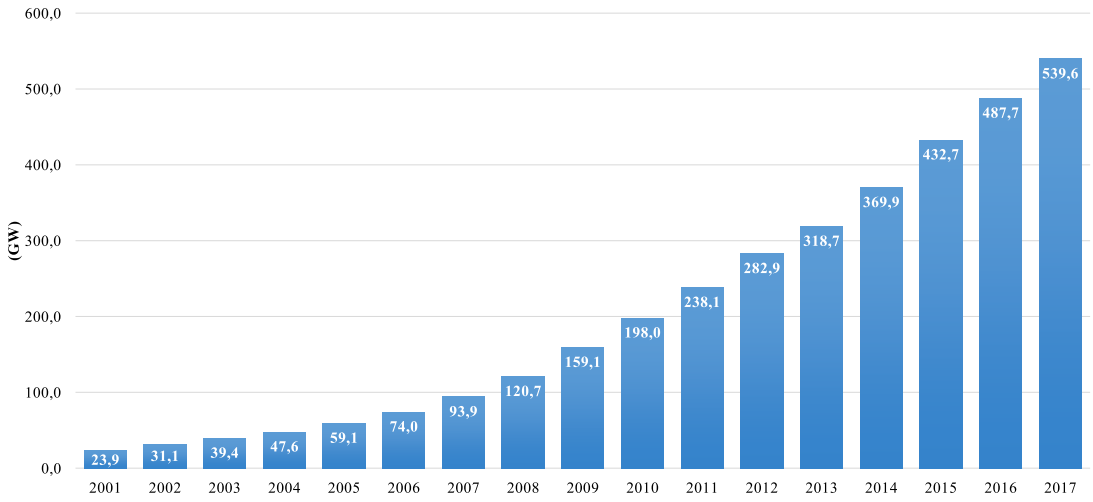

Figure 1.1: Global cumulative installed wind power capacity from 2001 to 2017.

Likewise, global annual wind power capacity increment is shown in Figure 1.2 [3]. The aforementioned increment depends on both the annual wind power installed and decommissioned. It shows that last four years are the best wind power installation years but it is worth mentioning that there is a decreasing trend in the last two years.

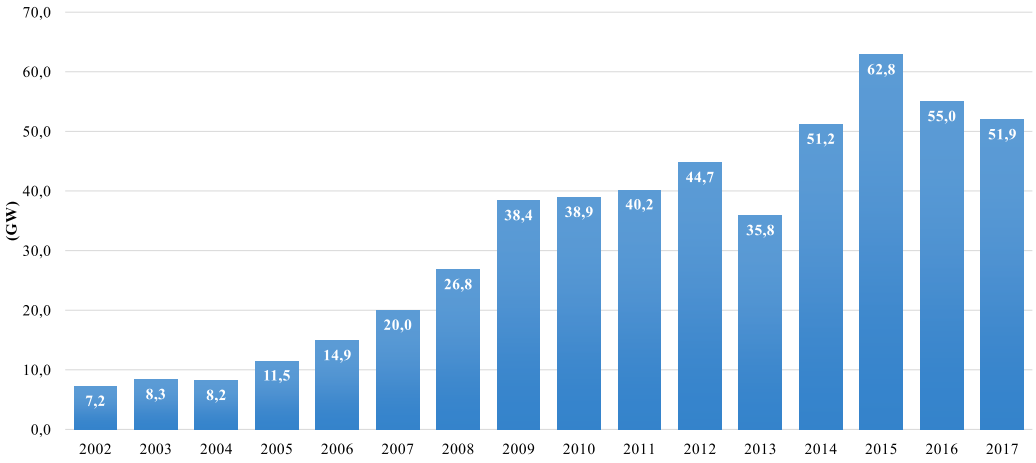

Figure 1.2: Global annual wind power capacity increment from 2001 to 2017.

1.1.1 Wind energy

Depending on the location, two different kinds of wind power plants can be considered: offshore and onshore. It should be pointed out that offshore wind energy is less mature than onshore wind energy given that the first commercial offshore wind farm (OWF) was installed in 1991 (in Denmark) [4]. Also, it is worth mentioning that the development patterns of these two wind energy technologies are different [5]. Even though annual wind power capacity increment has been reduced in the last years, this

is not the situation of offshore wind energy, which has grown in the last year. Namely, it has a global growing trend which is shown in Figure 1.3 [3].

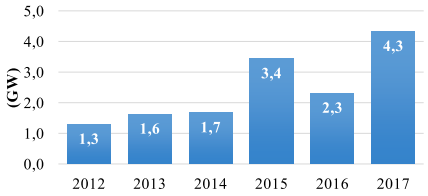

Figure 1.3: Global annual offshore wind power capacity increment from 2012 to 2017.

The comparison of offshore wind energy to onshore wind energy brings both the following main advantages and disadvantages of the offshore sites [1]. A first advantage comes from the location itself. Best onshore locations are already in use, although repowering projects can be relevant here. However, the sea provides larger suitable and free areas for wind power installation. In fact, this is probably the reason why annual wind power installed did not grow last year while installed offshore wind power grew. Moreover, due to the longer distance to populated areas, some wind energy drawbacks like the noise emission and the visual impact can be reduced. A second advantage corresponds to the resource quality because wind speed is generally higher and more consistent in the sea. Furthermore, onshore wind turbines are higher than their equivalent offshore ones due to the features of the turbulent-air layer close to the ground and the sea, respectively. Nevertheless, there are important disadvantages of offshore wind power. The main one is related to costs, which are bigger in offshore sites. Some reasons for this cost increment are, for instance, the corrosive environment, the fixed or floating wind turbine foundation, construction and operation and maintenance difficulties because of the accessibility problem, the integration to onshore and the higher separation between wind turbines because of the higher turbulences propagation compared to onshore sites. Regarding the economics of OWFs, studies show a big variability of its cost components with an increasing trend that seems to be stagnated for the vessels rental and the wind turbines acquisition [6].

As it can be extracted, offshore wind technology is still being developed and there are several ongoing research areas which will probably make OWFs be more cost-effective in the future. Specifically, this research work is focused on the integration of OWFs which are located far from the coast. Note that the increasing penetration level of offshore wind energy and high-power capacity of OWFs has recently made transmission system operators (TSOs) codes to increase the service requirements to OWFs, as it can be frequency support contribution, for instance. This has made some experts to start talking about offshore wind power plants (OWPPs), although the term OWF is generally used to refer to both concepts along this Thesis.

1.1.2 WTGS technology

It is worthy to give a brief overview of the main wind turbine generator system (WTGS) types [7, 8, 9], which can be also addressed as wind-energy conversion units (WECUs) and wind-energy conversion systems (WECSs). These systems are responsible for extracting the wind energy and converting it into kinetic energy and finally into electrical energy. First, squirrel-cage induction generators (SCIGs) were used with a multiple-stage gearbox and were directly connected to grid through a step-up transformer. It is a fixed speed concept which is addressed as type-1 WTGS. Then, fixed speed limitations were improved with the limited variable speed concept (Optislip), where variable rotor resistance and pitch control approaches were used. This is addressed as type-2 WTGS. Next, type-3 WTGS corresponds to a variable speed concept which uses an induction generator with a partial-scale power electronics converter that feeds the rotor winding, the doubly-fed induction generator (DFIG). This WTGS has been widely used because of its controllability while just a reduced power rating converter which is around 30 % of the WTGS rated power is needed. Finally, there are variable speed concepts with full-scale power electronics converter, where the alternating current (AC) part of the generator stator is completely decoupled from the AC grid. Typically, an electrically excited synchronous generator (EESG) or a permanent magnet synchronous generator (PMSG) is used with a single-stage gearbox or even without gearbox because of the use of a multi-pole machine with the corresponding reduced speed. These are addressed as type-4 WTGSs. Nowadays, wind power technology mainly uses type-3 and type-4 WTGSs, variable speed concepts which offer different advantages. The partial-scale converter makes type-3 cost be more attractive and it has lower power losses than the full-converter solution of type-4. However, type-4 WTGS avoids the brushes problems (failures and maintenance) of type-3 WTGS and it has a better control flexibility with a better fault ride-through (FRT) response [9] which helps provide the different TSO requirements for OWFs.

1.1.3 OWF interconnection technology: HVAC versus HVDC

Most promising areas for offshore wind power are located at long distances far from the shore, so long transmission lines are required for their interconnection. These interconnections can be accomplished by using two different technologies: high voltage alternating current (HVAC) and high voltage direct current (HVDC). The decision about the use of these technologies mainly depends on the transmission distance which affects the different cost components: lines, converters/platforms and losses [10]. Therefore, several studies have tried to establish the break-even distance which defines the length above which the most cost-effective technology is HVDC, as it is shown in Figure 1.4 [10]. There are many factors that affect this distance calculation, so different estimated values can be found. Nevertheless, it seems to be below 100 km [10, 11] for

marine transmissions, although some authors consider 50 km [12, 13, 14]. Therefore, HVDC is assumed to be the preferred technology for the connection of large OWFs which are located far from the coast [13, 15].

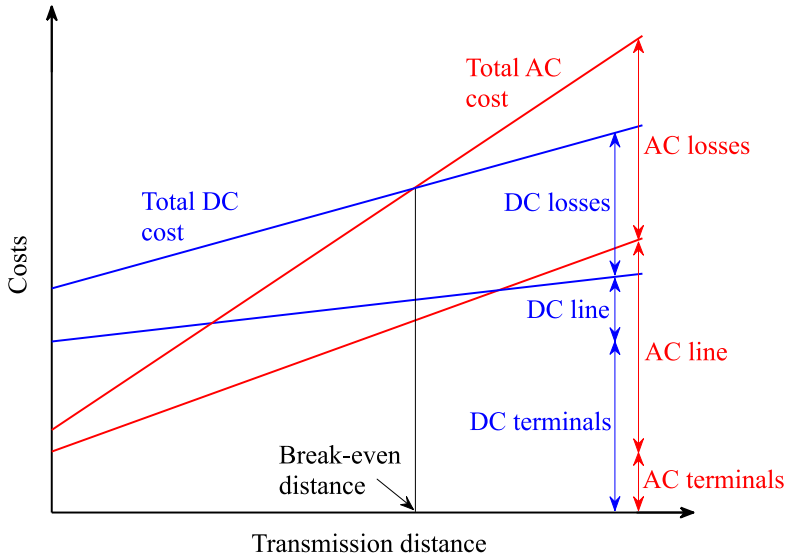

Figure 1.4: Dependence of HVAC and HVDC transmission costs on the distance.

1.1.4 HVDC technology: LCC versus VSC

This Thesis explores OWFs connected to onshore with HVDC transmission. Because of the direct current (DC) transmission, some researchers propose replacing the conventional AC collection offshore grid by a DC one [16, 17]. The main advantage of such a collection grid is the elimination of huge and heavy power transformers, which is quite interesting for marine applications. It allows us to omit half of the power electronics conversion in type-4 WTGSs, while it implies including converters in the other WTGS types, as it is established in [17]. However, the need of further research to overcome the DC protection drawbacks makes DC collection grids to be still under investigation [17].

This Thesis seeks an improvement for HVDC-connected OWFs which use the traditional AC collection offshore grid. These offshore grids are very likely isolated grids that need the corresponding voltage and frequency control in order to be operated. There are two kinds of HVDC transmission depending on the AC-DC conversion technology: line-commutated converter (LCC) and voltage-source converter (VSC). On the one hand, VSCs use self-controlled semiconductors which can belong to different types as turn-off thyristors (GTOs), being insulated gate bipolar transistors (IGBTs) the semiconductors used in most industrial applications [18]. The main advantage of VSC technology is its control flexibility which becomes quite important for OWF applications where it can provide the offshore AC grid (voltage and frequency) needed in such an isolated scenario. Moreover, the frequency spectrum of the AC waveforms requires

less filtering than LCC technology and it can be even unnecessary in the modern modular multilevel converter (MMC). On the other hand, traditional LCC technology uses thyristors. Although conventional LCC-HVDC links are made of thyristors, the unidirectional power flow of an OWF application suggests the possibility of using diodes in the HVDC rectifier converter, which also corresponds to a line-commutated converter. The disadvantage of LCC technology lies in its commutation nature which needs an AC grid (voltage and frequency) to provide AC-DC conversion during operation. LCC can operate connected to the AC grid in the onshore terminal of the HVDC link but not in the likely isolated offshore grid terminal. This implies that some means external to the HVDC link must be used in order to form and control the offshore AC grid voltage which is a challenge of this technology. It is worth mentioning that the offshore AC grid forming, during the startup, requires some active power which cannot be generally extracted from the HVDC link because of the unidirectional power flow nature of diode rectifiers. It is worth mentioning that the bidirectional power flow operation, which could be interesting for the startup of the OWF, requires reversing the DC voltage polarity while VSC just reverses the DC current. Furthermore, LCCs require huge AC filters which become quite important in marine applications where offshore substations are installed on platforms in the sea. Despite LCC drawbacks, this technology is superior to VSC technology in the following features [19]: maturity, reliability, efficiency, converter volume (converter footprint), cost and semiconductors overload capacity. Table 1.1 sumarizes the main advantages of both technologies LCC and VSC for OWF applications.

Table 1.1: Advantages of HVDC technologies: LCC versus VSC.

LCC	**VSC**
Lower cost	Black start / AC grid forming capability
Lower losses	Active and reactive power capability
Higher overload capacity	Smaller footprint (reduced filtering)
Longer experience and proven reliability	Bidirectional operation wihtout reversing DC voltage

LCC drawbacks are responsible for the absence of LCC-HVDC connected OWFs in the current offshore wind power scenario. Therefore, VSC is the current technology used for the interconnection of OWFs by means of HVDC links. However, LCC advantages have recently motivated the needed research in order to make this type of interconnection possible in a cost-effective way. Even though the huge passive filters imply a non-negligible drawback, most of the research has been focused on providing the voltage and frequency control required for the isolated OWF grid to which the LCC-rectifier is connected, which is the main challenge. Following, the state of the art of the different solutions which can be found in the literature is addressed.

1.1.5 LCC-HVDC connected OWF control solutions background

The different control proposals for the operation of OWFs with LCC-HVDC connection which can be found in the literature can be classified in two different categories: centralized control solutions and distributed control solutions.

1.1.5.1 Conventional centralized frequency control solutions

Beginning by the centralized control solutions, most of the proposed controls use an auxiliary static compensator (STATCOM) which is connected to the offshore AC grid in the offshore substation. This is the same bus where the LCC-rectifier is connected through its transformer. Namely, this offshore AC grid bus where all the OWF generated power is collected in order to be transferred to onshore is addressed as the point of common coupling (PCC) bus.

The control proposed in [20] uses a STATCOM which is controlled as a slack bus or infinite bus, *i.e.* it sets the voltage magnitude and the voltage angle at the PCC. It proposes to use the STATCOM DC voltage as a sensor to detect the imbalance in the active power generated by the OWF and the active power transmitted through the HVDC link. This imbalance is corrected by changing the thyristor firing angle which will modify the HVDC link current. Nevertheless, the use of the STATCOM DC voltage for detecting this active power imbalance is not realistic. This imbalance could imply important fluctuations, so a large STATCOM DC bus capacity is required in order to avoid unacceptable STATCOM DC voltage fluctuations. This proposal is a slight modification of the control proposed in [21]. The difference is that this proposal uses the dq-axes control of the STATCOM which seeks maintaining the PCC bus voltage oriented to the synchronous reference frame that rotates at the reference frequency. Therefore, the STATCOM seeks the PCC bus to behave as a slack bus. In [22] the control proposed in [21] is studied focusing on the STATCOM DC capacitor sizing needed. The same control principle for the STATCOM which is used in [21] is applied in [23, 24]. The control schemes are different and state feedback and a feedback compensator before applying proportional-integral (PI) controllers is used in [24]. It should be pointed out that in [23, 24] the startup of the offshore AC grid is addressed. Namely, a small auxiliary diesel generator which provides the active power required to maintain the STATCOM DC voltage during the startup is proposed. Later, the same authors in [24] propose an enhanced rectifier control that improves the power tracking of the rectifier and also the system damping after onshore grid faults [25].

The control solutions proposed in [26, 27, 28] present a voltage control which is implemented in the output of the type-3 WTGSs. Therefore, voltage control is a distributed control in a certain way. However, the frequency control is centralized and it is implemented by adjusting the active power balance at the PCC bus by adjusting the firing angle of the thyristor rectifier. The load-frequency relation drives this frequency

control and it does not imply that a load change will produce a frequency change, but the opposite. The load-frequency relation is a characteristic feature of the synchronous generator, where a frequency variation will produce a load variation and the opposite until the stable operation point is reached. Finally, [26] mentions that the offshore AC grid startup can be coordinated between the HVDC link and the type-3 WTGSs, but the procedure is just addressed and not specified. However, in [27, 28] a stand-alone operation of the type-3 WTGSs based on [29] is proposed to startup the grid before the frequency control starts operating.

It is worth mentioning that all the aforementioned control solutions use a thyristor rectifier in the HVDC link. In [30] the proposed control applies to the diode-rectifier HVDC connection of OWFs which can be composed of both type-3 and type-4 WTGSs. First, a type-3 WTGS voltage-source control based on [29] is proposed in order to be able to set the desired voltage magnitude and voltage phase in both types of WTGS. The well-known relations between active power and frequency and between reactive power and voltage magnitude present in conventional AC grids [31] are used for the control. Then, conventional active-power / frequency droop (P/f droop) and reactive-power / voltage droop (Q/V droop) controls are implemented in the voltage-source controlled WTGSs. However, both WTGS controls also use signals arriving from an OWF centralized controller. These signals cannot be instantaneous, so additional considerations about the communications needed are missing in this study. Finally, startup is accomplished by the WTGSs given their voltage-source control mode.

1.1.5.2 Hybrid HVDC-converter centralized frequency control solutions

Hybrid solutions can be also found in the literature. In [32], a DC parallel connection of a VSC and each of the two six-pulse diode rectifiers which would made a twelve-pulse rectifier if they were connected in series is proposed. In this control solution, the VSC is controlled as a slack bus. If no additional control is implemented, it is possible that there is power drawn by the rectifiers which is again injected to the offshore grid by the VSC. This power recirculation could take place in low power generation scenarios of the OWF which are not addressed in the publication and should be prevented by a control because of the power losses involved in the process. Similarly, a hybrid rectifier converter for OWF applications which consists of the DC series connection of a twelve-pulse diode rectifier and a VSC is presented in [33, 34] by the same authors in [32]. It is claimed that the VSC controls the PCC bus voltage magnitude and frequency. However, this converter is controlling the PCC bus voltage magnitude and its inner DC voltage, but not the frequency. A voltage-oriented control (VOC) [35, 36] to the PCC voltage is used, so it seems that it is assumed that there is frequency in the offshore grid because there is no control over the frequency in the VSC. In fact, the same authors present in [37] the same hybrid converter concept but assuming that there is voltage control in the offshore AC grid accomplished by the WTGSs, which appears

to be natural from the previous analysis. Therefore, the PCC bus voltage magnitude is controlled and the power transferred by the hybrid rectifier is set equal to the OWF generated power. In addition to establishing a substantially different hybrid rectifier control, a hybrid inverter with a twelve-pulse thyristor inverter connected in series to a VSC is proposed, which is the equivalent hybrid converter for the onshore inverter side. This way, a novel HVDC link based on hybrid VSCs for such an isolated application which helps reduce costs, power losses and footprint is claimed. Startup is only addressed in [37] among these hybrid solutions. Nevertheless, it is not significant because the proposed rectifier is not responsible for the offshore AC grid. Moreover, the proposals in [33, 34] use the VSC to filter the main harmonics of the twelve-pulse diode rectifier (11th- and 13th-harmonics) in order to reduce the passive filters required.

All the previous hybrid solutions have a DC capacitor connected in parallel to each of the diode DC outputs and to the VSC DC output. This feature means that if the dc-series-connected hybrid rectifier solution [33, 34, 37] is used to provide the OWF startup, the DC voltages balance would not be kept during the startup what would require at least overrating the maximum DC voltage of the diode units. These DC capacitors are removed in [38], where the DC-series connected rectifier is proposed to be made up of the twelve-pulse diode rectifier and a small MMC. This MMC is not proposed to control the offshore AC grid frequency which is controlled by the WTGSs. In fact, it only filters the DC voltage in normal operation in order to reduce the DC smoothing reactor while active power is transferred by the diode rectifiers. It is established that the startup process could be accomplished by the OWF WTGSs or by the hybrid rectifier. The latter implies setting a negative HVDC link voltage during the startup to allow the MMC to provide active power to the OWF with the required positive DC current imposed by the diode rectifiers, which would be disconnected from the offshore AC grid. This is not an easy procedure and it implies restoring the positive HVDC link voltage before starting to transmit power by the diodes. There are two different offshore AC grid voltage control options during this DC-voltage restoring time. On the one hand, the OWF could be able to operate in a stand-alone control mode during this DC-voltage restoring time, because the MMC and the link will be changing their DC voltage polarity thanks to the onshore inverter. On the other hand, The MMC could be keeping the offshore AC grid with its DC part disconnected from the HVDC link. This way, there is no control over the DC voltage of the MMC and its reconnection to the HVDC link could be complex.

Following the DC-parallel connected hybrid rectifier in [32], there is a similar proposal in [39] which uses thyristors instead of diodes. The VSC, which has a reduced DC voltage, provides the startup of the offshore AC grid while the thyristor rectifier is disconnected from the HVDC link. During normal operation, the VSC is in STATCOM mode with a Q/V droop together with the WTGSs and it provides active harmonic

filtering to its AC side. The offshore AC grid frequency control is carried out by modifying the firing angle of the thyristor rectifier, which is transferring the OWF power. Finally, there is a control shifting time when the thyristor rectifier must connect to a reduced DC voltage in the link, start transferring power and assume the frequency control while the VSC disconnects from the link and changes to STATCOM mode. This shifting time is mentioned but not discussed in the publication. Later, the control is modified in [40]. Specifically, the VSC control remains connected in operation, which eliminates the reduced VSC voltage advantage of the previous proposal. The VSC control is changed to be a slack bus and the thyristor rectifier follows current references.

1.1.5.3 Distributed control solutions

All the previous control solutions are centralized. Although some of them propose the WTGSs to startup the system or contribute to the offshore AC grid voltage control, this is not the target of a centralized control and they could be then considered as hybrid control solutions. A centralized control is supposed to provide the offshore AC grid to the WTGSs so they can operate by using the so-called VOC. This way, they inject active power depending on the wind conditions by following the WTGS power curve, which considers the maximum power point tracking (MPPT) control, if there is no power curtailment command [41] or deloaded operation to provide frequency support [42]. Regarding reactive power, WTGSs standard control modes are: reactive power reference, power factor reference and voltage reference [43]. Nevertheless, centralized solutions imply adding some power electronics to the PCC bus. Given that there is power electronics available in the most used type-3 and type-4 WTGSs, distributed solutions attempt the WTGSs to control the offshore AC grid. It is worth mentioning that most of the distributed control solutions use type-4 WTGSs because of their control flexibility advantage. Following, distributed approaches are addressed.

The control proposals which can be found in [44, 45] use single-WTGS aggregated models of the OWF to set the control principles of the distributed voltage and frequency control proposed in [46]. This control is performed in the WTGSs but it uses measurements at the PCC bus to orient the control. Therefore, this control cannot be entirely considered as distributed given the centralized measurements that are used. Moreover, these measurement signals should arrive via communication and this communication delay has a very important role given that the control would be oriented to an angular position which is different from the one that would be happening at that time. However, this communication delay is not considered. In addition, the angular reference is directly obtained from the PCC bus voltage components that are measured. As no dynamic tracking system as a phase-locked loop (PLL) is used, the voltage harmonic distortion is directly transferred to the WTGSs power control. The control includes the estimation of the quadrature component of the rectifier current and this estimation would not be as easy in the case of a real OWF which will have more than one

WTGS per string and π-models of the cables, for instance. Finally, [46] proposes to use the type-4 WTGS converters the following way. The front-end converter (FEC) or line-side converter (LSC) produces the desired AC voltage magnitude and angle while the back-end converter (BEC) or generator-side converter (GSC) controls the DC bus voltage. This modifies the conventional control of the wind turbine generator and its mechanical effects on the wind turbine should be studied.

The control proposed in [46] has been used for further studies. Namely, fault conditions and the efficiency of the solution are analyzed in [47], while an AC passive filters reduction is presented in [48]. Moreover, the integration of OWFs by means of diode-rectifier-based HVDC links to already existing VSC-based HVDC grids has been studied in [49, 50]. Finally, WTGSs are responsible for the offshore AC startup in [46], as they are also in [30].

A different control is proposed in [51]. It uses both the concepts of an active-power / voltage droop (P/V droop) and a reactive-power / frequency droop (Q/f droop). This control is an enhanced version of the control presented in [52] because the communications needed for the equal reactive power contribution of the WTGS used in [52] are eliminated. However, this control uses some principles of the one in [46] because WTGSs control also needs the measurements of the angular position and the frequency of the PCC bus AC voltage. This implies both several disadvantages addressed before and the need of communications for the control itself.

The authors in [53] present a control method which reduces the stability problems faced in weak offshore AC grids. These stability problems are directly related to the conventional PLL which is used for the VOC used in grid-connected converters [54, 55, 56]. The proposal consists of using a common fixed angular reference signal for the Park transformations in the control schemes of all the converters in the offshore AC grid, so the PLLs can be eliminated. This common fixed reference frame used for the converters synchronization is proposed to be obtained by a radio signal or the Global Positioning System (GPS) time signal. It is based on the injection of all the WTGS currents oriented to the fixed angular reference. This control method, which is initially proposed to be applied to VSC-HVDC connected OWFs, is also proposed to be used in case of a diode-rectifier-based HVDC link connection for the OWF. Specifically, it is presented for both type-3 WTGSs in [57] and type-4 WTGSs in [58], where a sinusoidal control is implemented in the converters. In [57], they address the startup problem, which is proposed to be done by an additional voltage supply. It can be feasible by an umbilical AC cable from onshore [59] or by the connection to a close OWF with a VSC-rectifier-based HVDC connection [60]. In [59], currents are injected in a synchronized way and the voltage magnitude is limited by the diode rectifier as it happens in the previous diode rectifier proposals. However, this control method injects currents and the offshore AC voltages are a result so there is no control over the reactive power of the WTGSs which could exceed the reactive power limits. In order to overcome

this drawback, the authors propose a droop control in [59] which helps approach the reactive power load of the different WTGSs but does not completely achieve a reactive power sharing. Finally, it is worth mentioning that this fixed reference frame approach does not have a decoupled control of active and reactive power in the WTGSs, given that the current vector is proyected to a vector which is not oriented to the terminal AC voltage.

The aforementioned fixed reference frame control approach seems to be one of the control proposals used by Siemens [61, 62]. This technology consists of the DC-series connection of diode rectifier units (DRUs) where the diode rectifier is embedded in the oil insulation of its input transformer. This way, a volume, cost and construction time reduction is claimed over conventional VSC-based HVDC connection of OWFs.

Siemens also presents a control for the DRUs solution in [63] which is based on [64]. This solution is not completely distributed because control commands are calculated as a function of both centralized and distributed measurements.

A new proposal based on PLLs has been recently presented in [65]. It uses a distributed Q/f droop control strategy which does not need communications and avoids the use of the GPS signal for synchronization. Moreover, P/V droop control is used during the startup which is proposed to be accomplished by the WTGSs to avoid the umbilical cable, but a specific procedure is followed to avoid the converters to exceed their power limits. However, as it has been previously mentioned, it is a PLL-based control which can be source of stability problems [54, 55, 56], which is the reason why the authors of the fixed reference frame looked for a more robust synchronization method. Moreover, they propose an active control of the MMC onshore inverter to improve the OWF power reduction response to an onshore AC fault.

As it can be extracted from the state of the art, there is an increasing interest in providing the diode-rectifier-based HVDC link solution the proper controls to be a feasible solution for the connection of future OWFs. The OWF control proposals analyzed from [30] to [65] (except [39, 40]) in the previous state of the art attempt a diode rectifier solution for the HVDC connection to onshore. In fact, the European Union supported the project PROMOTioN [66] which also has the DRUs among the proposals for large meshed offshore grids. The research on feasible and industrially-applicable control solutions for the diode-rectifier-based HVDC connection of future OWFs has motivated this Thesis work.

1.2 Objectives of the dissertation

The objectives of this Thesis are addressed following:

- To propose controls which overcome the drawbacks of diode-rectifier-based HVDC

links for the connection of OWFs which mainly implies providing startup capability and frequency control.

- To propose a centralized control for the LCC-rectifier-based HVDC connection of OWFs. This kind of control provides the offshore grid frequency, so any WTGS technology could be used without modifying the conventional controls.
- To propose a decentralized control for the diode-rectifier-based HVDC connection of OWFs. This kind of control avoids auxiliary power electronics converters in the offshore platforms and it should not modify the WTGSs active power control. Another requirement is to use a reactive power sharing strategy (QSS) which prevents the WTGS to exceed their reactive power limits, which can be achieved by assigning the same reactive power level to each of the WTGSs.
- To develop system models that allow the derivation or the justification of the proposed control strategies.
- To check the stability and evaluate the performance of the OWF when the proposed control strategies are applied.

1.3 Structure of the dissertation

The structure of this Thesis is summarized in the flow chart which is shown in Figure 1.5. In Chapter 2, the system under study for the connection of OWFs through LCC-rectifier-based HVDC links is presented. Then, it is defined how each of the elements in the system is modeled and an average-value model (AVM) of the LCC-rectifier station is proposed and validated. This proposed AVM will allow the derivation of the centralized control proposal and one of the control fundamentals of the decentralized control proposal. Moreover, the small-signal models are also provided in Chapter 2 when the elements are completely defined. Note that some elements will be completed by the control proposals in Chapter 3 and Chapter 4 and their small-signal models will be derived in those chapters.

Then, Chapter 3 presents the centralized voltage and frequency control for OWFs which are connected through LCC-rectifier-based HVDC links. According to the proposed AVM dynamic equations, the frequency and voltage control strategies are derived and presented. If a diode rectifier is used, just frequency can be controlled and it is demonstrated that the voltage magnitude is clamped between acceptable limits. However, the use of a thyristor rectifier allows both voltage and frequency to be controlled. Then, each of the solutions are evaluated in Chapter 3: diode rectifier with frequency control and thyristor rectifier with voltage and frequency control. Small-signal models are used to design the controller parameters and check the stability of the controlled systems, while simulation results are presented by using the proposed

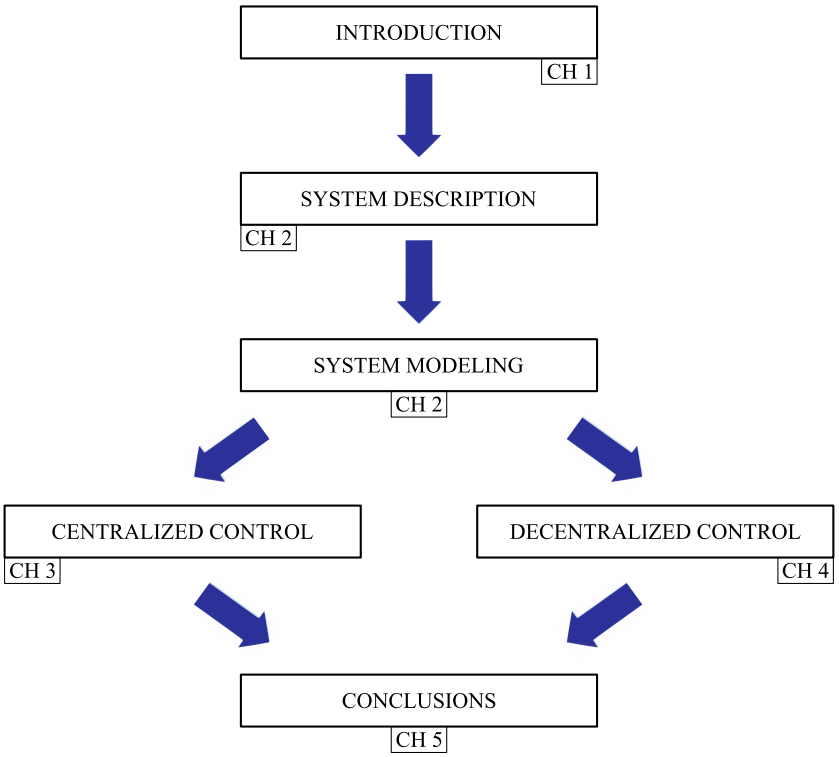

Figure 1.5: Flow chart of the Thesis structure.

AVM. Given that the control derivation, the controllers design, the stability analysis and the simulation are accomplished by using the proposed AVM, a validation against a detailed switching model (DSM) is carried out. Finally, fault response is also checked by a DSM simulation.

In Chapter 4, the decentralized frequency control for the connection of OWFs by diode-rectifier-based HVDC links is presented. First, the control fundamentals are addressed. Then, the decentralized frequency control schemes are presented. Even though the decentralized frequency control produces frequency deviations which are acceptable, they can be removed by the secondary frequency control which is also presented. Small-signal models are used to check the stability of the decentralized frequency control. Moreover, both the decentralized frequency control and the decentralized frequency control with secondary regulation are checked by a DSM simulation. Specifically, startup, operation and fault response are simulated.

Finally, the main conclusions are drawn in Chapter 5, where the publications which have been yielded from this Thesis are also addressed.

1.4 Bibliography

[1] M. D. Esteban et al. "Why offshore wind energy?" In: *Renewable Energy* 36.2 (2011), pp. 444–450 (cit. on pp. 1, 3).

[2] REN21. *Renewables 2017 Global Status Report*. 2017. URL: http://www.ren21.net/wp-content/uploads/2017/06/17-8399_GSR_2017_Full_Report_0621_Opt.pdf (visited on 04/17/2018) (cit. on p. 1).

[3] G. W. E. Council. *Global Wind Statistics 2017*. 2018. URL: http://gwec.net/wp-content/uploads/vip/GWEC_PRstats2017_EN-003_FINAL.pdf (visited on 04/18/2018) (cit. on pp. 1–3).

[4] M. Bilgili, A. Yasar, and E. Simsek. "Offshore wind power development in Europe and its comparison with onshore counterpart". In: *Renewable and Sustainable Energy Reviews* 15.2 (2011), pp. 905–915 (cit. on p. 2).

[5] P. Enevoldsen and S. V. Valentine. "Do onshore and offshore wind farm development patterns differ?" In: *Energy for Sustainable Development* 35 (2016), pp. 41–51 (cit. on p. 2).

[6] A. G. Gonzalez-Rodriguez. "Review of offshore wind farm cost components". In: *Energy for Sustainable Development* 37 (2017), pp. 10–19 (cit. on p. 3).

[7] H Li and Z. Chen. "Overview of different wind generator systems and their comparisons". In: *IET Renewable Power Generation* 2.2 (2008), pp. 123–138 (cit. on p. 4).

[8] P. Sorensen et al. "Modular structure of wind turbine models in IEC 61400-27-1". In: *Power and Energy Society General Meeting (PES), 2013 IEEE*. IEEE. 2013, pp. 1–5 (cit. on p. 4).

[9] H. Polinder et al. "Trends in wind turbine generator systems". In: *IEEE Journal of emerging and selected topics in power electronics* 1.3 (2013), pp. 174–185 (cit. on p. 4).

[10] T. A. Antunes, P. J. Santos, and A. J. Pires. "HVAC transmission restrictions in large scale offshore wind farm applications". In: *Compatibility, Power Electronics and Power Engineering (CPE-POWERENG), 2017 11th IEEE International Conference on*. IEEE. 2017, pp. 46–52 (cit. on p. 4).

[11] O. Gomis-Bellmunt et al. "Voltage–current characteristics of multiterminal HVDC-VSC for offshore wind farms". In: *Electric Power Systems Research* 81.2 (2011), pp. 440–450 (cit. on p. 4).

[12] I. López et al. "Review of wave energy technologies and the necessary power-equipment". In: *Renewable and Sustainable Energy Reviews* 27 (2013), pp. 413–434 (cit. on p. 5).

[13] S Rodrigues et al. "Trends of offshore wind projects". In: *Renewable and Sustainable Energy Reviews* 49 (2015), pp. 1114–1135 (cit. on p. 5).

[14] A Kalair, N Abas, and N Khan. "Comparative study of HVAC and HVDC transmission systems". In: *Renewable and Sustainable Energy Reviews* 59 (2016), pp. 1653–1675 (cit. on p. 5).

[15] R. Perveen, N. Kishor, and S. R. Mohanty. "Off-shore wind farm development: Present status and challenges". In: *Renewable and Sustainable Energy Reviews* 29 (2014), pp. 780–792 (cit. on p. 5).

[16] O. Beik and N. Schofield. "An offshore wind generation scheme with a high-voltage hybrid generator, HVDC interconnections, and transmission". In: *IEEE Transactions on Power Delivery* 31.2 (2016), pp. 867–877 (cit. on p. 5).

[17] K. Musasa et al. "Review on DC collection grids for offshore wind farms with high-voltage DC transmission system". In: *IET Power Electronics* 10.15 (2017), pp. 2104–2115 (cit. on p. 5).

[18] N. Flourentzou, V. G. Agelidis, and G. D. Demetriades. "VSC-based HVDC power transmission systems: An overview". In: *IEEE Transactions on power electronics* 24.3 (2009), pp. 592–602 (cit. on p. 5).

[19] O. Saborío-Romano et al. "Connection of OWPPs to HVDC networks using VSCs and Diode Rectifiers: an Overview". In: *15th International Workshop on Large-Scale Integration of Wind Power into Power Systems as well as on Transmission Networks for Offshore Wind Power Plants*. 2016 (cit. on p. 6).

[20] S. Foster, L. Xu, and B. Fox. "Control of an LCC HVDC system for connecting large offshore wind farms with special consideration of grid fault". In: *Power and Energy Society General Meeting-Conversion and Delivery of Electrical Energy in the 21st Century, 2008 IEEE*. IEEE. 2008, pp. 1–8 (cit. on p. 7).

[21] S. V. Bozhko et al. "Control of offshore DFIG-based wind farm grid with line-commutated HVDC connection". In: *Energy Conversion, IEEE Transactions on* 22.1 (2007), pp. 71–78 (cit. on p. 7).

[22] S. Bozhko et al. "Large offshore DFIG-based wind farm with line-commutated HVDC connection to the main grid: Engineering studies". In: *IEEE transactions on energy conversion* 23.1 (2008), pp. 119–127 (cit. on p. 7).

[23] H. Zhou, G. Yang, and H. Geng. "Grid integration of DFIG-based offshore wind farms with hybrid HVDC connection". In: *Electrical Machines and Systems, 2008. ICEMS 2008. International Conference on*. IEEE. 2008, pp. 2579–2584 (cit. on p. 7).

[24] H. Zhou et al. "Control of a hybrid high-voltage DC connection for large doubly fed induction generator-based wind farms". In: *Renewable Power Generation, IET* 5.1 (2011), pp. 36–47 (cit. on p. 7).

[25] H. Zhou, G. Yang, and J. Wang. "Modeling, analysis, and control for the rectifier of hybrid HVdc systems for DFIG-based wind farms". In: *IEEE Transactions on Energy Conversion* 26.1 (2011), pp. 340–353 (cit. on p. 7).

[26] D. Xiang et al. "Coordinated control of an HVDC link and doubly fed induction generators in a large offshore wind farm". In: *Power Delivery, IEEE Transactions on* 21.1 (2006), pp. 463–471 (cit. on pp. 7, 8).

[27] R. Li et al. "Grid frequency control design for offshore wind farms with naturally commutated HVDC link connection". In: *Industrial Electronics, 2006 IEEE International Symposium on*. Vol. 2. IEEE. 2006, pp. 1595–1600 (cit. on pp. 7, 8).

[28] R. Li, S. Bozhko, and G. Asher. "Frequency control design for offshore wind farm grid with LCC-HVDC link connection". In: *Power Electronics, IEEE Transactions on* 23.3 (2008), pp. 1085–1092 (cit. on pp. 7, 8).

[29] R Pena, J. Clare, and G. Asher. "A doubly fed induction generator using back-to-back PWM converters supplying an isolated load from a variable speed wind turbine". In: *IEE Proceedings-Electric Power Applications* 143.5 (1996), pp. 380–387 (cit. on p. 8).

[30] R Vidal-Albalate et al. "Simultaneous connection of Type-3 and Type-4 Off-shore wind farms to HVDC Diode Rectifier Units". In: *Proceedings of the 15th Wind Integration Workshop*. 2016, pp. 1–6 (cit. on pp. 8, 11, 12).

[31] P. Kundur, N. J. Balu, and M. G. Lauby. *Power system stability and control*. Vol. 7. McGraw-hill New York, 1994 (cit. on p. 8).

[32] T. H. Nguyen and D.-C. Lee. "Control of offshore wind farms based on HVDC". In: *Energy Conversion Congress and Exposition (ECCE), 2012 IEEE*. IEEE. 2012, pp. 3113–3118 (cit. on pp. 8, 9).

[33] T. H. Nguyen, D.-C. Lee, and C.-K. Kim. "A cost-effective converter system for HVDC links integrated with offshore wind farms". In: *Industrial Electronics Society, IECON 2013-39th Annual Conference of the IEEE*. IEEE. 2013, pp. 7978–7983 (cit. on pp. 8, 9).

[34] T. H. Nguyen, D.-C. Lee, and C.-K. Kim. "A series-connected topology of a diode rectifier and a voltage-source converter for an HVDC transmission system". In: *Power Electronics, IEEE Transactions on* 29.4 (2014), pp. 1579–1584 (cit. on pp. 8, 9).

[35] T. Ostrem et al. "Grid connected photovoltaic (PV) inverter with robust phase-locked loop (PLL)". In: *Transmission & Distribution Conference and Exposition: Latin America, 2006. TDC'06. IEEE/PES*. IEEE. 2006, pp. 1–7 (cit. on p. 8).

[36] S. L. Sanjuan. *Voltage oriented control of three-phase boost PWM converters: design, simulation and implementation of a 3-phase boost battery charger*. Chalmers University of Technology, 2010 (cit. on p. 8).

[37] T. H. Nguyen, Q. A. Le, and D.-C. Lee. "A novel HVDC-link based on hybrid voltage-source converters". In: *Energy Conversion Congress and Exposition (ECCE), 2015 IEEE*. IEEE. 2015, pp. 3338–3343 (cit. on pp. 8, 9).

[38] M. von Hofen et al. "Hybrid offshore HVDC converter with diode rectifier and Modular Multilevel Converter". In: *Power Electronics for Distributed Generation Systems (PEDG), 2016 IEEE 7th International Symposium on*. IEEE. 2016, pp. 1–7 (cit. on p. 9).

[39] F. Fein and B. Orlik. "Dual HVDC system with line-and self-commutated converters for grid connection of offshore wind farms". In: *Renewable Energy Research and Applications (ICRERA), 2013 International Conference on*. IEEE. 2013, pp. 280–285 (cit. on pp. 9, 12).

[40] F. Fein, H. Groke, and B. Orlik. "AC line fault characteristics of an HVDC link with line-and self-commutated converters in parallel operation". In: *PCIM Europe 2015; International Exhibition and Conference for Power Electronics, Intelligent Motion, Renewable Energy and Energy Management; Proceedings of*. VDE. 2015, pp. 1–8 (cit. on pp. 10, 12).

[41] J. L. Rodriguez-Amenedo, S. Arnalte, and J. C. Burgos. "Automatic generation control of a wind farm with variable speed wind turbines". In: *Energy Conversion, IEEE Transactions on* 17.2 (2002), pp. 279–284 (cit. on p. 10).

[42] F. Díaz-González et al. "Participation of wind power plants in system frequency control: Review of grid code requirements and control methods". In: *Renewable and Sustainable Energy Reviews* 34 (2014), pp. 551–564 (cit. on p. 10).

[43] P. Sørensen et al. "Progress in IEC 61400-27". In: *11th International Workshop on Large-Scale Integration of Wind Power into Power Systems as well as on Transmission Networks for Offshore Wind Power Plants*. 2012 (cit. on p. 10).

[44] R Blasco-Gimenez et al. "Voltage and frequency control of SG based wind farms with uncontrolled HVDC rectifier". In: *Industrial Electronics (ISIE), 2010 IEEE International Symposium on*. IEEE. 2010, pp. 2499–2504 (cit. on p. 10).

[45] R. Blasco-Gimenez et al. "Diode-Based HVdc link for the connection of large offshore wind farms". In: *Energy Conversion, IEEE Transactions on* 26.2 (2011), pp. 615–626 (cit. on p. 10).

[46] R. Blasco-Gimenez et al. "Distributed voltage and frequency control of offshore wind farms connected with a diode-based HVdc link". In: *Power Electronics, IEEE Transactions on* 25.12 (2010), pp. 3095–3105 (cit. on pp. 10, 11).

[47] S. Bernal-Perez et al. "Efficiency and fault ride-through performance of a diode-rectifier-and VSC-inverter-based HVDC link for offshore wind farms". In: *IEEE Transactions on Industrial Electronics* 60.6 (2013), pp. 2401–2409 (cit. on p. 11).

[48] R. Blasco-Gimenez et al. "LCC-HVDC connection of offshore wind farms with reduced filter banks". In: *IEEE Transactions on Industrial Electronics* 60.6 (2013), pp. 2372–2380 (cit. on p. 11).

[49] S Bernal-Perez et al. "Connection of off-shore wind power plants to VSC-MTdc networks using HVdc diode-rectifiers". In: *Industrial Electronics (ISIE), 2013 IEEE International Symposium on*. IEEE. 2013, pp. 1–6 (cit. on p. 11).

[50] S Añó-Villalba et al. "Wind power plant integration in voltage source converter HVdc grids with voltage droop control". In: *Mathematics and Computers in Simulation* (2017) (cit. on p. 11).

[51] A. A. Iván et al. "Control strategy of a HVDC-Diode Rectifier connected type-4 off-shore wind farm". In: *Future Energy Electronics Conference (IFEEC), 2015 IEEE 2nd International*. IEEE. 2015, pp. 1–6 (cit. on p. 11).

[52] A. I. Andrade, R. Blasco-Gimenez, and G. R. Pena. "Distributed control strategy for a wind generation systems based on PMSG with uncontrolled rectifier HVDC connection". In: *Industrial Technology (ICIT), 2015 IEEE International Conference on*. IEEE. 2015, pp. 982–986 (cit. on p. 11).

[53] M. Gierschner, H.-J. Knaak, and H.-G. Eckel. "Fixed-reference-frame-control: a novel robust control concept for grid side inverters in HVDC connected weak offshore grids". In: *Power Electronics and Applications (EPE'14-ECCE Europe), 2014 16th European Conference on*. IEEE. 2014, pp. 1–7 (cit. on p. 11).

[54] H Konishi et al. "A consideration of stable operating power limits in VSC-HVDC systems". In: (2001) (cit. on pp. 11, 12).

[55] M. Liserre, R. Teodorescu, and F. Blaabjerg. "Stability of photovoltaic and wind turbine grid-connected inverters for a large set of grid impedance values". In: *IEEE transactions on power electronics* 21.1 (2006), pp. 263–272 (cit. on pp. 11, 12).

[56] T Midtsund, J. Suul, and T Undeland. "Evaluation of current controller performance and stability for voltage source converters connected to a weak grid". In: *Power Electronics for Distributed Generation Systems (PEDG), 2010 2nd IEEE International Symposium on*. IEEE. 2010, pp. 382–388 (cit. on pp. 11, 12).

[57] C. Prignitz, H.-G. Eckel, and H.-J. Knaak. "DFIG wind turbines operating in a fixed reference frame". In: *Power Electronics and Applications (EPE'15 ECCE-Europe), 2015 17th European Conference on*. IEEE. 2015, pp. 1–8 (cit. on p. 11).

[58] C. Prignitz, H.-G. Eckel, and A. Rafoth. "FixReF sinusoidal control in line side converters for offshore wind power generation". In: *Power Electronics for Distributed Generation Systems (PEDG), 2015 IEEE 6th International Symposium on*. IEEE. 2015, pp. 1–5 (cit. on p. 11).

[59] C. Prignitz et al. "FixReF: A control strategy for offshore wind farms with different wind turbine types and diode rectifier HVDC transmission". In: *Power Electronics for Distributed Generation Systems (PEDG), 2016 IEEE 7th International Symposium on*. IEEE. 2016, pp. 1–7 (cit. on pp. 11, 12).

[60] C. Prignitz, H.-G. Eckel, and S. Achenbach. "FixReF: A Current Control Strategy for Offshore Wind Turbines Connected to Different Types of HVDC Transmission". In: *Proceedings of the 15th Wind Integration Workshop*. 2016, pp. 1–8 (cit. on p. 11).

[61] P Menke et al. “Breakthrough in DC grid access technology for large scale offshore wind farms”. In: *EWEA offshore, Copenhagen, Denmark* (2015), pp. 1–5 (cit. on p. 12).

[62] P Menke et al. “2nd Generation DC Grid Access for Large Scale Offshore Wind Farms”. In: *14th International Wind Integration Workshop, Brüssel*. 2015 (cit. on p. 12).

[63] S. Seman, R. Zurowski, and C. Taratoris. “Interconnection of advanced Type 4 WTGs with Diode Rectifier based HVDC solution and weak AC grids”. In: *Proceedings of the 14th Wind Integration Workshop*. 2015, pp. 1–7 (cit. on p. 12).

[64] P. B. Brogan et al. *Control method for self-commutated converter for controlling power exchange*. US Patent App. 14/913,182. 2013 (cit. on p. 12).

[65] L. Yu, R. Li, and L. Xu. “Distributed PLL-Based Control of Offshore Wind Turbines Connected With Diode-Rectifier-Based HVDC Systems”. In: *IEEE Transactions on Power Delivery* 33.3 (2018), pp. 1328–1336 (cit. on p. 12).

[66] P. on Meshed HVDC Offshore Transmission Networks. *Deliverable 1.1: Detailed description of the requirements that can be expected per work package*. 2016. URL: https://www.promotion-offshore.net/fileadmin/PDFs/160415_PROMOtioN_WP1_D_1.1_V1.0.pdf (visited on 04/29/2018) (cit. on p. 12).

Chapter 2

System Description and Modeling

2.1 Introduction

The performance and the stability of the control strategies proposed in this Thesis are analyzed by means of different models of the system. The system under study is the LCC-rectifier-based HVDC connection of an OWF, whose overview is depicted in Figure 2.1. In addition to the HVDC link cables and converters, the rectifier transformer, the AC harmonic filters and the reactive power compensation bank are shown in Figure 2.1. This chapter presents the models used for the main elements of the system in the studied application: the HVDC inverter, the HVDC cables, the WTGSs and the HVDC rectifier. Then, these models will be combined in order to form the OWF layouts used along the studies in this Thesis.

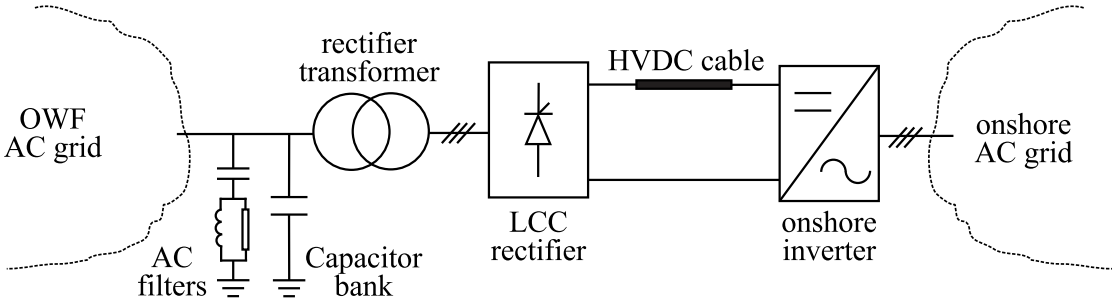

Figure 2.1: Overview of the elements of an LCC-rectifier-based HVDC connection of an OWF.

Part of the models which are presented in this chapter do not only have a final proposal-analysis purpose but they are also used in order to obtain and to explain the control strategy fundamentals of the proposals. It is worth mentioning that a real OWF is composed of a high number of WTGSs which may go from tens of WTGSs to hundreds of WTGSs. The number of WTGSs could be reduced given that the offshore WTGS capacity is increasing [1]. However, the total OWF capacity is growing faster [1] and a high amount of WTGSs is still needed for large OWFs.

From the simulation point of view, aggregated models are mainly used because they allow the reproduction of the real OWF response with reduced computational requirements. Moreover, the aggregated models also clarify the analysis of the proposed solutions.

It is worth mentioning that the LCC rectifier models presented in this chapter will consider the general case of a controlled thyristor rectifier with its firing angle α. Therefore, the model becomes the one of the uncontrolled diode rectifier by setting a zero firing angle (α=0).

2.2 HVDC link model

In this section, the models used for the HVDC inverter and the HVDC cables are presented. However, the detailed study of these two elements is out of the scope of this Thesis. For this reason, reduced models will be used in order to represent these elements in the OWF layouts which will be used. However, the LCC rectifier plays a very important role in the HVDC integration proposed in this Thesis. Therefore, DSMs will be used and an AVM will be presented in the following section.

Since the substation footprint and weight are not as important onshore as offshore, any of the existing technologies (LCC and VSC) can be used in the HVDC onshore inverter. The aim of the OWF application consists of transmitting all the power generated by the WTGSs to the onshore AC grid. The rectifier converter injects all the power to the HVDC link while the inverter converter must deliver all this power to the onshore AC grid. This can be achieved by maintaining constant its DC voltage. The study of

the HVDC inverter is out of the scope of this Thesis, but it is required to be operated at constant DC voltage mode, so it is modeled as a DC voltage source as in previous studies [2]. This inverter DC source is addressed by V_{di} along this Thesis.

The cables are usually represented by their π-model or their T-model. The accuracy of the model can be increased by considering models for reduced lengths of the cable, which will result in a final model which is composed of multiple π-models connected in series, *i.e.* a distributed cable model. An enhanced π-model is presented in [3], where a mutual inductance considers the coupling between the core and the screen parts of the cable. However, this DC cable accuracy is not needed and reduced cable models are considered in this Thesis. The main model used for the cable is the T-model proposed in the HVDC Benchmark model [4], which has the inductances L_{dc1} and L_{dc2}, the resistances R_{dc1} and R_{dc2} and the capacitor C_c. However, there is one study case where the dynamics of the cable are neglected and a pure resistive link is considered (R_{dc}). Figure 2.2 shows both cable models together with the inverter model. On the one hand, it is worth noting that the dynamics of the T-model establishes three new state variables which are the rectifier DC current I_{dc1}, the inverter DC current I_{dc2} and the HVDC link voltage V_c. On the other hand, the resistive link only adds the DC link current I_{dc} to the rectifier and inverter DC voltages (V_{dr} and V_{di}, respectively).

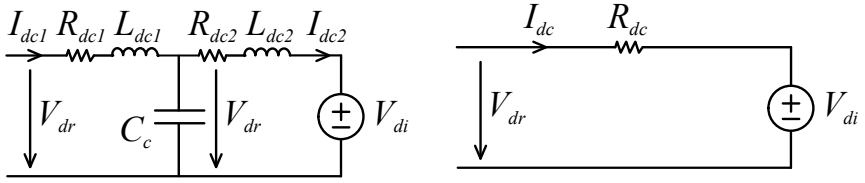

(a) T-model. *(b)* Pure resistive model.

Figure 2.2: HVDC link models.

2.3 LCC-Rectifier AVM

The use of DSMs in the power electronics field has the advantage of their full and precise representation of the diverse components. However, their discontinuous nature makes the extraction of their small-signal characteristics difficult and the computing time is increased in comparison to simpler models [5]. For this reason, AVMs are extensively used for power electronic components studies. Although the proposals in this Thesis will be also checked by using the DSM of the LCC rectifier, it proves useful to employ the AVM for the stability analyses and the derivation of the control strategy fundamentals. Following, the state of the art of LCC converters average-value modeling is addressed.

The AVM of an LCC converter connected to a synchronous machine is studied in [6]. This model considers the dq subtransient reactances. In [7], the proposed model considers the stator dynamics. A new approach is presented in [8], because the model does not consider the DC smoothing reactor. Therefore, constant DC current and continuous current operation cannot be assumed. Although the aforementioned approaches are analytical, parametric models which consider the diverse rectifier conduction modes can be found in [9, 10, 11]. Most of the proposals analyze the rectifier operation, but the LCC inverter operation is also studied in [12]. Moreover, AC waveforms with their harmonic contents can be reconstructed by means of a parametric AVM [13].

Although in [14] the diverse AVMs which can be used for the representation of a diode rectifier load are compared, the dynamics of the AC filter capacitor are not evaluated in any of the studied models. This Thesis presents an enhanced AVM which considers the LCC rectifier, its transformer and the dynamics of the AC capacitor bank connected to its primary winding AC bus. The AVM which is proposed in [15] is not totally correct. The active power balance of the converter is affected by the losses at the commutation resistance which is included in the model circuit. This commutation resistance is an equivalent resistance which allows the representation of the DC voltage drop which is caused by the inductance at the rectifier AC side. However, it should not produce any power consumption [16] as it does in [15]. Finally, there is a solution which allows the selection of the harmonic contents to be considered in the model: the dynamic phasors technique [17, 18, 19]. In [17], an equivalent DC inductance is proposed. It is derived by adding the value of the AC inductance which is seen from the LCC converter DC side to the DC inductance value.

The enhanced AVM which is presented in this Thesis considers the dynamics of the capacitor bank which is placed at the primary side of the LCC rectifier transformer. This capacitor bank is usually placed for reactive power compensation of both the LCC rectifier and its transformer. It represents also the capacity of the AC harmonic filters at fundamental frequency [20] and its location in the case of the OWF application corresponds to the PCC bus. One advantage of the proposed model is that the incoming active and reactive powers from the OWF are the inputs. This is convenient given that the conventional operation variables of the WTGSs are also their output power components. Moreover, the AC state variables of the AVM are the polar components of the voltage vector at the capacitor bank bus in a dq synchronous reference frame. These state variables are useful to derive the centralized frequency control proposed in this Thesis. The proposed model can be also used to evaluate the dynamic performance of the LCC rectifier station and other dynamic components with the complete topology of the OWF grid. For such a study, the grid is considered in steady-state and a step-by-step load flow is used [21]. The capacitor bank bus is the slack bus of the load flow. Therefore, the active and reactive powers resulting from the load flow study are introduced in the proposed AVM which provides the slack bus voltage magnitude and

angle to be considered in the successive load flow. This load flow will in turn provide the following powers to be considered in the AVM in this iterative process.

In this section, the classic AVM of the LCC rectifier is first addressed. This AVM usually combines both the LCC rectifier and its supplying transformer. This transformer is quite important for the rectifier as it has a double functionality. It provides the needed galvanic insulation while it provides phase displacement among the transformer secondary windings for the diverse rectifier configurations. Given that these windings are connected to individual six-pulse rectifier bridges whose DC outputs are connected in series, AC power quality is improved by reducing the total harmonic distortion (THD) of the LCC rectifier. Two examples of a 12-pulse rectifier (30° phase displacement achieved by the star-delta connection) and an 18-pulse rectifier (±20° phase displacement achieved by the zig-zag connections) are shown in Figure 2.3. The AC current harmonic content reduction is shown in Table 2.1 [22].

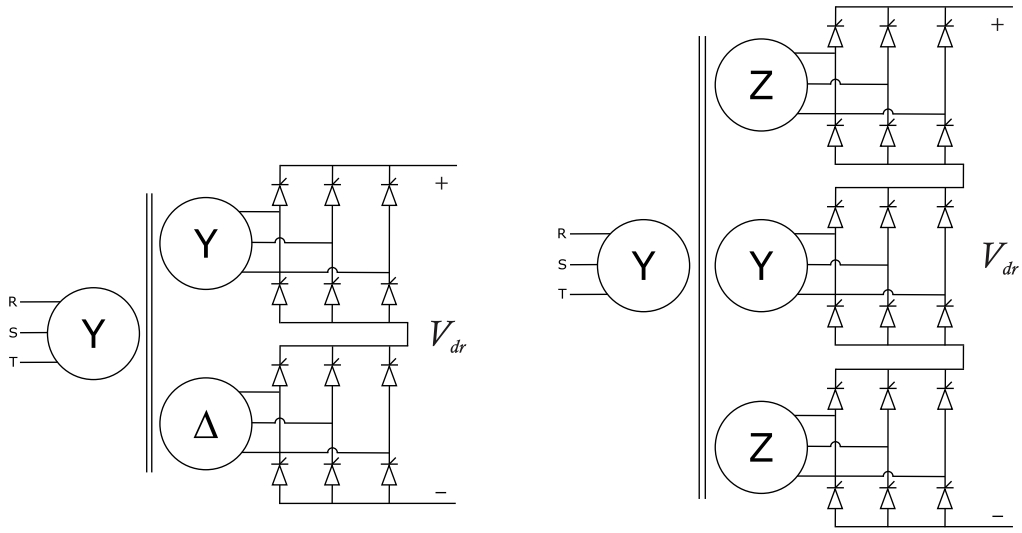

(a) 12-pulse rectifier. *(b)* 18-pulse rectifier.

Figure 2.3: LCC rectifier configurations.

Table 2.1: AC current THD comparison of different LCC rectifier configurations considering the same load and system per-unit parameters and a zero firing angle.

	6-pulse rectifier	**12-pulse rectifier**	**18-pulse rectifier**
THD	23.9 %	8.61 %	3.54 %

For the sake of clarity, the LCC rectifiers along this Thesis will be represented by a box with the picture of a thyristor or a diode (see Figure 2.4), depending on the semiconductor used. As it is addressed under this box, the drawing represents a rectifier with n_b six-pulse bridges and the appropriate transformer configurations. Therefore, a 12-pulse rectifier and an 18-pulse rectifier will correspond to n_b equal to two and three, respectively.

Following, the classic AVM equations of the combination of the LCC rectifier and its transformer are first presented. Then, the aforementioned equations are used to derive the model equations when the dynamics of the capacitor bank connected to the PCC bus is considered.

2.3.1 Classic Rectifier and transformer AVM

This section presents the equations that determine the LCC rectifier and transformer AVM which is depicted in Figure 2.4. The transformer is defined by its short-circuit inductance L_t. DC voltage and current of the rectifier are addressed as V_{dr} and I_{dc}, respectively. The root mean square (RMS) values of the three-phase line PCC bus voltage and rectifier current are U_{pcc} and I_r, respectively. A continuous current operation of the LCC rectifier is assumed given the DC smoothing reactor which is placed at the rectifier DC output in order to reduce the DC current ripple. Moreover, the losses are neglected in both the transformer and the AC-DC conversion.

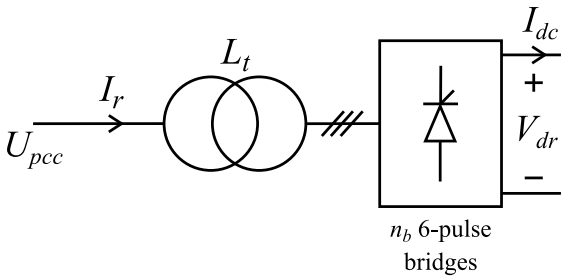

Figure 2.4: LCC rectifier and transformer AVM.

The equations of this model are the algebraic equations which relate the AC and the DC magnitudes between the input and the output of the rectifier. The Fourier analysis [16, 23] allows the derivation of these equations by the only consideration of the fundamental components. The main equations are the ones which relate voltages and currents and they are as follows:

$$V_{dr} = \frac{3\sqrt{2}}{\pi} n_b k_{\alpha,\mu} U_{pcc} \cos\varphi \tag{2.1}$$

$$I_r = \frac{\sqrt{6}}{\pi} n_b k_{\alpha,\mu} I_{dc} \tag{2.2}$$

where φ is the phase shift between the PCC voltage and the rectifier current and the variable $k_{\alpha,\mu}$ depends on the rectifier firing angle α and its commutation angle μ.

It is worth noting that additional equations are needed in order to define $k_{\alpha,\mu}$ and φ. The equation of $k_{\alpha,\mu}$ is (2.3) and it uses the commutation angle which can be obtained by applying (2.4). The combination of (2.1) and (2.5) provides the equation to obtain φ,

which is (2.6).

$$k_{\alpha,\mu} = \frac{1}{2}\Big(\cos\alpha + \cos\left(\alpha+\mu\right)\Big)\sqrt{1+\Big(\mu\csc\mu\csc\left(2\alpha+\mu\right)-\cot\left(2\alpha+\mu\right)\Big)^2} \quad (2.3)$$

$$R_\mu I_{dc}=\frac{\frac{3\sqrt{2}}{\pi}U_{pcc}}{2}\Big(\cos\alpha-\cos\left(\alpha+\mu\right)\Big) \;\rightarrow\; \mu=\arccos\left(\cos\alpha-\frac{2\pi R_\mu I_{dc}}{3\sqrt{2}U_{pcc}}\right)-\alpha \quad (2.4)$$

$$V_{dr} = \frac{3\sqrt{2}}{\pi}n_b U_{pcc}\cos\alpha - n_b R_\mu I_{dc} \quad (2.5)$$

$$\varphi = \arccos\left(\frac{1}{k_{\alpha,\mu}}\Big(\cos\alpha - \frac{\pi R_\mu I_{dc}}{3\sqrt{2}n_b U_{pcc}}\Big)\right) \quad (2.6)$$

where $R_\mu=\frac{3}{\pi}\omega_0 L_t$ is the commutating resistance and ω_0 is the AC system frequency.

Finally, the active and reactive power inputs to the LCC rectifier and transformer from the PCC bus, P_r and Q_r respectively, can be defined as follows:

$$P_r = V_{dr} I_{dc} \quad (2.7)$$

$$Q_r = V_{dr} I_{dc}\tan\varphi = P_r\tan\varphi \quad (2.8)$$

Equations (2.1) to (2.8) define then the AC-DC conversion of the LCC rectifier and transformer AVM in real values. The base magnitudes of both the AC system and the DC system powers, voltages, currents and impedances can be defined as follows:

$$S_{base,AC} = \sqrt{3}V_{base,AC}I_{base,AC} \quad (2.9)$$

$$Z_{base,AC} = \frac{V_{base,AC}^2}{S_{base,AC}} \quad (2.10)$$

$$P_{base,DC} = V_{base,DC}I_{base,DC} = S_{base,AC} \quad (2.11)$$

$$V_{base,DC} = \frac{3\sqrt{2}}{\pi}n_b V_{base,AC} \quad (2.12)$$

$$I_{base,AC} = \frac{\sqrt{6}}{\pi}n_b I_{base,DC} \quad (2.13)$$

$$R_{base,DC} = \frac{V_{base,DC}}{I_{base,DC}} = \left(\frac{3\sqrt{2}}{\pi}n_b\right)^2 Z_{base,AC} \quad (2.14)$$

Therefore, the per-unit AC-DC conversion is defined by the equations in (2.15) to (2.21). It is worth noting that lowercase notation is used along this Thesis to denote

per-unit variables.

$$v_{dr} = k_{\alpha,\mu} u_{pcc} \cos\varphi = u_{pcc} \cos\alpha - r_\mu i_{dc} \tag{2.15}$$

$$i_r = k_{\alpha,\mu} i_{dc} \tag{2.16}$$

$$\mu = \arccos\left(\cos\alpha - \frac{2 r_\mu i_{dc}}{u_{pcc}}\right) - \alpha \tag{2.17}$$

$$\varphi = \arccos\left(\frac{1}{k_{\alpha,\mu}}\left(\cos\alpha - \frac{r_\mu i_{dc}}{u_{pcc}}\right)\right) \tag{2.18}$$

$$r_\mu = \frac{n_b R_\mu}{R_{base,DC}} = \frac{n_b \frac{3}{\pi}\omega_0 L_t}{\left(\frac{3\sqrt{2}}{\pi} n_b\right)^2 \omega_0 L_{base}} = \frac{\pi}{6}\frac{x_t}{n_b} \tag{2.19}$$

$$p_r = v_{dr} i_{dc} \tag{2.20}$$

$$q_r = v_{dr} i_{dc} \tan\varphi = p_r \tan\varphi \tag{2.21}$$

where x_t is the per-unit reactance of each of the six-pulse rectifier transformers over the global AC base power $S_{base,AC}$.

2.3.1.1 Small-signal model of the HVDC link considering the classic rectifier and transformer model

The small-signal model derived in this section corresponds to the HVDC link modeled by the T-modeled cable and inverter shown in Section 2.2 and the classic LCC rectifier and transformer model. It will be used for stability analysis in Chapter 4 of this Thesis. For the sake of clarity, the diagram which shows the inputs and outputs of the model is shown in Figure 2.5. Note that the outputs are the current components injected to the AC grid while the AC voltage components are inputs, given the small-signal models interconnection which will be carried out in Chapter 4.

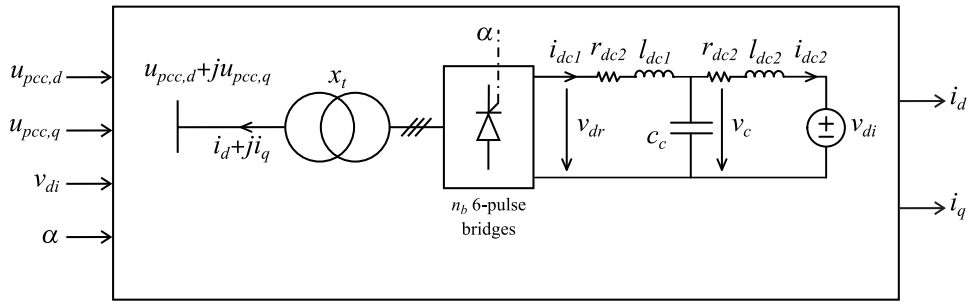

Figure 2.5: Inputs and outputs diagram of the T-modeled HVDC link which includes the classic LCC rectifier and transformer model.

The per-unit dynamic equations of the HVDC link T-modeled cable and inverter are as follows:

$$\frac{l_{dc1}}{\omega_0}\frac{di_{dc1}}{dt} = v_{dr} - v_c - r_{dc1}i_{dc1}$$

$$\frac{c_c}{\omega_0}\frac{dv_c}{dt} = i_{dc1} - i_{dc2}$$

$$\frac{l_{dc2}}{\omega_0}\frac{di_{dc2}}{dt} = v_c - v_{di} - r_{dc2}i_{dc2} \tag{2.22}$$

where:

$$c_c = \omega_0 C_c R_{base,DC} \tag{2.23}$$

$$l_{dck} = \omega_0 \frac{L_{dck}}{R_{base,DC}} = \omega_0 \frac{R_{dck}\tau_{dck}}{R_{base,DC}} = \tau_{dck}\omega_0 r_{dck} \quad (k = 1, 2) \tag{2.24}$$

It is worth noting that the outputs of the system are only the dq components of the current injected to the AC grid (i_d and i_q). The equations of these currents are derived from the classic rectifier and transformer model considering the rectifier DC current i_{dc1} as follows:

$$(i_d + j i_q) = -\left(\frac{p_r + j q_r}{u_{pcc,d} + j u_{pcc,q}}\right)^* = \frac{-v_{dr} i_{dc1}}{u_{pcc,d}^2 + u_{pcc,q}^2}\Big((1 + j\tan\varphi)(u_{pcc,d} - j u_{pcc,q})\Big)^* =$$

$$= \underbrace{\frac{v_{dr} i_{dc1}}{u_{pcc,d}^2 + u_{pcc,q}^2}(-u_{pcc,d} - u_{pcc,q}\tan\varphi)}_{i_d} + j\underbrace{\frac{v_{dr} i_{dc1}}{u_{pcc,d}^2 + u_{pcc,q}^2}(u_{pcc,d}\tan\varphi - u_{pcc,q})}_{i_q} \tag{2.25}$$

This small-signal model has the state variables in (2.22), where v_{dr} can be derived from the equations addressed in Section 2.3.1 ((2.3), (2.15) and (2.17) to (2.19)), where the rectifier DC current is now equal to i_{dc1}. For the sake of simplicity, $k_{\alpha,\mu}$ is considered as a constant [23] for the small-signal studies along this Thesis.

Therefore, the small-signal model can be obtained and it is presented in (2.26). The inputs, outputs and states considered for this small-signal model are $\boldsymbol{\Delta u_{cr}} = [\Delta u_{pcc,d}, \Delta u_{pcc,q}, \Delta v_{di}, \Delta\alpha]^\mathsf{T}$, $\boldsymbol{\Delta y_{cr}} = [\Delta i_d, \Delta i_q]^\mathsf{T}$ and $\boldsymbol{\Delta x_{cr}} = [\Delta i_{dc1}, \Delta v_c, \Delta i_{dc2}]^\mathsf{T}$, respectively. Note that the subscript 0 denotes steady-state value of the variables along this Thesis while the subscript cr denotes the classic rectifier small-signal model.

$$\frac{d\boldsymbol{\Delta x_{cr}}}{dt} = \boldsymbol{A_{cr}}\boldsymbol{\Delta x_{cr}} + \boldsymbol{B_{cr}}\boldsymbol{\Delta u_{cr}}$$

$$\boldsymbol{\Delta y_{cr}} = \boldsymbol{C_{cr}}\boldsymbol{\Delta x_{cr}} + \boldsymbol{D_{cr}}\boldsymbol{\Delta u_{cr}} \tag{2.26}$$

where $\boldsymbol{A_{cr}}$, $\boldsymbol{B_{cr}}$, $\boldsymbol{C_{cr}}$ and $\boldsymbol{D_{cr}}$ are as follows:

$$\boldsymbol{A_{cr}} = \begin{bmatrix} -\dfrac{\omega_0(r_\mu + r_{dc1})}{l_{dc1}} & -\dfrac{\omega_0}{l_{dc1}} & 0 \\ \dfrac{\omega_0}{c_c} & 0 & -\dfrac{\omega_0}{c_c} \\ 0 & \dfrac{\omega_0}{l_{dc2}} & -\dfrac{\omega_0 r_{dc2}}{l_{dc2}} \end{bmatrix}$$

$$\boldsymbol{B_{cr}} = \begin{bmatrix} \dfrac{\omega_0 \cos\alpha_0 u_{pcc,d0}}{l_{dc1} u_{pcc0}} & \dfrac{\omega_0 \cos\alpha_0 u_{pcc,q0}}{l_{dc1} u_{pcc0}} & 0 & -\dfrac{\omega_0 \sin\alpha_0 u_{pcc0}}{l_{dc1}} \\ 0 & 0 & 0 & 0 \\ 0 & 0 & -\dfrac{\omega_0}{l_{dc2}} & 0 \end{bmatrix}$$

$$\boldsymbol{C_{cr}} = \begin{bmatrix} c_{cr,11} & 0 & 0 \\ c_{cr,21} & 0 & 0 \end{bmatrix}$$

$$\boldsymbol{D_{cr}} = \begin{bmatrix} d_{cr,11} & d_{cr,12} & 0 & d_{cr,14} \\ d_{cr,21} & d_{cr,22} & 0 & d_{cr,24} \end{bmatrix} \tag{2.27}$$

where the non-defined terms are as follows:

$$c_{cr,11} = \frac{(u_{pcc0}\cos\alpha_0 - 2r_\mu i_{dc10})(-u_{pcc,d0} - u_{pcc,q0}\tan\varphi_0) - u_{pcc,q0} v_{dr0} i_{dc10} (\sec\varphi_0)^2 \zeta_{i_{dc10}}}{u_{pcc0}^2}$$

$$c_{cr,21} = \frac{(u_{pcc0}\cos\alpha_0 - 2r_\mu i_{dc10})(u_{pcc,d0}\tan\varphi_0 - u_{pcc,q0}) + u_{pcc,d0} v_{dr0} i_{dc10} (\sec\varphi_0)^2 \zeta_{i_{dc10}}}{u_{pcc0}^2}$$

$$d_{cr,11} = \frac{i_{dc10}\Bigg(\Big(\frac{u_{pcc,d0}}{u_{pcc0}}\cos\alpha_0\big(-u_{pcc,d0} - u_{pcc,q0}\tan\varphi_0\big) - v_{dr0}\big(u_{pcc,q0}(\sec\varphi_0)^2\zeta_{u_{pcc,d0}} + \\ +1\big)\Big)u_{pcc0}^2 + 2u_{pcc,d0}v_{dr0}\Big(u_{pcc,d0} + u_{pcc,q0}\tan\varphi_0\Big)\Bigg)}{u_{pcc0}^4}$$

$$d_{cr,12} = \frac{i_{dc10}\Bigg(\Big(\frac{u_{pcc,q0}}{u_{pcc0}}\cos\alpha_0\big(-u_{pcc,d0} - u_{pcc,q0}\tan\varphi_0\big) - v_{dr0}\big(u_{pcc,q0}(\sec\varphi_0)^2\zeta_{u_{pcc,q0}} + \\ +\tan\varphi_0\big)\Big)u_{pcc0}^2 + 2u_{pcc,q0}v_{dr0}\Big(u_{pcc,d0} + u_{pcc,q0}\tan\varphi_0\Big)\Bigg)}{u_{pcc0}^4}$$

$$d_{cr,14}=\frac{i_{dc10}\Big(u_{pcc0}\sin\alpha_0(u_{pcc,d0}+u_{pcc,q0}\tan\varphi_0)-v_{dr0}u_{pcc,q0}(\sec\varphi_0)^2\zeta_{\alpha_0}\Big)}{u_{pcc0}^2}$$

$$d_{cr,21}=\frac{i_{dc10}\Bigg(\Big(\frac{u_{pcc,d0}}{u_{pcc0}}\cos\alpha_0\big(u_{pcc,d0}\tan\varphi_0-u_{pcc,q0}\big)+v_{dr0}\big(u_{pcc,d0}(\sec\varphi_0)^2\zeta_{u_{pcc,d0}}+ \\ +\tan\varphi_0\big)\Big)u_{pcc0}^2-2u_{pcc,d0}v_{dr0}\Big(u_{pcc,d0}\tan\varphi_0-u_{pcc,q0}\Big)\Bigg)}{u_{pcc0}^4}$$

$$d_{cr,22}=\frac{i_{dc10}\Bigg(\Big(\frac{u_{pcc,q0}}{u_{pcc0}}\cos\alpha_0\big(u_{pcc,d0}\tan\varphi_0-u_{pcc,q0}\big)+v_{dr0}\big(u_{pcc,d0}(\sec\varphi_0)^2\zeta_{u_{pcc,q0}}- \\ -1\big)\Big)u_{pcc0}^2-2u_{pcc,q0}v_{dr0}\Big(u_{pcc,d0}\tan\varphi_0-u_{pcc,q0}\Big)\Bigg)}{u_{pcc0}^4}$$

$$d_{cr,24}=\frac{i_{dc10}\Big(-u_{pcc0}\sin\alpha_0(u_{pcc,d0}\tan\varphi_0-u_{pcc,q0})+v_{dr0}u_{pcc,d0}(\sec\varphi_0)^2\zeta_{\alpha_0}\Big)}{u_{pcc0}^2}$$

$$\zeta_{u_{pcc0}}=\left(\frac{\partial\varphi}{\partial u_{pcc}}\right)_0=\frac{1}{k_{\alpha,\mu}}\frac{-r_\mu i_{dc10}}{u_{pcc0}^2\sin\varphi_0}$$

$$\zeta_{u_{pcc,d0}}=\left(\frac{\partial\varphi}{\partial u_{pcc,d}}\right)_0=\frac{u_{pcc,d0}}{u_{pcc0}}\zeta_{u_{pcc0}}$$

$$\zeta_{u_{pcc,q0}}=\left(\frac{\partial\varphi}{\partial u_{pcc,q}}\right)_0=\frac{u_{pcc,q0}}{u_{pcc0}}\zeta_{u_{pcc0}}$$

$$\zeta_{i_{dc10}}=\left(\frac{\partial\varphi}{\partial i_{dc1}}\right)_0=\frac{1}{k_{\alpha,\mu}}\frac{r_\mu}{u_{pcc0}\sin\varphi_0}$$

$$\zeta_{\alpha_0}=\left(\frac{\partial\varphi}{\partial\alpha}\right)_0=\frac{1}{k_{\alpha,\mu}}\frac{\sin\alpha_0}{\sin\varphi_0} \tag{2.28}$$

It is worth noting that all the LCC rectifier models in this Thesis become a diode rectifier model by considering a zero firing angle in the equations and by eliminating their firing angle input.

2.3.2 Proposed LCC rectifier station AVM

The AVM model which is proposed in this section considers the LCC rectifier, its transformer and the dynamics of the AC capacitor bank connected to the PCC bus. It

is developed considering several assumptions which are addressed following:

- Harmonics are neglected in the voltages and currents of both the AC and the DC sides.
- Power losses are neglected in the LCC rectifier conversion and its transformer as in the classic model.
- The capacitor bank C connected to the PCC bus includes the capacitance for reactive power compensation and the capacitance of the harmonic filters at the fundamental frequency [20].
- The LCC rectifier is made up of n_b six-pulse rectifier bridges that are connected in series in their DC side.
- The rest of the AC system is represented by the incoming active and reactive powers to the rectifier station bus, *i.e.* the PCC bus.

The previous assumptions correspond to the LCC rectifier station layout presented in Figure 2.6. Note that the incoming active and reactive powers are addressed as P_{owf} and Q_{owf}, respectively, given the application considered in this Thesis.

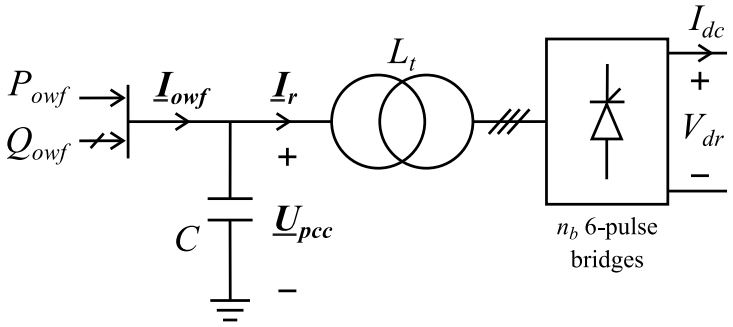

Figure 2.6: Overview of the proposed AVM system.

2.3.2.1 AVM in the *dq* synchronous reference frame

The model which is depicted in Figure 2.6 considers a synchronous reference frame which rotates at frequency ω_0 which is shown in Figure 2.7. It is worth noting that vectors in the dq synchronous reference frame are denoted by bold underlined fonts along this Thesis. Therefore, the three-phase OWF line currents $i_{owf,a}, i_{owf,b}, i_{owf,c}$, rectifier line currents $i_{r,a}, i_{r,b}, i_{r,c}$ and PCC bus voltages $u_{pcc,a}, u_{pcc,b}, u_{pcc,c}$ are represented in Figure 2.6 by their corresponding vectors $\underline{\boldsymbol{I}}_{\boldsymbol{owf}}$, $\underline{\boldsymbol{I}}_{\boldsymbol{r}}$ and $\underline{\boldsymbol{U}}_{\boldsymbol{pcc}}$ in the dq synchronous reference frame. The Park transformation in (2.29) defines the calculation of the vectors

in the dq synchronous reference frame from the three-phase a, b, c values.

$$\boldsymbol{T}(\theta(t)) = \sqrt{\frac{2}{3}} \begin{bmatrix} \cos(\theta(t)) & \cos\left(\theta(t) - \frac{2\pi}{3}\right) & \cos\left(\theta(t) + \frac{2\pi}{3}\right) \\ -\sin(\theta(t)) & -\sin\left(\theta(t) - \frac{2\pi}{3}\right) & -\sin\left(\theta(t) + \frac{2\pi}{3}\right) \end{bmatrix} \tag{2.29}$$

where $\theta(t)=\omega_0 t-\frac{\pi}{2}+\phi_0$ and ϕ_0, which is shown in Figure 2.7, is the angle of the synchronous reference frame in the stationary system.

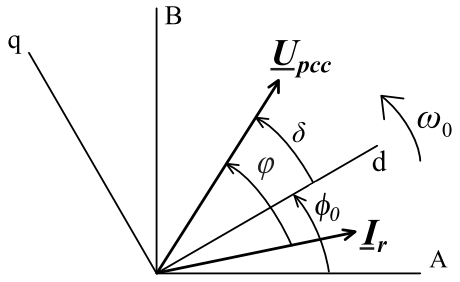

Figure 2.7: Vector diagram of the PCC bus voltage and rectifier current vectors in the stationary and synchronous reference systems.

As it was previously established, the dynamics of the capacitor bank connected to the PCC bus is considered in this AVM. This dynamics equation is expressed in (2.30), which is split in its dq components in (2.31). Due to the fact that the model which represents the transformer and the rectifier is not dynamic, the PCC voltage dq components $U_{pcc,d}$ and $U_{pcc,q}$ will be initially the state variables of the model.

$$\underline{\boldsymbol{I}}_{\boldsymbol{owf}} - \underline{\boldsymbol{I}}_{\boldsymbol{r}} = C\frac{d\underline{\boldsymbol{U}}_{\boldsymbol{pcc}}}{dt} + j\omega_0 C\underline{\boldsymbol{U}}_{\boldsymbol{pcc}} \tag{2.30}$$

$$I_{owf,d} - I_{r,d} = C\frac{dU_{pcc,d}}{dt} - \omega_0 C U_{pcc,q}$$

$$I_{owf,q} - I_{r,q} = C\frac{dU_{pcc,q}}{dt} + \omega_0 C U_{pcc,d} \tag{2.31}$$

The classic equations which are obtained by the Fourier analysis at fundamental frequency for the AC-DC conversion of the rectifier, which are (2.1) and (2.2), can be now used. They allow the definition of the switching vector $\boldsymbol{S_{abc}}$ between the three-phase AC and the DC voltages and currents, which is shown in (2.32). It is worth noting that bold font denotes vectors and matrices along this Thesis.

$$V_{dr} = \boldsymbol{S_{abc}}^{\mathsf{T}} \boldsymbol{U_{pcc,abc}}$$

$$\boldsymbol{I_{r,abc}} = \boldsymbol{S_{abc}} I_{dc} \tag{2.32}$$

where $\boldsymbol{I_{r,abc}}=[i_{r,a}(t) \quad i_{r,b}(t) \quad i_{r,c}(t)]^{\mathsf{T}}$, $\boldsymbol{U_{pcc,abc}}=[u_{pcc,a}(t) \quad u_{pcc,b}(t) \quad u_{pcc,c}(t)]^{\mathsf{T}}$ and $\boldsymbol{S_{abc}}$ is as follows:

$$\boldsymbol{S_{abc}} = \frac{2\sqrt{3}}{\pi} k_{\alpha,\mu} n_b \left[\sin\gamma \quad \sin\left(\gamma - \frac{2\pi}{3}\right) \quad \sin\left(\gamma + \frac{2\pi}{3}\right) \right]^{\mathsf{T}} \tag{2.33}$$

where $\gamma = \omega_0 t + \phi - \varphi$, $\phi = \phi_0 + \delta$ is the PCC voltage phase angle which can be seen in Figure 2.7.

$\boldsymbol{S_{abc}}$ can be then transformed into a dq switching vector by applying the transformation in (2.29), so the expressions in (2.32) become the ones in (2.34).

$$\begin{aligned} V_{dr} &= \boldsymbol{S_{dq}}^{\mathsf{T}} \underline{\boldsymbol{U}}_{\boldsymbol{pcc}} \\ \underline{\boldsymbol{I}}_{\boldsymbol{r}} &= \boldsymbol{S_{dq}} I_{dc} \end{aligned} \tag{2.34}$$

where the switching vector $\boldsymbol{S_{dq}}$ is as follows:

$$\boldsymbol{S_{dq}} = \boldsymbol{T}(\theta(t))\boldsymbol{S_{abc}} = [S_d \quad S_q]^{\mathsf{T}} = \frac{3\sqrt{2}}{\pi} n_b k_{\alpha,\mu} [\cos(\delta - \varphi) \quad \sin(\delta - \varphi)]^{\mathsf{T}} \tag{2.35}$$

where δ, which is shown in Figure 2.7, is the angle between the voltage vector $\underline{\boldsymbol{U}}_{\boldsymbol{pcc}}$ and the synchronous reference frame, *i.e.* the angle of $\underline{\boldsymbol{U}}_{\boldsymbol{pcc}}$.

Then, the equations in (2.34) can be expressed in its dq components as it is defined in (2.36). Note that the combination of (2.31) and (2.36) can be graphically expressed by the ideal transformer model shown in Figure 2.8.

$$\begin{aligned} V_{dr} &= S_d U_{pcc,d} + S_q U_{pcc,q} \\ I_{rd} &= S_d I_{dc} \\ I_{rq} &= S_q I_{dc} \end{aligned} \tag{2.36}$$

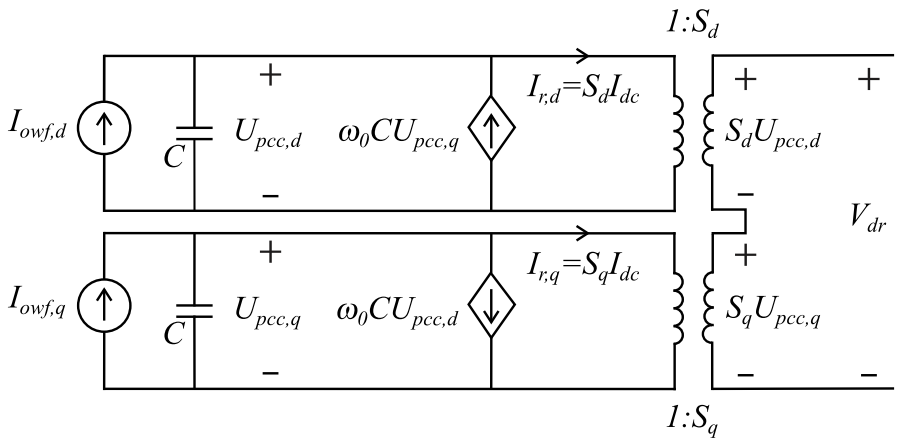

Figure 2.8: AVM in the dq synchronous reference frame.

Therefore, according to (2.36) the AVM main equations are as follows:

$$I_{owf,d} - S_d I_{dc} = C\frac{dU_{pcc,d}}{dt} - \omega_0 C U_{pcc,q}$$

$$I_{owf,q} - S_q I_{dc} = C\frac{dU_{pcc,q}}{dt} + \omega_0 C U_{pcc,d}$$

$$V_{dr} = S_d U_{pcc,d} + S_q U_{pcc,q} \tag{2.37}$$

Finally, this model can be expressed in the per-unit system defined in (2.9) to (2.14), so its main equations are as follows:

$$\frac{b_c}{\omega_0}\frac{du_{pcc,d}}{dt} = i_{owf,d} - \underbrace{k_{\alpha,\mu} i_{dc}\cos(\delta-\varphi)}_{i_{r,d}} + b_c u_{pcc,q} \tag{2.38}$$

$$\frac{b_c}{\omega_0}\frac{du_{pcc,q}}{dt} = i_{owf,q} - \underbrace{k_{\alpha,\mu} i_{dc}\sin(\delta-\varphi)}_{i_{r,q}} - b_c u_{pcc,d} \tag{2.39}$$

$$v_{dr} = k_{\alpha,\mu}\Big(u_{pcc,d}\cos(\delta-\varphi) + u_{pcc,q}\sin(\delta-\varphi)\Big) \tag{2.40}$$

where $b_c = \omega_0 C Z_{base,AC}$ is the capacitor bank C per-unit susceptance.

2.3.2.2 Polar coordinates AVM

The synchronous reference frame AVM has the dq components of the PCC voltage vector as state variables. However, the proposed model is transformed from Cartesian coordinates to polar coordinates in this section. Therefore, the state variables change from $u_{pcc,d}$ and $u_{pcc,q}$ to the voltage vector magnitude u_{pcc} and angle δ. Then, both the model state variables are directly related to the voltage and frequency control which should be applied to the OWF and they will be useful to derive the control strategies. In addition, the inputs of the model will change from currents to powers, which correspond to the conventional output variables of the WTGSs.

The relation between the Cartesian and polar coordinates is set in (2.41).

$$u_{pcc,d} = u_{pcc}\cos\delta$$

$$u_{pcc,q} = u_{pcc}\sin\delta \tag{2.41}$$

Then, the derivatives of the Cartesian coordinates can be developed based on the polar coordinates ones as follows:

$$\frac{du_{pcc,d}}{dt} = \frac{d(u_{pcc}\cos\delta)}{dt} = \cos\delta\frac{du_{pcc}}{dt} - u_{pcc}\sin\delta\frac{d\delta}{dt} = \frac{u_{pcc,d}}{u_{pcc}}\frac{du_{pcc}}{dt} - u_{pcc,q}\frac{d\delta}{dt}$$

$$\frac{du_{pcc,q}}{dt} = \frac{d(u_{pcc}\sin\delta)}{dt} = \sin\delta\frac{du_{pcc}}{dt} + u_{pcc}\cos\delta\frac{d\delta}{dt} = \frac{u_{pcc,q}}{u_{pcc}}\frac{du_{pcc}}{dt} + u_{pcc,d}\frac{d\delta}{dt} \quad (2.42)$$

Therefore, the equations to obtain the polar coordinates derivatives from the Cartesian coordinates derivatives can be obtained and are addressed in (2.43).

$$\frac{du_{pcc}}{dt} = \frac{1}{u_{pcc}}\left(u_{pcc,d}\frac{du_{pcc,d}}{dt} + u_{pcc,q}\frac{du_{pcc,q}}{dt}\right)$$

$$\frac{d\delta}{dt} = \frac{1}{u_{pcc}^2}\left(-u_{pcc,q}\frac{du_{pcc,d}}{dt} + u_{pcc,d}\frac{du_{pcc,q}}{dt}\right) \quad (2.43)$$

Finally, (2.38) and (2.39) are introduced in (2.43) as follows:

$$u_{pcc}\frac{du_{pcc}}{dt} = u_{pcc,d}\left(\frac{\omega_0}{b_c}(i_{owf,d} - i_{r,d} + b_c u_{pcc,q})\right) + u_{pcc,q}\left(\frac{\omega_0}{b_c}(i_{owf,q} - i_{r,q} - b_c u_{pcc,d})\right)$$

$$\rightarrow \frac{b_c u_{pcc}}{\omega_0}\frac{du_{pcc}}{dt} = \underbrace{u_{pcc,d}i_{owf,d} + u_{pcc,q}i_{owf,q}}_{p_{owf}} - \underbrace{(u_{pcc,d}i_{r,d} + u_{pcc,q}i_{r,q})}_{p_r} \quad (2.44)$$

$$u_{pcc}^2\frac{d\delta}{dt} = -u_{pcc,q}\left(\frac{\omega_0}{b_c}(i_{owf,d} - i_{r,d} + b_c u_{pcc,q})\right) + u_{pcc,d}\left(\frac{\omega_0}{b_c}(i_{owf,q} - i_{r,q} - b_c u_{pcc,d})\right)$$

$$\rightarrow \frac{b_c u_{pcc}^2}{\omega_0}\frac{d\delta}{dt} = \underbrace{-u_{pcc,q}i_{owf,d} + u_{pcc,d}i_{owf,q}}_{-q_{owf}} + \underbrace{u_{pcc,q}i_{r,d} - u_{pcc,d}i_{r,q}}_{q_r} - \underbrace{b_c u_{pcc,d}^2}_{q_c} \quad (2.45)$$

where q_c is the reactive power generated by the capacitor bank C connected to the PCC bus.

Therefore, the polar coordinates AVM equations are as follows, considering also the expression in (2.15):

$$\frac{b_c u_{pcc}}{\omega_0}\frac{du_{pcc}}{dt} = p_{owf} - p_r = p_{owf} - k_{\alpha,\mu}u_{pcc}i_{dc}\cos\varphi$$

$$\frac{b_c u_{pcc}^2}{\omega_0}\frac{d\delta}{dt} = -q_{owf} + q_r - q_c = -q_{owf} + k_{\alpha,\mu}u_{pcc}i_{dc}\sin\varphi - q_c$$

$$v_{dr} = k_{\alpha,\mu}u_{pcc}\cos\varphi \quad (2.46)$$

The final polar coordinates AVM is composed by equations (2.46), (2.3) and (2.17) to (2.19) and its inputs and outputs diagram is shown in Figure 2.9. It is worth noting that (2.46) establishes that the active and reactive power balances at the PCC bus determine the dynamics of both the PCC bus voltage magnitude and voltage angle, respectively.

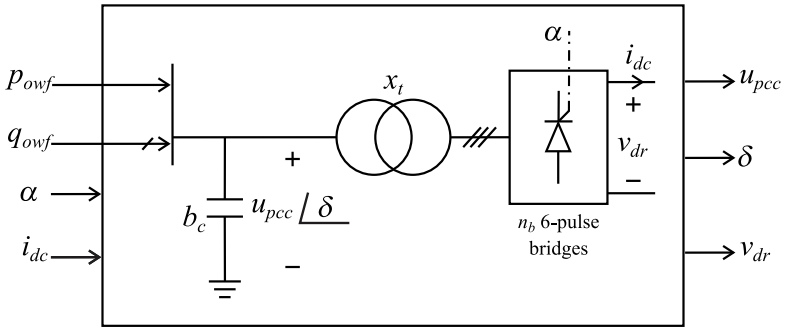

Figure 2.9: Proposed AVM inputs and outputs diagram.

2.3.3 Small-signal frequency-domain validation of the proposed AVM

As it was introduced in Chapter 1, offshore AC voltage and frequency have to be controlled in order to make the LCC rectifier operation possible in isolated OWF applications. For this reason, the proposed AVM validation is accomplished by connecting its AC side to the Thévenin equivalent of an AC grid. Therefore, no additional control is required and an open-loop validation of the model is presented. Moreover, the DC part of the AVM is connected to the T-model of the HVDC cable and the HVDC inverter model addressed in Section 2.2. The studied system is shown in per-unit in Figure 2.10. As it can be observed in Figure 2.10, $\underline{\boldsymbol{v}}_{\boldsymbol{th}}$ is the thevenin voltage vector while r_{th} and x_{th} are the resistance and reactance of the Thévenin impedance, respectively.

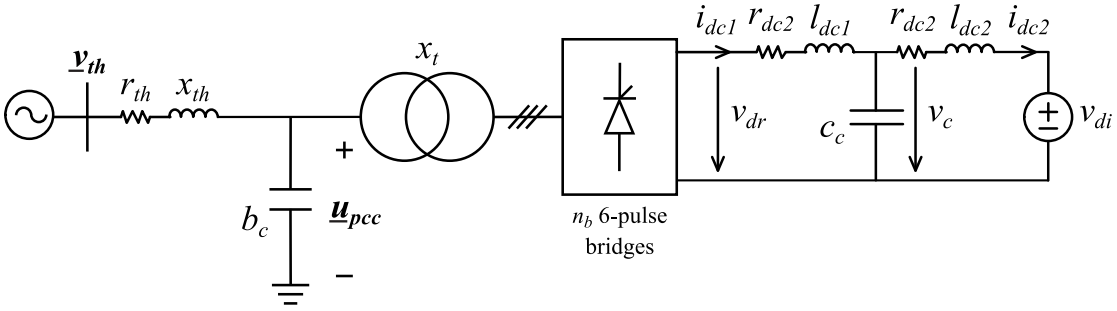

Figure 2.10: System considered for the proposed AVM validation.

The AVM will be used along this Thesis with this T-model of the HVDC link, but the Thévenin equivalent will not be used again. For the sake of clarity, the system in Figure 2.10 is divided in two models in this section. These models are individually addressed following and they will be finally interconnected in order to obtain the total small-signal model.

2.3.3.1 Small-signal model of the Thévenin equivalent

The Thévenin AC grid equivalent model inputs and outputs diagram is depicted in Figure 2.11. As it can be observed in Figure 2.11, Cartesian coordinates are used for the Thévenin bus voltage vector ($\underline{\boldsymbol{v_{th}}} = v_{th,d} + jv_{th,q}$) while polar coordinates are still used for the PCC bus voltage vector definition. Although the current injected by the Thévenin equivalent ($\underline{\boldsymbol{i_{th}}} = i_{th,d} + ji_{th,q}$) is part of the model, its outputs are the active and reactive powers injected (p_{th} and q_{th}, respectively) in order to fit the inputs of the proposed AVM they will be connected to.

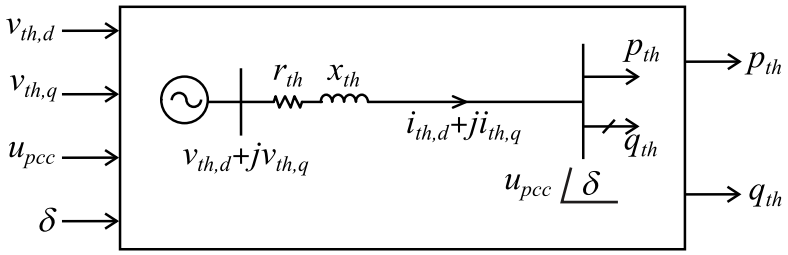

Figure 2.11: Thévenin AC grid equivalent inputs and outputs diagram.

According to the model, there are two state variables which correspond to the dq components of the current vector $\underline{\boldsymbol{i_{th}}}$. The dynamic equations of these states are defined by the inductor equations as follows:

$$\begin{aligned}\frac{di_{th,d}}{dt} &= \frac{\omega_0}{x_{th}}\left(v_{th,d} - u_{pcc}\cos\delta - r_{th}i_{th,d} + x_{th}i_{th,q}\right)\\ \frac{di_{th,q}}{dt} &= \frac{\omega_0}{x_{th}}\left(v_{th,q} - u_{pcc}\sin\delta - r_{th}i_{th,q} - x_{th}i_{th,d}\right)\end{aligned} \tag{2.47}$$

The equations of the output powers are as follows:

$$\begin{aligned}p_{th} &= u_{pcc}i_{th,d}\cos\delta + u_{pcc}i_{th,q}\sin\delta\\ q_{th} &= u_{pcc}i_{th,d}\sin\delta - u_{pcc}i_{th,q}\cos\delta\end{aligned} \tag{2.48}$$

Therefore, the Thévenin equivalent small-signal model can be obtained and it is shown in (2.49). Note that this Thévenin small-signal model is denoted by the subscript th. Its inputs, outputs and states are $\boldsymbol{\Delta u_{th}}$=$[\Delta v_{th,d}, \Delta v_{th,q}, \Delta u_{pcc}, \Delta\delta]^\mathsf{T}$, $\boldsymbol{\Delta y_{th}}$=$[\Delta p_{th}, \Delta q_{th}]^\mathsf{T}$ and $\boldsymbol{\Delta x_{th}}$=$[\Delta i_{th,d}, \Delta i_{th,q}]^\mathsf{T}$, respectively.

$$\begin{aligned}\frac{d\boldsymbol{\Delta x_{th}}}{dt} &= \boldsymbol{A_{th}\Delta x_{th}} + \boldsymbol{B_{th}\Delta u_{th}}\\ \boldsymbol{\Delta y_{th}} &= \boldsymbol{C_{th}\Delta x_{th}} + \boldsymbol{D_{th}\Delta u_{th}}\end{aligned} \tag{2.49}$$

where $\boldsymbol{A_{th}}$, $\boldsymbol{B_{th}}$, $\boldsymbol{C_{th}}$ and $\boldsymbol{D_{th}}$ are as follows:

$$\boldsymbol{A_{th}} = \begin{bmatrix} -\dfrac{r_{th}\omega_0}{x_{th}} & \omega_0 \\ -\omega_0 & -\dfrac{r_{th}\omega_0}{x_{th}} \end{bmatrix}$$

$$\boldsymbol{B_{th}} = \begin{bmatrix} \dfrac{\omega_0}{x_{th}} & 0 & -\dfrac{\omega_0 \cos\delta_0}{x_{th}} & \dfrac{\omega_0 u_{pcc0} \sin\delta_0}{x_{th}} \\ 0 & \dfrac{\omega_0}{x_{th}} & -\dfrac{\omega_0 \sin\delta_0}{x_{th}} & -\dfrac{\omega_0 u_{pcc0} \cos\delta_0}{x_{th}} \end{bmatrix}$$

$$\boldsymbol{C_{th}} = \begin{bmatrix} u_{pcc0}\cos\delta_0 & u_{pcc0}\sin\delta_0 \\ u_{pcc0}\sin\delta_0 & -u_{pcc0}cos\delta_0 \end{bmatrix}$$

$$\boldsymbol{D_{th}} = \begin{bmatrix} 0 & 0 & i_{th,d0}\cos\delta_0 + i_{th,q0}\sin\delta_0 & u_{pcc0}(-i_{th,d0}\sin\delta_0 + i_{th,q0}\cos\delta_0) \\ 0 & 0 & i_{th,d0}\sin\delta_0 - i_{th,q0}\cos\delta_0 & u_{pcc0}(i_{th,d0}\cos\delta_0 + i_{th,q0}\sin\delta_0) \end{bmatrix} \quad (2.50)$$

2.3.3.2 Small-signal model of the HVDC link considering the proposed AVM

The model considered here is a combination of the LCC rectifier and transformer AVM proposed in Section 2.3.2 and the HVDC link inverter and T-modeled cable presented in Section 2.2. Figure 2.12 shows the inputs and outputs of the considered model.

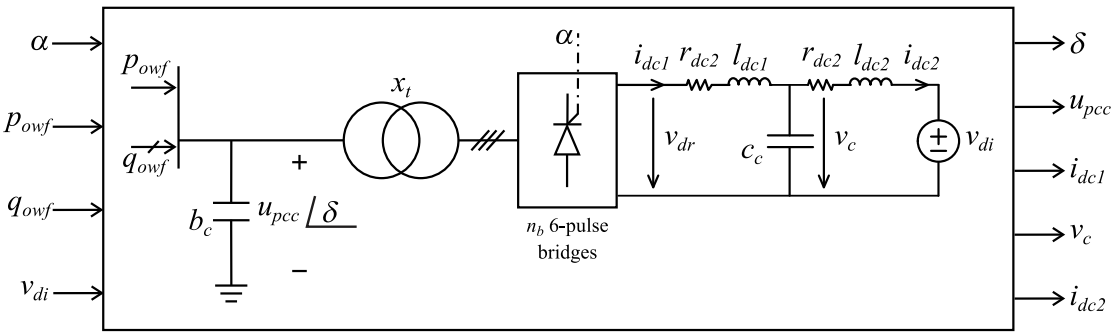

Figure 2.12: Inputs and outputs diagram of the T-modeled HVDC link which includes the proposed LCC rectifier AVM.

Therefore, the equations of the model in Figure 2.12 are the combination of the algebraic equations (2.3) and (2.17) to (2.19) and the dynamic equations in (2.51), which have been obtained by properly merging (2.46) and (2.22).

$$\frac{1}{\omega_0}\frac{d\delta}{dt} = \frac{-q_{owf}+q_r}{q_c} - 1 = \frac{-q_{owf}}{b_c u_{pcc}^2} + \frac{k_{\alpha,\mu} i_{dc1}\sin\varphi}{b_c u_{pcc}} - 1$$

$$\frac{1}{\omega_0}\frac{du_{pcc}}{dt} = \frac{u_{pcc}}{q_c}(p_{owf}-p_r) = \frac{p_{owf}}{b_c u_{pcc}} - \frac{k_{\alpha,\mu} i_{dc1}\cos\varphi}{b_c}$$

$$\frac{1}{\omega_0}\frac{di_{dc1}}{dt} = \frac{k_{\alpha,\mu} u_{pcc}\cos\varphi - v_c - r_{dc1} i_{dc1}}{l_{dc1}}$$

$$\frac{1}{\omega_0}\frac{dv_c}{dt} = \frac{i_{dc1}-i_{dc2}}{c_c}$$

$$\frac{1}{\omega_0}\frac{di_{dc2}}{dt} = \frac{v_c - v_{di} - r_{dc2} i_{dc2}}{l_{dc2}} \tag{2.51}$$

Once the equations of the model are defined, the small-signal model can be obtained and it is shown in (2.52). $\boldsymbol{\Delta u_{pr}} = [\Delta\alpha, \Delta p_{owf}, \Delta q_{owf}, \Delta v_{di}]^\mathsf{T}$, $\boldsymbol{\Delta y_{pr}}$=$[\Delta\delta, \Delta u_{pcc}, \Delta i_{dc1}, \Delta v_c, \Delta i_{dc2}]^\mathsf{T}$ and $\boldsymbol{\Delta x_{pr}}$=$[\Delta\delta, \Delta u_{pcc}, \Delta i_{dc1}, \Delta v_c, \Delta i_{dc2}]^\mathsf{T}$ are its inputs, outputs and states, respectively. Note that the subscript pr is used to denote the small-signal model of the proposed rectifier station and HVDC link.

$$\frac{1}{\omega_0}\frac{d\boldsymbol{\Delta x_{pr}}}{dt} = \boldsymbol{A_{pr}}\boldsymbol{\Delta x_{pr}} + \boldsymbol{B_{pr}}\boldsymbol{\Delta u_{pr}}$$

$$\boldsymbol{\Delta y_{pr}} = \boldsymbol{C_{pr}}\boldsymbol{\Delta x_{pr}} + \boldsymbol{D_{pr}}\boldsymbol{\Delta u_{pr}} \tag{2.52}$$

where $\boldsymbol{A_{pr}}$, $\boldsymbol{B_{pr}}$, $\boldsymbol{C_{pr}}$ and $\boldsymbol{D_{pr}}$ are as follows:

$$\boldsymbol{A_{pr}} = \begin{bmatrix} 0 & a_{pr,12} & a_{pr,13} & 0 & 0 \\ 0 & a_{pr,22} & a_{pr,23} & 0 & 0 \\ 0 & a_{pr,32} & a_{pr,33} & -\frac{1}{l_{dc1}} & 0 \\ 0 & 0 & \frac{1}{c_c} & 0 & -\frac{1}{c_c} \\ 0 & 0 & 0 & \frac{1}{l_{dc2}} & -\frac{r_{dc2}}{l_{dc2}} \end{bmatrix}$$

$$\boldsymbol{B_{pr}} = \begin{bmatrix} \frac{p_{owf0}}{q_{c0}}\zeta_{\alpha_0} & 0 & -\frac{1}{q_{c0}} & 0 \\ u_{pcc0}\frac{q_{r0}}{q_{c0}}\zeta_{\alpha_0} & \frac{u_{pcc0}}{q_{c0}} & 0 & 0 \\ -\frac{k_{\alpha,\mu}u_{pcc0}\sin\varphi_0}{l_{dc1}}\zeta_{\alpha_0} & 0 & 0 & 0 \\ 0 & 0 & 0 & 0 \\ 0 & 0 & 0 & -\frac{1}{l_{dc2}} \end{bmatrix}$$

$$\boldsymbol{C_{pr}} = \begin{bmatrix} 1 & 0 & 0 & 0 & 0 \\ 0 & 1 & 0 & 0 & 0 \\ 0 & 0 & 1 & 0 & 0 \\ 0 & 0 & 0 & 1 & 0 \\ 0 & 0 & 0 & 0 & 1 \end{bmatrix}$$

$$\boldsymbol{D_{pr}} = \begin{bmatrix} 0 & 0 & 0 & 0 \\ 0 & 0 & 0 & 0 \\ 0 & 0 & 0 & 0 \\ 0 & 0 & 0 & 0 \\ 0 & 0 & 0 & 0 \end{bmatrix} \tag{2.53}$$

where $\zeta_{u_{pcc0}}$, $\zeta_{i_{dc10}}$ and ζ_{α_0} are defined in (2.28). $a_{pr,12}$, $a_{pr,13}$, $a_{pr,22}$, $a_{pr,23}$, $a_{pr,32}$ and $a_{pr,33}$ are as follows:

$$a_{pr,12} = \frac{1}{u_{pcc0}}\left(\frac{q_{r0}}{q_{c0}} - 2\right) + \frac{p_{owf0}}{q_{c0}}\zeta_{u_{pcc0}}$$

$$a_{pr,13} = \frac{k_{\alpha,\mu}u_{pcc0}\sin\varphi_0}{q_{c0}} + \frac{p_{owf0}}{q_{c0}}\zeta_{i_{dc10}}$$

$$a_{pr,22} = -\frac{p_{owf0}}{q_{c0}} + u_{pcc0}\frac{q_{r0}}{q_{c0}}\zeta_{u_{pcc0}}$$

$$a_{pr,23} = -\frac{k_{\alpha,\mu}u_{pcc0}^2\cos\varphi_0}{q_{c0}} + u_{pcc0}\frac{q_{r0}}{q_{c0}}\zeta_{i_{dc10}}$$

$$a_{pr,32} = \frac{k_{\alpha,\mu}}{l_{dc1}}\left(\cos\varphi_0 - u_{pcc0}\sin\varphi_0\zeta_{u_{pcc0}}\right)$$

$$a_{pr,33} = -\frac{1}{l_{dc1}}\left(r_{dc1} + k_{\alpha,\mu}u_{pcc0}\sin\varphi_0\zeta_{i_{dc10}}\right) \tag{2.54}$$

2.3.3.3 Small-signal validation

This section seeks the small-signal frequency-domain validation of the proposed model. This will be accomplished by comparing the frequency response analysis (FRA) of both the DSM built in PSIM and the analytical small-signal model obtained, which is addressed following.

Once the small-signal models of the Thévenin equivalent and the HVDC system have been obtained in Section 2.3.3.1 and 2.3.3.2, respectively, the small-signal of the considered model can be also obtained. Therefore, the full small-signal model has been calculated by considering the interconnections between the two submodels which are shown in Figure 2.13.

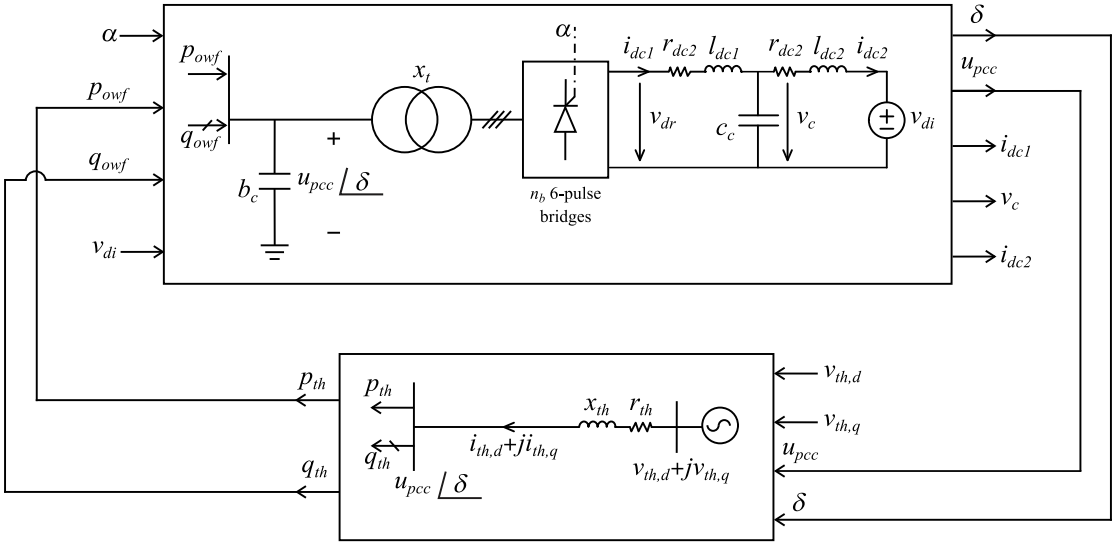

Figure 2.13: Interconnection of the submodels considered for the small-signal frequency-domain validation of the proposed AVM.

Therefore, the model is validated in both the diode rectifier and the thyristor rectifier versions. The FRA is performed around a steady-state point defined by p_{owf0} equal to 0.4 p.u. Note that the thyristor rectifier study case also has the firing angle degree of freedom, so u_{pcc} is decided to be 1 p.u. The Thévenin equivalent impedance parameters are r_{th}=0.005 p.u. and x_{th}=0.05 p.u. The rest of the parameters can be found in Table 2.2 and they have been obtained from the HVDC Benchmark model [4]. Note that the inverter DC voltage value is changed depending on the LCC rectifier semiconductor which is used.

In order to obtain the DSM FRA, the AC sweep tool of PSIM is used. The transfer function analyzed is the one between the rectifier DC current (i_{dc1}) and the Thévenin equivalent voltage magnitude ($v_{th,d}$ given that zero $v_{th,q}$ is considered). The results are presented in Figure 2.14a for the diode rectifier case and in Figure 2.14b for the thyristor rectifier case.

Table 2.2: Parameters used for the HVDC link with the proposed LCC rectifier AVM.

Parameter	Value	Parameter	Value
n_b	2 6-pulse bridges	$S_{base,AC}$	1000 MVA
$V_{base,AC}$	211.42 kV	$V_{base,DC}$	571.0346 kV
x_t/n_b	0.1505 p.u.	b_c	0.625 p.u.
$r_{dc1} \equiv r_{dc2}$	0.00765 p.u.	$l_{dc1} \equiv l_{dc2}$	0.57367 p.u.
c_c	2.66347 p.u.	f_0	50 Hz
v_{di} (diode)	0.9529 p.u.	v_{di} (thyristor)	0.855 p.u.

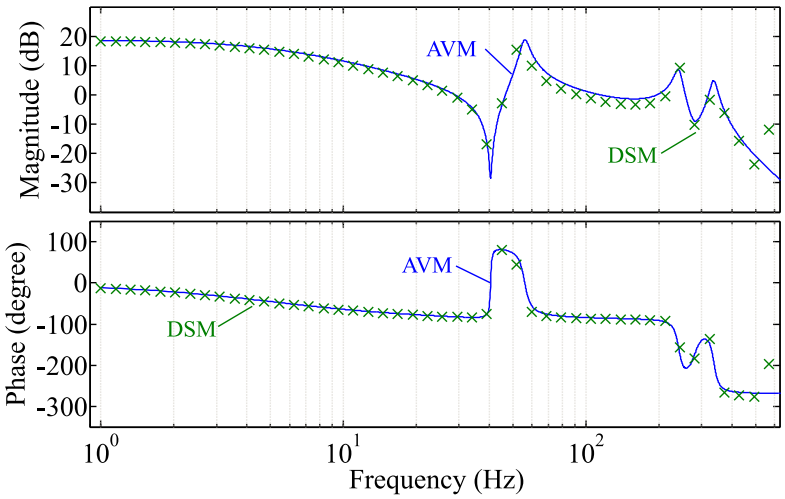

(a) Diode rectifier study case.

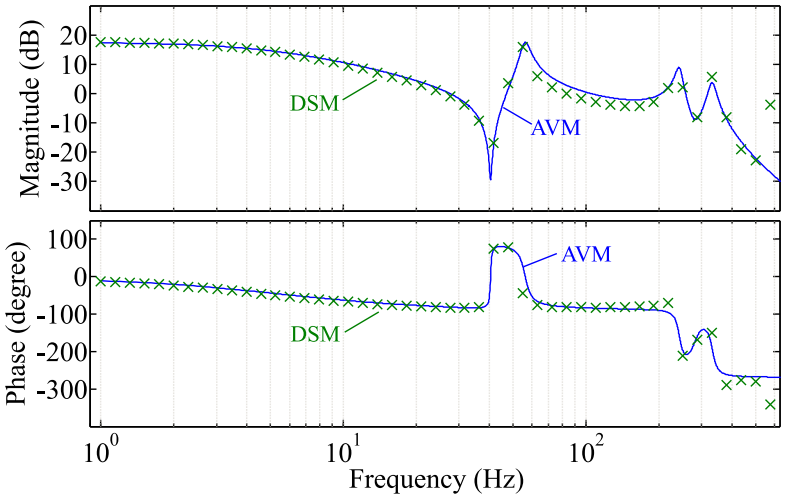

(b) Thyristor rectifier study case.

Figure 2.14: Frequency response of the transfer function between the rectifier DC current and the grid voltage magnitude with the proposed AVM and the DSM representation.

Figure 2.14 shows that in both the diode and the thyristor rectifier cases the AVM frequency response is accurate compared to the DSM one. It is worth mentioning that the switching frequency of this system is equal to 600 Hz. This is due to the fact that a twelve-pulse rectifier is used (n_b equals 2) and the AC system frequency is 50 Hz. According to Figure 2.14, the frequency responses differ when the frequency is close to or above the switching frequency. However, this is the expected result with the considered assumptions, which are no valid for frequencies close to and above the switching frequency [9].

2.4 WTGS model

The WTGSs conventional output control variables are its active and reactive powers. The active power will usually follow the WTGS power curve if there is no deloaded operation due to frequency support [24] or power curtailment command [25]. The reactive power is completely decoupled and it can follow different control strategies. For instance, remote voltage control or power factor control [26] can be of interest.

For this reason, both single WTGS aggregated models used along this Thesis only represent the WTGS by its active and reactive power injection, which can correspond to both type-3 and type-4 WTGS technologies. However, there are study cases in Chapter 4 where the WTGSs are considered to be type-4 and they are modeled as it is shown in Figure 2.15. Note that the subscript k is used for the WTGS identification number along this Thesis when there are several WTGSs. The BEC is represented by the active power p_{kdc} injected to the WTGS DC link. The DC link voltage at the capacitor c_{dc} is v_{kdc}, being i_{kdc} the DC current extracted by the FEC. Moreover, overvoltage protection is provided by a crowbar with resistance r_{cb}. AC variables are represented in three phase, being the FEC output voltage and current vectors $\boldsymbol{v_{k,abc}}$ and $\boldsymbol{i_{k,abc}}$, respectively. The FEC output filter is made of a series inductor with reactance x_f and a parallel capacitor with susceptance b_f. Therefore, the output voltage and current of the WTGS are $\boldsymbol{u_{k,abc}}$ and $\boldsymbol{i_{ok,abc}}$, respectively. The generated active power is p_k and the generated reactive power is q_k.

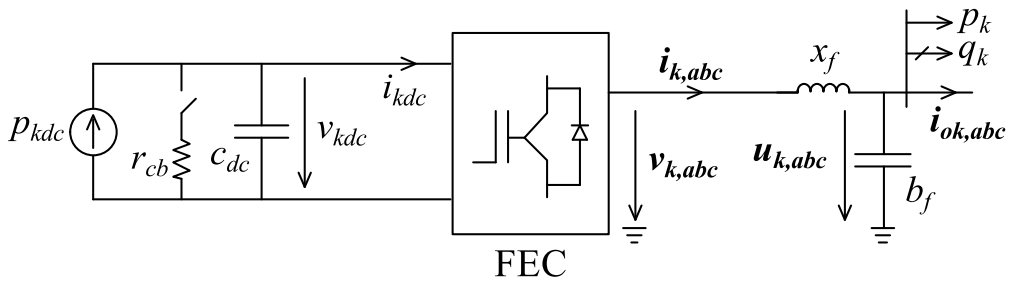

Figure 2.15: Type-4 WTGS model.

The small-signal model of this WTGS model will be derived in Chapter 4, together

with the proposed decentralized control, in order to assess the stability analysis of the proposal. Additional equations for the FEC DC parameters definition, which depend on the WTGS nominal values which are in turn considered the base values, are as follows:

$$V_{WTGSbase,DC} = \frac{2\sqrt{2}}{\sqrt{3}} V_{WTGSbase,AC} \tag{2.55}$$

$$P_{WTGSbase,DC} = S_{WTGSbase,AC} \tag{2.56}$$

$$c_{dc} = \omega_0 C_{dc} \frac{V^2_{WTGSbase,DC}}{P_{WTGSbase,DC}} \tag{2.57}$$

2.5 Conclusions

In this chapter, the models of the main elements which will be used in the layouts studied in this Thesis have been presented.

AVMs are useful to study the power electronics systems because they avoid the discontinuous nature of the DSMs and reduce the computing time required for the studies. Among the existing LCC rectifier AVMs, there is no proper AVM that considers the dynamics of the capacitor bank located at the PCC bus. Therefore, an enhanced LCC rectifier AVM is proposed in this chapter.

The main advantages of the proposed AVM are its inputs and state variables. The inputs are the active and reactive powers that are injected from the AC grid. Given that WTGSs conventional output variables are their active and reactive powers, there is a match between the natural outputs of the OWF and the AVM inputs. Moreover, the state variables of the model are the PCC bus voltage magnitude and angle. This is quite important because OWFs connected through LCC-rectifier-based HVDC links need a voltage and frequency control in the isolated offshore AC grid. Therefore, these states facilitate the derivation of a decoupled voltage and frequency control strategy which will be presented in Chapter 3.

Finally, the proposed AVM allows the study of the dynamic response of the HVDC link and the devices connected to the AC grid by a static consideration of the complete topology of the AC grid. It needs an iterative process where the rectifier AC bus is considered as the slack bus in the AC grid load flow. Therefore, the active and reactive power which are the load flow result are the inputs to the dynamic AVM which will provide the new slack bus voltage magnitude and angle. Then, the load flow is again run in this iterative solution.

2.6 Bibliography

[1] W. Europe. *Offshore Wind in Europe. Key trends and statistics 2017*. 2018. URL: https://windeurope.org/wp-content/uploads/files/about-wind/statistics/WindEurope-Annual-Offshore-Statistics-2017.pdf (visited on 05/10/2018) (cit. on p. 22).

[2] R. Blasco-Gimenez et al. "Distributed voltage and frequency control of offshore wind farms connected with a diode-based HVdc link". In: *Power Electronics, IEEE Transactions on* 25.12 (2010), pp. 3095–3105 (cit. on p. 23).

[3] M. Abouzlam et al. "Identification of a HVDC cable model with coupling between core and screen". In: *IFAC-PapersOnLine* 48.28 (2015), pp. 1433–1438 (cit. on p. 23).

[4] M Szechtman, T Wess, and C. Thio. "A benchmark model for HVDC system studies". In: *AC and DC Power Transmission, 1991., International Conference on*. IET. 1991, pp. 374–378 (cit. on pp. 23, 42).

[5] S Chiniforoosh et al. "Definitions and applications of dynamic average models for analysis of power systems". In: *IEEE Transactions on Power Delivery* 25.4 (2010), pp. 2655–2669 (cit. on p. 23).

[6] S. D. Sudhoff and O. Wasynczuk. "Analysis and average-value modeling of line-commutated converter-synchronous machine systems". In: *IEEE transactions on energy conversion* 8.1 (1993), pp. 92–99 (cit. on p. 24).

[7] S. Sudhoff et al. "Transient and dynamic average-value modeling of synchronous machine fed load-commutated converters". In: *IEEE Transactions on Energy Conversion* 11.3 (1996), pp. 508–514 (cit. on p. 24).

[8] J. Alt, S. Sudhoff, and B. Ladd. "Analysis and average-value modeling of an inductorless synchronous machine load commutated converter system". In: *IEEE transactions on energy conversion* 14.1 (1999), pp. 37–43 (cit. on p. 24).

[9] J. Jatskevich, S. D. Pekarek, and A. Davoudi. "Parametric average-value model of synchronous machine-rectifier systems". In: *IEEE transactions on energy conversion* 21.1 (2006), pp. 9–18 (cit. on pp. 24, 44).

[10] J. Jatskevich, S. D. Pekarek, and A. Davoudi. "Fast procedure for constructing an accurate dynamic average-value model of synchronous machine-rectifier systems". In: *IEEE Transactions on Energy Conversion* 21.2 (2006), pp. 435–441 (cit. on p. 24).

[11] H Atighechi et al. "Dynamic average-value modeling of CIGRE HVDC benchmark system". In: *IEEE Transactions on Power Delivery* 29.5 (2014), pp. 2046–2054 (cit. on p. 24).

[12] H. Atighechi et al. "Using current-source formulation for dynamic average-value modeling of inverter side HVDC system". In: *Electrical and Computer Engineering (CCECE), 2013 26th Annual IEEE Canadian Conference on*. IEEE. 2013, pp. 1–4 (cit. on p. 24).

[13] H. Atighechi et al. "Using Multiple Reference Frame Theory for Considering Harmonics in Average-Value Modeling of Diode Rectifiers". In: *IEEE Transactions on Energy Conversion* 31.3 (2016), pp. 872–881 (cit. on p. 24).

[14] S. Chiniforoosh et al. "Dynamic average modeling of front-end diode rectifier loads considering discontinuous conduction mode and unbalanced operation". In: *IEEE Transactions on Power Delivery* 27.1 (2012), pp. 421–429 (cit. on p. 24).

[15] K Chaijarurnudomrung, K.-N. Areerak, and K.-L. Areerak. "Modeling of Three-phase Controlled Rectifier using a DQ method". In: *Advances in Energy Engineering (ICAEE), 2010 International Conference on*. IEEE. 2010, pp. 56–59 (cit. on p. 24).

[16] E. W. Kimbark. *Direct current transmission*. Vol. 1. John Wiley & Sons, 1971 (cit. on pp. 24, 26).

[17] M. Daryabak et al. "Modeling of LCC-HVDC systems using dynamic phasors". In: *Power Delivery, IEEE Transactions on* 29.4 (2014), pp. 1989–1998 (cit. on p. 24).

[18] Y. Huang et al. "A parametric dynamic phasor model of line-commutated rectifier systems". In: *Electrical and Computer Engineering (CCECE), 2016 IEEE Canadian Conference on*. IEEE. 2016, pp. 1–4 (cit. on p. 24).

[19] Y. Huang et al. "Interfacing SFA-and GAM-type dynamic phasors for modeling of integrated AC-DC power systems". In: *Power and Energy Society General Meeting (PESGM), 2016*. IEEE. 2016, pp. 1–5 (cit. on p. 24).

[20] M. Guan et al. "Synchronous generator emulation control strategy for voltage source converter (VSC) stations". In: *IEEE Transactions on Power Systems* 30.6 (2015), pp. 3093–3101 (cit. on pp. 24, 32).

[21] L. M. Castro, E. Acha, and C. R. Fuerte-Esquivel. "A novel VSC-HVDC link model for dynamic power system simulations". In: *Electric Power Systems Research* 126 (2015), pp. 111–120 (cit. on p. 24).

[22] B. Wu and M. Narimani. *High-power converters and AC drives*. Vol. 59. John Wiley & Sons, 2017 (cit. on p. 25).

[23] X.-F. Wang, Y. Song, and M. Irving. *Modern power systems analysis*. Springer Science & Business Media, 2010 (cit. on pp. 26, 29).

[24] F. Díaz-González et al. "Participation of wind power plants in system frequency control: Review of grid code requirements and control methods". In: *Renewable and Sustainable Energy Reviews* 34 (2014), pp. 551–564 (cit. on p. 44).

[25] J. L. Rodriguez-Amenedo, S. Arnalte, and J. C. Burgos. "Automatic generation control of a wind farm with variable speed wind turbines". In: *Energy Conversion, IEEE Transactions on* 17.2 (2002), pp. 279–284 (cit. on p. 44).

[26] P. Sørensen et al. "Progress in IEC 61400-27". In: *11th International Workshop on Large-Scale Integration of Wind Power into Power Systems as well as on Transmission Networks for Offshore Wind Power Plants*. 2012 (cit. on p. 44).

Chapter 3

Centralized voltage and frequency control of OWFs connected to LCC-based Rectifiers

3.1 Introduction

This chapter presents the proposed centralized voltage and frequency control for OWFs which are connected to the onshore grid by an LCC-rectifier-based HVDC link. This control strategy is derived from the AVM proposed in Section 2.3.2, which considers the dynamics of the capacitor bank which is connected to the PCC bus.

The aforementioned model has the incoming active and reactive powers from the offshore AC grid to the PCC bus as inputs. These inputs prove useful given that a single aggregated model of the WTGS, which is directly connected to the PCC bus, will be considered as the OWF layout in this chapter. Moreover, the polar coordinates state variables of the model allow the clear identification of the voltage and frequency dynamics from the proposed AVM equations. In addition, the model equations are obtained in a dq synchronous reference frame which rotates at frequency ω_0, which will be also convenient for the frequency control strategy proposed in this chapter. On the one hand, the alignment of the PCC bus voltage vector to the dq synchronous reference frame can be accomplished by affecting the reactive power balance through reactive power injection to the PCC bus, what leads to the OWF frequency control needed for the LCC rectifier operation. On the other hand, it is also demonstrated that the active power balance at the PCC bus drives the PCC bus voltage magnitude variations. Finally, the structure of this chapter is addressed following.

First, the OWF layout which is used for the centralized voltage and frequency control studies is presented in Section 3.2. Then, the centralized control strategies are derived and presented in Secion 3.3. It is worth mentioning that the LCC semiconductor technology defines the control, given that the voltage control cannot be carried out if a diode rectifier is used. In section 3.4, the controllers design is shown and the stability analysis is performed. Both are based on the small-signal models of the corresponding OWF layout. Then, Section 3.5 shows the performance of the proposed control by using the AVM proposed in Section 2.3.2. Given that the derivation, the analysis and the simulation results of the centralized voltage and frequency control are based on the proposed AVM, the validation of both the control and the AVM are accomplished in Section 3.6 by using a DSM as reference. It should be pointed out that both the small-signal frequency response and the large-signal time response are compared in this validation. Finally, a fault response study is shown in Section 3.7 and the main conclusions are addressed in Section 3.8.

3.2 System description

An overview showing the main elements of the LCC-rectifier-based HVDC connection of an OWF has been presented in Figure 2.1. The OWF layout which is used to represent the system along this chapter is shown in Figure 3.1.

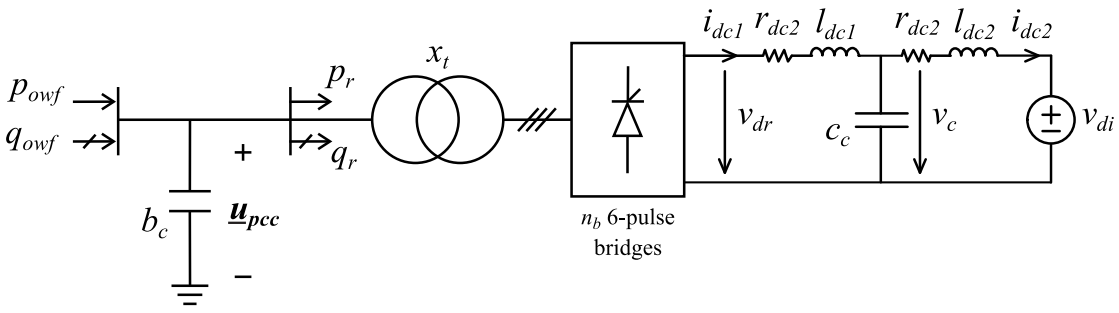

Figure 3.1: OWF equivalent with a single aggregated WTGS and an HVDC composed of a T-modeled cable, the inverter and an LCC rectifier.

There is an LCC rectifier station which includes the rectifier, its transformer and a capacitor bank (with susceptance b_c) which is connected to the PCC bus. This rectifier station AVM has been proposed in Section 2.3.2. It is worth noting that the capacitor bank represents both the fundamental frequency performance of the AC harmonic filters and the reactive power compensation. Moreover, the rest of the HVDC link is modeled by using the equivalent DC voltage source v_{di} for the onshore inverter and the HVDC Benchmark model [1] proposal for the cable (T-model), which have been presented in Section 2.2. Finally, the OWF AC grid is simplified to the output active and reactive powers of a single aggregated WTGS which is directly connected to the OWF PCC bus. Specifically, these active and reactive powers are addressed by p_{owf} and q_{owf}, respectively. As it has been addressed in Chapter 2, this onshore inverter model can represent any of the existing technologies but it is defined by its constant DC voltage operation mode. Likewise, the WTGS output powers representation is accurate for both type-3 and type-4 WTGS technologies.

The system parameters can be found in Table 2.2.

3.3 Centralized voltage and frequency control

The objectives of the centralized voltage and frequency control strategies are to maintain the OWF AC voltage magnitude and frequency at their reference values. As it was established in Chapter 1, this OWF AC grid control is required in order to operate the LCC rectifier. Although the proposed AVM used in the OWF layout studied in this chapter has been proposed in Section 2.3.2, the small-signal model which considers the same HVDC link and WTGSs modeling which are used in this section has already been presented in Section 2.3.3.2. The dynamic equations of this model have been shown in (2.51). According to them, a decoupled voltage and frequency control strategy is derived and presented following.

The control strategies proposed in this section use PI controllers. These controllers will be tuned and the stability and performance of the system will be analyzed in the

following sections.

3.3.1 Centralized frequency control

According to the equation of $\frac{d\delta}{dt}$ which is presented in (2.51), the reactive power balance at the capacitor bank placed at the PCC bus (with susceptance b_c) leads to the dynamic response of the PCC voltage vector angle δ. It is worth noting that this equation might be transformed into another equation which explicitly contains the expression of the OWF AC frequency. This equation is shown in (3.2) and it is derived by combining (2.51) and (3.1).

$$\omega = \omega_0 + \frac{d\delta}{dt} \tag{3.1}$$

$$\frac{\omega}{\omega_0} q_c = -q_{owf} + q_r \tag{3.2}$$

Therefore, these equations clearly indicate that the reactive power balance at the capacitor bank bus is driving the frequency of the PCC voltage vector in the dq synchronous reference frame which rotates at frequency ω_0. This synchronous reference frame is usually obtained by means of a PLL which is measuring the AC voltage, as in VOC strategies [2, 3]. However, the OWF application is slightly different and this kind of strategy would imply that the control is orientated to the AC voltage which the control is simultaneously generating, what could naturally lead to stability issues. However, the dq synchronous frame of the proposed AVM uses a stiff reference frequency signal, ω_0. Therefore, ω_0 has a constant value and the reference angular position is easily obtained by integrating this stiff reference. Therefore, this reference angular position is not subject to any measurement noise, harmonic distortion or other grid disturbance because a PLL is not required. If ω_0 is constant and equal to the desired OWF AC frequency, the frequency control can be guaranteed by keeping a constant angle δ in the PCC bus voltage vector, which is the objective of the proposed frequency control.

The reactive power balance obtained from (3.2) contains both the reactive power provided by the capacitor bank q_c and the reactive power absorbed by the rectifier and transformer q_r, but they cannot be controlled. q_r is provided by a passive element and it could only be controlled to a varying value by controlling the PCC bus voltage magnitude u_{pcc}. q_r mainly depends on the firing angle if thyristors are used in the LCC rectifier and on the active power which is transferred through the HVDC link. The other reactive power which is present in (3.2) is the reactive power delivered by the OWF q_{owf}. It mainly depends on the active power generated, the OWF AC grid topology and the reactive power strategy of the WTGSs. A remote control of q_{owf} could be done through the WTGSs reactive power control strategy, but it requires communication between the PCC bus and the WTGSs so it will not provide the fast control response

required for the frequency variations. Therefore, an additional reactive power injection to the PCC bus is proposed to achieve the frequency control and it will be addressed as q_{ctr}, which can be observed in the system layout depicted in Figure 3.2.

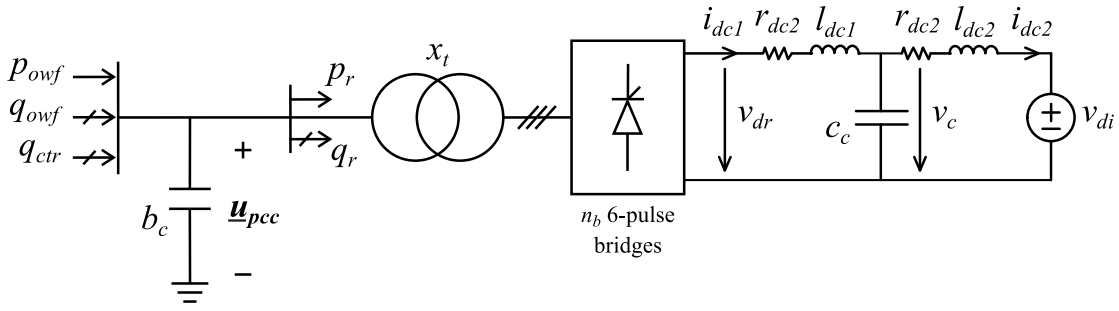

Figure 3.2: OWF equivalent with a single aggregated WTGS, the reactive power injection q_{ctr} for frequency control and an HVDC composed of a T-modeled cable, the inverter and an LCC rectifier.

The addition of q_{ctr} to the system modifies the studied OWF layout to the one shown in Figure 3.2. Moreover, the set of dynamic equations of the OWF layout model which was presented in (2.51) is modified as it is established in (3.3). Likewise, (3.2) becomes (3.4).

$$\frac{1}{\omega_0}\frac{d\delta}{dt} = \frac{-q_{owf} - q_{ctr} + q_r}{q_c} - 1 = \frac{-q_{owf} - q_{ctr}}{b_c u_{pcc}^2} + \frac{k_{\alpha,\mu} i_{dc1} \sin\varphi}{b_c u_{pcc}} - 1$$

$$\frac{1}{\omega_0}\frac{du_{pcc}}{dt} = \frac{u_{pcc}}{q_c}(p_{owf} - p_r) = \frac{p_{owf}}{b_c u_{pcc}} - \frac{k_{\alpha,\mu} i_{dc1} \cos\varphi}{b_c}$$

$$\frac{1}{\omega_0}\frac{di_{dc1}}{dt} = \frac{k_{\alpha,\mu} u_{pcc} \cos\varphi - v_c - r_{dc1} i_{dc1}}{l_{dc1}}$$

$$\frac{1}{\omega_0}\frac{dv_c}{dt} = \frac{i_{dc1} - i_{dc2}}{c_c}$$

$$\frac{1}{\omega_0}\frac{di_{dc2}}{dt} = \frac{v_c - v_{di} - r_{dc2} i_{dc2}}{l_{dc2}} \tag{3.3}$$

$$\frac{\omega}{\omega_0} q_c = -q_{owf} - q_{ctr} + q_r \tag{3.4}$$

Although any constant reference for angle δ would lead to the frequency control, a zero δ control is proposed, because it means a zero q component of the PCC bus voltage vector $\underline{\boldsymbol{u}}_{\boldsymbol{pcc}}$ ($u_{pcc,q}$), being $u_{pcc,d}$ the voltage magnitude. This control is accomplished by a PI regulator which defines the reference value q_{ctr}^{ref}, as it is shown in the frequency control channel depicted at the bottom of Figure 3.3. This reactive power injection must be provided by any of the elements available in the OWF or by an element which is specifically used for this purpose, as a STATCOM.

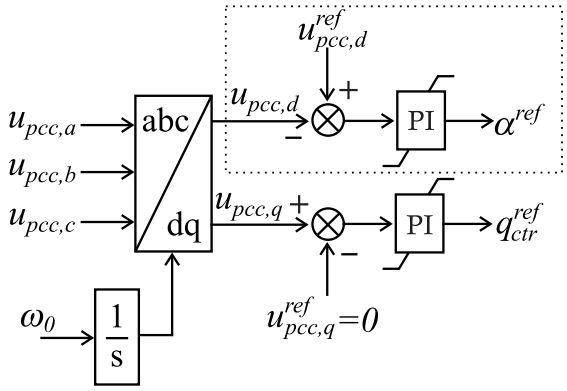

Figure 3.3: Centralized voltage and frequency control strategies.

3.3.2 Centralized voltage control

The equation of $\frac{du_{pcc}}{dt}$ in (3.3) shows that the active power balance at the capacitor bank bus (PCC bus) drives the variations of the OWF AC voltage magnitude. There are two terms in the active power balance: p_{owf} and p_r. The first one is the active power injected from the OWF, which mainly depends on the available wind through the WTGS power curve if there is no power curtailment [4] or deloaded operation due to frequency support [5]. Therefore, it should not be modified for the voltage magnitude control, given that the objective of the OWF application is generating as much power as possible and transferring it to the onshore grid. However, the second term is the active power drawn by the LCC rectifier and it can be easily controlled by modifying the firing angle α. Due to the constant DC voltage operation of the onshore inverter, p_r is decreased when α is increased and vice versa.

As it has been previously established, the PCC voltage vector will be aligned to the dq synchronous reference frame due to the centralized frequency control. Thus, the PCC voltage vector magnitude will be equal to its d component $u_{pcc,d}$. Then, the centralized voltage control strategy regulates $u_{pcc,d}$ to its reference value $u^{ref}_{pcc,d}$ through the firing angle reference α^{ref}, as it is shown at the top of Figure 3.3. Note that this centralized frequency control cannot be applied if a diode rectifier is used in the HVDC link, due to the missing firing angle signal. This is the reason why the centralized voltage control channel is inside dotted lines in Figure 3.3.

Although the voltage magnitude cannot be controlled when a diode rectifier is used in the HVDC link, it will be demonstrated that it will vary between admissible limits. It is worth mentioning that the PCC voltage magnitude steady-state value in the diode-rectifier case depends on the active power transferred through the HVDC link. Its variation range is mainly affected by the total HVDC link resistance, the rectifier transformer inductance and the inverter DC voltage v_{di}.

3.4 Controller design and stability analysis

Due to the non-linear dynamics of the LCC rectifier, the controller parameters of the centralized voltage and frequency control could be tuned by considering the small-signal analysis of the system at each of the possible operating points. However, this technique could be intensely cumbersome and the controllers are designed at a single operating point. Once the controllers design is finished, the stability of the controlled system is checked in the other operating points.

First, the small-signal model of the non-controlled OWF layout in Figure 3.2 is addressed, given that it is needed for the centralized controllers tuning. This system fits the one presented in Section 2.3.3.2 but with the additional reactive power injection q_{ctr}. The inputs and ouputs diagram of this system is depicted in Figure 3.4.

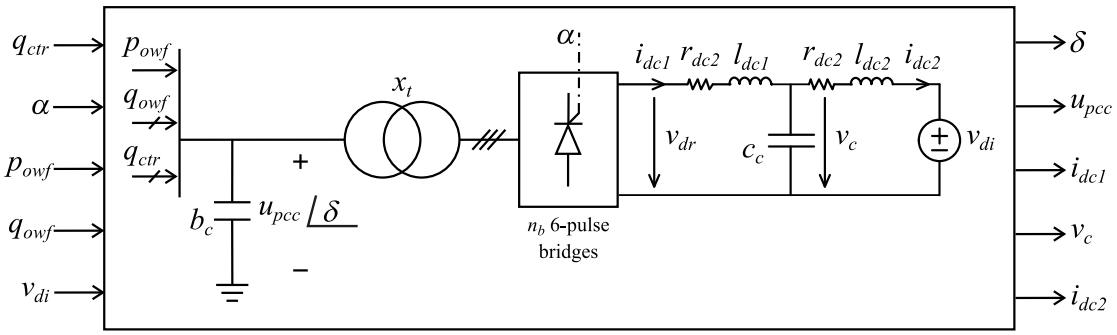

Figure 3.4: Inputs and outputs diagram of the OWF layout used for the centralized control studies including the additional input q_{ctr}.

The addition of the input q_{ctr} makes the small-signal model be the one detailed in (3.5). Its inputs, outputs and states are $\boldsymbol{\Delta u_{nc}} = [\Delta q_{ctr}, \Delta\alpha, \Delta p_{owf}, \Delta q_{owf}, \Delta v_{di}]^{\mathsf{T}}$, $\boldsymbol{\Delta y_{nc}}$=$[\Delta\delta, \Delta u_{pcc}, \Delta i_{dc1}, \Delta v_c, \Delta i_{dc2}, \Delta u_{pcc,q}]^{\mathsf{T}}$ and $\boldsymbol{\Delta x_{nc}}$=$[\Delta\delta, \Delta u_{pcc}, \Delta i_{dc1}, \Delta v_c, \Delta i_{dc2}]^{\mathsf{T}}$, respectively. Note that not only the input q_{ctr}, but also the output $\Delta u_{pcc,q}$, which will be used for the frequency control, is added with respect to the model presented in (2.52). In addition, the subscript nc denotes the small-signal model of the non-controlled LCC-rectifier-based system.

$$\frac{1}{\omega_0}\frac{d\boldsymbol{\Delta x_{nc}}}{dt} = \boldsymbol{A_{nc}}\boldsymbol{\Delta x_{nc}} + \boldsymbol{B_{nc}}\boldsymbol{\Delta u_{nc}}$$

$$\boldsymbol{\Delta y_{nc}} = \boldsymbol{C_{nc}}\boldsymbol{\Delta x_{nc}} + \boldsymbol{D_{nc}}\boldsymbol{\Delta u_{nc}} \tag{3.5}$$

where $\boldsymbol{A_{nc}}$ is equal to $\boldsymbol{A_{pr}}$ in (2.53) and $\boldsymbol{B_{nc}}$, $\boldsymbol{C_{nc}}$ and $\boldsymbol{D_{nc}}$ are as follows:

$$\boldsymbol{B_{nc}} = \begin{bmatrix} -\frac{1}{q_{c0}} & \frac{p_{owf0}}{q_{c0}}\zeta_{\alpha_0} & 0 & -\frac{1}{q_{c0}} & 0 \\ 0 & u_{pcc0}\frac{q_{r0}}{q_{c0}}\zeta_{\alpha_0} & \frac{u_{pcc0}}{q_{c0}} & 0 & 0 \\ 0 & -\frac{k_{\alpha,\mu}u_{pcc0}\sin\varphi_0}{l_{dc1}}\zeta_{\alpha_0} & 0 & 0 & 0 \\ 0 & 0 & 0 & 0 & 0 \\ 0 & 0 & 0 & 0 & -\frac{1}{l_{dc2}} \end{bmatrix}$$

$$\boldsymbol{C_{nc}} = \begin{bmatrix} 1 & 0 & 0 & 0 & 0 \\ 0 & 1 & 0 & 0 & 0 \\ 0 & 0 & 1 & 0 & 0 \\ 0 & 0 & 0 & 1 & 0 \\ 0 & 0 & 0 & 0 & 1 \\ u_{pcc0}\cos\delta_0 & \sin\delta_0 & 0 & 0 & 0 \end{bmatrix}$$

$$\boldsymbol{D_{nc}} = \begin{bmatrix} 0 & 0 & 0 & 0 & 0 \\ 0 & 0 & 0 & 0 & 0 \\ 0 & 0 & 0 & 0 & 0 \\ 0 & 0 & 0 & 0 & 0 \\ 0 & 0 & 0 & 0 & 0 \\ 0 & 0 & 0 & 0 & 0 \end{bmatrix} \tag{3.6}$$

In the following sections, the frequency PI controller will be tuned and the small-signal model of the diode-rectifier-based OWF layout will be analyzed. In this small-signal model, Δq_{ctr} will become function of $\Delta\delta$ given the frequency PI controller equation and $\Delta\alpha$ is eliminated because of the diode rectifier. Finally, the voltage and frequency controllers are designed for the thyristor-rectifier-based OWF layout. Then, the small-signal of the controlled system will be also studied. This small-signal model will lose the inputs $\Delta\alpha$ and Δq_{ctr} because they depend on the state variables Δu_{pcc} and $\Delta\delta$ given the voltage and frequency PI controller equations, respectively.

It is worth mentioning that the controlled systems are different depending on the LCC rectifier semiconductor. Therefore, the independent study of the frequency controlled diode rectifier and the voltage and frequency controlled thyristor rectifier is interesting even though the diode rectifier could be assumed to be a particular case of the thyristor rectifier.

3.4.1 Diode-rectifier-based HVDC connection with frequency control

First, the small-signal model in (3.5) has to be modified in order to fit the diode rectifier-based HVDC connection. This is achieved by eliminating the second column of matrices $\boldsymbol{B_{nc}}$ and $\boldsymbol{D_{nc}}$ and remaining the other matrices the same. Note that the firing angle input does not exist so the inputs vector becomes $\boldsymbol{\Delta u_{nc}}$= $[\Delta q_{ctr}, \Delta p_{owf}, \Delta q_{owf}, \Delta v_{di}]^{\mathsf{T}}$.

The aformentioned small-signal model is used to obtain the transfer function between the input Δq_{ctr} and the output $\Delta u_{pcc,q}$. This is due to the centralized frequency control proposed in Section 3.3.1. It consists of a PI controller which processes the error of the PCC voltage vector q component to provide the reactive power to be injected for the frequency control. The required transfer function is shown in (3.7), which is a negative integrator with time constant $\dfrac{b_c u_{pcc0}^2}{\omega_0}$.

$$\frac{\Delta u_{pcc,q}}{\Delta q_{ctr}} = \frac{-\omega_0}{b_c u_{pcc0}^2 s} \tag{3.7}$$

As it has been previously stated, the PCC voltage magnitude cannot be controlled. Thus, the transfer funtion addressed in (3.7) will be slightly different depending on the operating point considered, which will imply a different u_{pcc0} value. The proposed onshore inverter DC voltage value v_{di} is designed to be the one which yields a PCC voltage magnitude of 1 p.u. when the active power transmitted through the HVDC link is approximately 0.5 p.u. Then, the operating point defined by p_{owf0}=0.5 p.u. is the one chosen for the frequency controller design.

The specifications used to derive the PI parameters are a 1000 rad/s bandwidth in the feedback system and a PI controller time constant equal to 10 ms. The PI controller equation is the one shown in (3.9) and the parameter values which are obtained are k_p^{fc}=1.8 p.u. and k_i^{fc}=180/ω_0=0.573 p.u. This equation uses the value of $\Delta u_{pcc,q}$ which can be extracted from (3.5) and is as follows:

$$\Delta u_{pcc,q} = \sin\delta_0 \Delta u_{pcc} + u_{pcc0}\cos\delta_0 \Delta\delta = u_{pcc0}\Delta\delta \tag{3.8}$$

$$\Delta q_{ctr} = u_{pcc0}\left(k_p^{fc}\Delta\delta + k_i^{fc}\omega_0 \int \Delta\delta dt\right) = u_{pcc0}\left(k_p^{fc}\Delta\delta + k_i^{fc}\Delta x_{fc}\right) \tag{3.9}$$

As it can be observed, the new state variable Δx_{fc} is defined and its dynamic equation is as follows:

$$\frac{1}{\omega_0}\frac{d\Delta x_{fc}}{dt} = \Delta\delta \tag{3.10}$$

Then, the small-signal model which includes the frequency control can be derived. It adds the dynamic equation (3.10) to the ones considered in the model shown in (3.5)

and its matrix form is as follows:

$$\frac{1}{\omega_0}\frac{d\boldsymbol{\Delta x_{df}}}{dt} = \boldsymbol{A_{df}}\boldsymbol{\Delta x_{df}} + \boldsymbol{B_{df}}\boldsymbol{\Delta u_{df}}$$

$$\boldsymbol{\Delta y_{df}} = \boldsymbol{C_{df}}\boldsymbol{\Delta x_{df}} + \boldsymbol{D_{df}}\boldsymbol{\Delta u_{df}} \tag{3.11}$$

where $\boldsymbol{\Delta u_{df}} = [\Delta p_{owf}, \Delta q_{owf}, \Delta v_{di}]^{\mathsf{T}}$, $\boldsymbol{\Delta y_{df}}$=$[\Delta\delta, \Delta u_{pcc}, \Delta i_{dc1}, \Delta v_c, \Delta i_{dc2}, \Delta q_{ctr}]^{\mathsf{T}}$ and $\boldsymbol{\Delta x_{df}}$=$[\Delta\delta, \Delta u_{pcc}, \Delta i_{dc1}, \Delta v_c, \Delta i_{dc2}, \Delta x_{fc}]^{\mathsf{T}}$. Note that the subscript df denotes the small-signal model of the diode-rectifier-based system with frequency control. $\boldsymbol{A_{df}}$, $\boldsymbol{B_{df}}$, $\boldsymbol{C_{df}}$ and $\boldsymbol{D_{df}}$ can be derived from matrices in (3.5) as follows:

$$\boldsymbol{A_{df}} = \begin{bmatrix} b_{nc,11}u_{pcc0}k_p^{fc} & a_{nc,12} & a_{nc,13} & 0 & 0 & b_{nc,11}u_{pcc0}k_i^{fc} \\ 0 & a_{nc,22} & a_{nc,23} & 0 & 0 & 0 \\ 0 & a_{nc,32} & a_{nc,33} & a_{nc,34} & 0 & 0 \\ 0 & 0 & a_{nc,43} & 0 & a_{nc,45} & 0 \\ 0 & 0 & 0 & a_{nc,54} & a_{nc,55} & 0 \\ 1 & 0 & 0 & 0 & 0 & 0 \end{bmatrix}$$

$$\boldsymbol{B_{df}} = \begin{bmatrix} 0 & b_{nc,14} & 0 \\ b_{nc,23} & 0 & 0 \\ 0 & 0 & 0 \\ 0 & 0 & 0 \\ 0 & 0 & b_{nc,55} \\ 0 & 0 & 0 \end{bmatrix}$$

$$\boldsymbol{C_{df}} = \begin{bmatrix} 1 & 0 & 0 & 0 & 0 & 0 \\ 0 & 1 & 0 & 0 & 0 & 0 \\ 0 & 0 & 1 & 0 & 0 & 0 \\ 0 & 0 & 0 & 1 & 0 & 0 \\ 0 & 0 & 0 & 0 & 1 & 0 \\ u_{pcc0}k_p^{fc} & 0 & 0 & 0 & 0 & u_{pcc0}k_i^{fc} \end{bmatrix}$$

$$\boldsymbol{D_{df}} = \begin{bmatrix} 0 & 0 & 0 \\ 0 & 0 & 0 \\ 0 & 0 & 0 \\ 0 & 0 & 0 \\ 0 & 0 & 0 \\ 0 & 0 & 0 \end{bmatrix} \tag{3.12}$$

As it has been previously established, the stability of the frequency controlled diode-rectifier-based HVDC-connected OWF must be checked in the operating points which are different from the one which has been used for the controller tuning. Specifically, the stability is checked in a hundred operating points which correspond to active power transferred from 0.01 p.u. to 1 p.u. (p_{owf0}=0.01, 0.02, 0.03, ..., 1 p.u.). The eigenvalues of the resulting small-signal model have been extracted for each of the operating points and they are depicted in Figure 3.5.

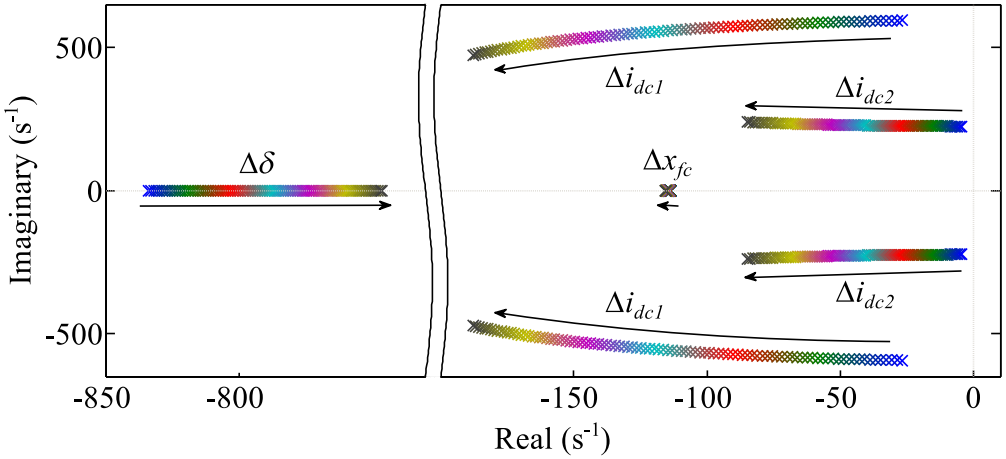

Figure 3.5: Eigenvalues of the OWF layout with diode-rectifier-based HVDC connection and centralized frequency control at diverse operating points (arrows indicate increasing active power transferred).

As it can be observed in Figure 3.5, the real part of all the eigenvalues is negative so the stability is then proved. Moreover, the arrows which can be found in Figure 3.5 show the locus of the studied eigenvalues while active power p_{owf} is increased. The dominant state is also indicated for each of the eigenvalues. It is worth noting that the four complex eigenvalues which can be analyzed increase their stability when the active power transferred is increased, given the higher damping acquired. Finally, it should be pointed out that the dominant states of these complex eigenvalues are Δi_{dc1} and Δi_{dc2}, which also increase their steady-state values in the same varying conditions.

3.4.2 Thyristor-rectifier-based HVDC connection with voltage and frequency control

Since in this section the plant transfer function to be studied for the frequency control design is equal to the one of the diode-rectifier-based system, the frequency controller matches the one derived in Section 3.4.1. It should be pointed out that the plant is invariable with respect to the operating point due to the additional voltage control which is applied in the thyristor-rectifier-based HVDC-connected OWF.

Following the same methodology which has been used in order to tune the frequency controller, the small-signal model of the thyristor-rectifier-based layout with frequency control is needed in order to get the plant transfer function to be used by the

voltage controller. This small-signal model is the one shown in (3.13). Note that the subscript tf denotes the small-signal model of the thyristor-rectifier-based system with frequency control.

$$\frac{1}{\omega_0}\frac{d\boldsymbol{\Delta x_{tf}}}{dt} = \boldsymbol{A_{tf}}\boldsymbol{\Delta x_{tf}} + \boldsymbol{B_{tf}}\boldsymbol{\Delta u_{tf}}$$

$$\boldsymbol{\Delta y_{tf}} = \boldsymbol{C_{tf}}\boldsymbol{\Delta x_{tf}} + \boldsymbol{D_{tf}}\boldsymbol{\Delta u_{tf}} \tag{3.13}$$

where $\boldsymbol{A_{tf}}$, $\boldsymbol{C_{tf}}$, $\boldsymbol{\Delta x_{tf}}$ and $\boldsymbol{\Delta y_{tf}}$ are equal to $\boldsymbol{A_{df}}$, $\boldsymbol{C_{df}}$, $\boldsymbol{\Delta x_{df}}$ and $\boldsymbol{\Delta y_{df}}$, respectively, in (3.12). $\boldsymbol{\Delta u_{tf}} = [\Delta\alpha, \Delta p_{owf}, \Delta q_{owf}, \Delta v_{di}]^{\mathsf{T}}$ and $\boldsymbol{B_{tf}}$ and $\boldsymbol{D_{tf}}$ can be derived from matrices in (3.5) as follows:

$$\boldsymbol{B_{tf}} = \begin{bmatrix} b_{nc,12} & 0 & b_{nc,14} & 0 \\ b_{nc,22} & b_{nc,23} & 0 & 0 \\ b_{nc,32} & 0 & 0 & 0 \\ 0 & 0 & 0 & 0 \\ 0 & 0 & 0 & b_{nc,55} \\ 0 & 0 & 0 & 0 \\ 0 & 0 & 0 & 0 \end{bmatrix}$$

$$\boldsymbol{D_{tf}} = \begin{bmatrix} 0 & 0 & 0 & 0 \\ 0 & 0 & 0 & 0 \\ 0 & 0 & 0 & 0 \\ 0 & 0 & 0 & 0 \\ 0 & 0 & 0 & 0 \\ 0 & 0 & 0 & 0 \end{bmatrix} \tag{3.14}$$

The plant transfer function to be obtained from (3.13) is the one which has $\Delta\alpha$ as input and Δu_{pcc} as output, which changes depending on the active power operating point. This is due to the centralized voltage controller proposed in Section 3.3.2, where the PI controller processes the negative error of the PCC voltage vector d component to produce the thyristor firing angle to be used. It is worth noting the correspondence between the voltage vector magnitude and the d component due to the centralized frequency control strategy ($\Delta u_{pcc,d}{=}\Delta u_{pcc}\cos\delta_0 - u_{pcc0}\sin\delta_0\Delta\delta{=}\Delta u_{pcc}$).

As it was previously chosen, p_{owf0}=0.5 p.u. is also used for the centralized voltage controller design. The design specifications for this controller are 500 rad/s bandwidth in the feedback system and a PI time constant which is three times higher than the frequency controller one (30 ms). The equation that defines this PI voltage controller is shown in (3.15) and its parameter values are k_p^{vc}=1.67 rad/p.u. and k_i^{vc}=0.177 rad/p.u.

$$\Delta\alpha = -\left(k_p^{vc}\Delta u_{pcc} + k_i^{vc}\omega_0\int \Delta u_{pcc}dt\right) = -(k_p^{vc}\Delta u_{pcc} + k_i^{vc}\Delta x_{vc}) \tag{3.15}$$

As it can be observed in (3.15), a new state variable Δx_{vc} is defined and its dynamic equation is as follows:

$$\frac{1}{\omega_0}\frac{d\Delta x_{vc}}{dt} = \Delta u_{pcc} \tag{3.16}$$

If (3.15) and (3.16) are considered together with (3.13), the small-signal model of the thyristor-rectifier-based HVDC-connected OWF under study can be obtained in order to check the stability of the controlled system in the diverse operating points. This small-signal model is presented in (3.17). Note that the subscript tvf denotes the small-signal model of the thyristor-rectifier-based system with voltage and frequency control.

$$\begin{aligned}\frac{1}{\omega_0}\frac{d\boldsymbol{\Delta x_{tvf}}}{dt} &= \boldsymbol{A_{tvf}\Delta x_{tvf}} + \boldsymbol{B_{tvf}\Delta u_{tvf}} \\ \boldsymbol{\Delta y_{tvf}} &= \boldsymbol{C_{tvf}\Delta x_{tvf}} + \boldsymbol{D_{tvf}\Delta u_{tvf}}\end{aligned} \tag{3.17}$$

where $\boldsymbol{\Delta u_{tvf}}$=$[\Delta p_{owf}, \Delta q_{owf}, \Delta v_{di}]^{\mathsf{T}}$, $\boldsymbol{\Delta y_{tvf}}$=$[\Delta\delta, \Delta u_{pcc}, \Delta i_{dc1}, \Delta v_c, \Delta i_{dc2}, \Delta q_{ctr}, \Delta\alpha]^{\mathsf{T}}$ and $\boldsymbol{\Delta x_{tvf}}$=$[\Delta\delta, \Delta u_{pcc}, \Delta i_{dc1}, \Delta v_c, \Delta i_{dc2}, \Delta x_{fc}, \Delta x_{vc}]^{\mathsf{T}}$. $\boldsymbol{A_{tvf}}$, $\boldsymbol{B_{tvf}}$, $\boldsymbol{C_{tvf}}$ and $\boldsymbol{D_{tvf}}$ can be derived from matrices in (3.5) as follows:

$$\boldsymbol{A_{tvf}} = \begin{bmatrix} b_{nc,11}u_{pcc0}k_p^{fc} & a_{nc,12}-b_{nc,12}k_p^{vc} & a_{nc,13} & 0 & 0 & b_{nc,11}u_{pcc0}k_i^{fc} & -b_{nc,12}k_i^{vc} \\ 0 & a_{nc,22}-b_{nc,22}k_p^{vc} & a_{nc,23} & 0 & 0 & 0 & -b_{nc,22}k_i^{vc} \\ 0 & a_{nc,32}-b_{nc,32}k_p^{vc} & a_{nc,33} & a_{nc,34} & 0 & 0 & -b_{nc,32}k_i^{vc} \\ 0 & 0 & a_{nc,43} & 0 & a_{nc,45} & 0 & 0 \\ 0 & 0 & 0 & a_{nc,54} & a_{nc,55} & 0 & 0 \\ 1 & 0 & 0 & 0 & 0 & 0 & 0 \\ 0 & 1 & 0 & 0 & 0 & 0 & 0 \end{bmatrix}$$

$$\boldsymbol{B_{tvf}} = \begin{bmatrix} 0 & b_{nc,14} & 0 \\ b_{nc,23} & 0 & 0 \\ 0 & 0 & 0 \\ 0 & 0 & 0 \\ 0 & 0 & b_{nc,55} \\ 0 & 0 & 0 \\ 0 & 0 & 0 \end{bmatrix}$$

$$\boldsymbol{C_{tvf}} = \begin{bmatrix} 1 & 0 & 0 & 0 & 0 & 0 & 0 \\ 0 & 1 & 0 & 0 & 0 & 0 & 0 \\ 0 & 0 & 1 & 0 & 0 & 0 & 0 \\ 0 & 0 & 0 & 1 & 0 & 0 & 0 \\ 0 & 0 & 0 & 0 & 1 & 0 & 0 \\ u_{pcc0}k_p^{fc} & 0 & 0 & 0 & 0 & u_{pcc0}k_i^{fc} & 0 \\ 0 & -k_p^{vc} & 0 & 0 & 0 & 0 & -k_i^{vc} \end{bmatrix}$$

$$\boldsymbol{D_{tvf}} = \begin{bmatrix} 0 & 0 & 0 \\ 0 & 0 & 0 \\ 0 & 0 & 0 \\ 0 & 0 & 0 \\ 0 & 0 & 0 \\ 0 & 0 & 0 \\ 0 & 0 & 0 \end{bmatrix} \tag{3.18}$$

As it has been previously performed with the frequency control, the centralized voltage and frequency controlled system must be evaluated in the diverse operating points in order to assess the stability analysis. The same operating points considered in Section 3.4.1 are considered here and the eigenvalues extracted from each of the small-signal models are depicted in Figure 3.6. Figure 3.6 has arrows which indicate the direction of the eigenvalues movement when the active power transferred is increased. The dominant states for each of the eigenvalues are also defined in Figure 3.6.

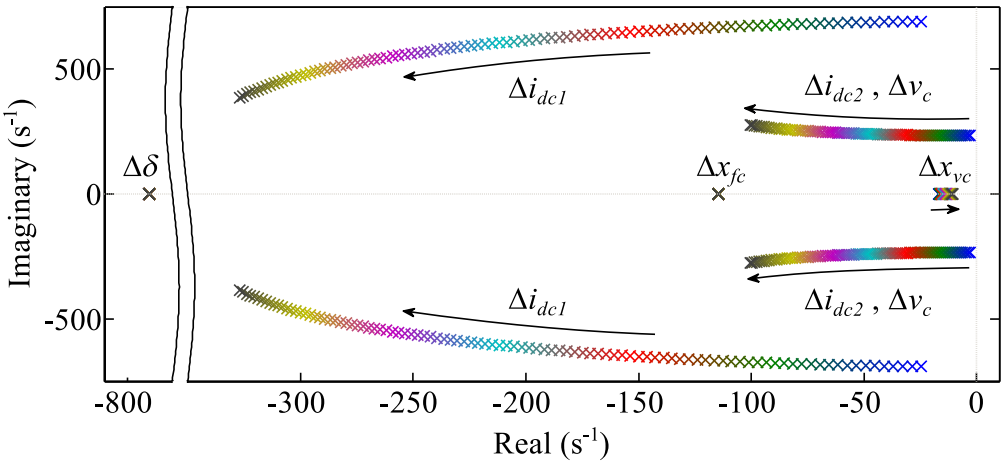

Figure 3.6: Eigenvalues of the OWF layout with thyristor-rectifier-based HVDC connection and centralized voltage and frequency control at diverse operating points (arrows indicate increasing active power transferred).

As it can be extracted from Figure 3.6, the centralized voltage and frequency controlled system is stable due to the negative real part of all the eigenvalues. There are two eigenvalues which are invariable with respect to the operating point and their

dominant states are $\Delta\delta$ and Δx_{fc}. Furthermore, it can be stated that the stability improves when the active power transferred is increased due to the higher damping of the complex eigenvalues. However, the eigenvalue whose dominant state is Δx_{vc} slightly moves towards the imaginary axis when p_{owf} is increased.

The comparison of the eigenvalues of the diode-rectifier case and the thyristor rectifier case (Figure 3.5 and Figure 3.6, respectively) shows that the two real eigenvalues which vary with the operating conditions in the diode-rectifier case do not move when the voltage control is applied in the thyristor-rectifier case. In addition, the complex eigenvalues of the thyristor-rectifier case take positions which are located farther from the imaginary axis than in the diode-rectifier case. Finally, Δv_c becomes a dominant state of one of the complex eigenvalues in the thyristor rectifier case.

3.5 AVM simulation results

Once the centralized controllers have already been tuned, this section will show the simulation results of the AVM of the layout in Figure 3.2 with the proposed centralized control embedded. These simulations are performed in Matlab/Simulink.

Three initial operating points at 0.1 p.u., 0.4 p.u. and 0.7 p.u. of OWF power (p_{owf}) are simulated during 0.4 s. The initial reactive power injected by the OWF (q_{owf}) is considered zero in the three cases. Then, two input steps are considered during the simulation time window: a p_{owf} increment of 0.2 p.u. at t=0.01 s and a q_{owf} increment from zero to 0.1 p.u. a t=0.3 s. It should be pointed out that both step changes are smoothed by the action of a first order filter whose time constant and gain are equal to 10 ms and 1 p.u., respectively. This permits representing more realistic changing conditions.

It is worth noting that there is a third input in both diode-rectifier-based and thyristor-rectifier-based systems which corresponds to the onshore inverter DC voltage v_{di}. Even though the system response to a change in v_{di} could be checked, it is not of interest given the constant DC voltage operating mode of the onshore inverter which will maintain this voltage value.

The results for each of the LCC rectifiers considered are presented in the following subsections.

3.5.1 Diode-rectifier-based HVDC connection with frequency control

The simulation results of the diode-rectifier-based HVDC-connected OWF with frequency control are depicted in Figure 3.7. The three different study cases regarding the initial operating conditions are shown. From top to bottom, Figure 3.7 shows the PCC bus frequency, the PCC bus voltage magnitude and the reactive power injected to control the offshore AC frequency.

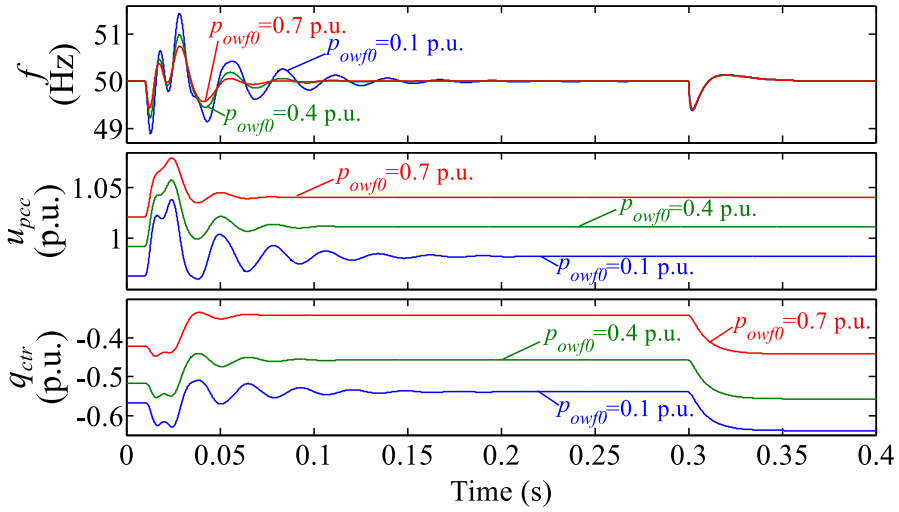

Figure 3.7: AVM simulation results during active- and reactive- power changes of the diode-rectifier-based HVDC connection of the OWF with centralized frequency control (frequency, PCC voltage and controlling reactive power).

As it can be observed in Figure 3.7, the PCC bus voltage magnitude increases with the active power generated from the OWF, *i.e.* with the active power transferred by the HVDC link. The reactive power absorbed by the diode rectifier and its transformer also increases in these varying conditions. Thus, the controlling reactive power q_{ctr} is also higher when the active power level is higher.

Figure 3.7 shows that the variation of u_{pcc} and q_{ctr} when active power is increased at t=0.01 s follows the same logics. When the reactive power provided by the OWF is increased at t=0.3 s, the PCC voltage magnitude remains unvariable. However, the controlling reactive power is decreased in order to maintain the frequency at its reference value (50 Hz), what is perfectly achieved in the diverse simulation cases.

By comparing the reponse in the three different initial operating conditions, it can be concluded that the lower the active power level in the system, the more oscillating is the system response to the active power change. This result can be predicted by the stability analysis in Section 3.4.1 (Figure 3.5), where the complex eigenvalues increase their damping when the active power level is increased.

It is worth mentioning that despite the absence of voltage control in this diode-rectifier-based HVDC-connected OWF, voltage varies within acceptable bounded limits. Actually, u_{pcc} steady-state limits can be calculated and they are 1.05 p.u. and 0.954 p.u. when p_{owf} is equal to 1 p.u. and 0.01 p.u., respectively. These variations are acceptable according to grid codes [6].

3.5.2 Thyristor-rectifier-based HVDC connection with voltage and frequency control

The simulation results of the thyristor-rectifier-based HVDC-connected OWF with voltage and frequency control are depicted in Figure 3.8, where the three different study cases are shown. From top to bottom, Figure 3.8 shows the PCC bus frequency, the PCC bus voltage magnitude, the reactive power injected to control the offshore AC frequency and the thyristor firing angle.

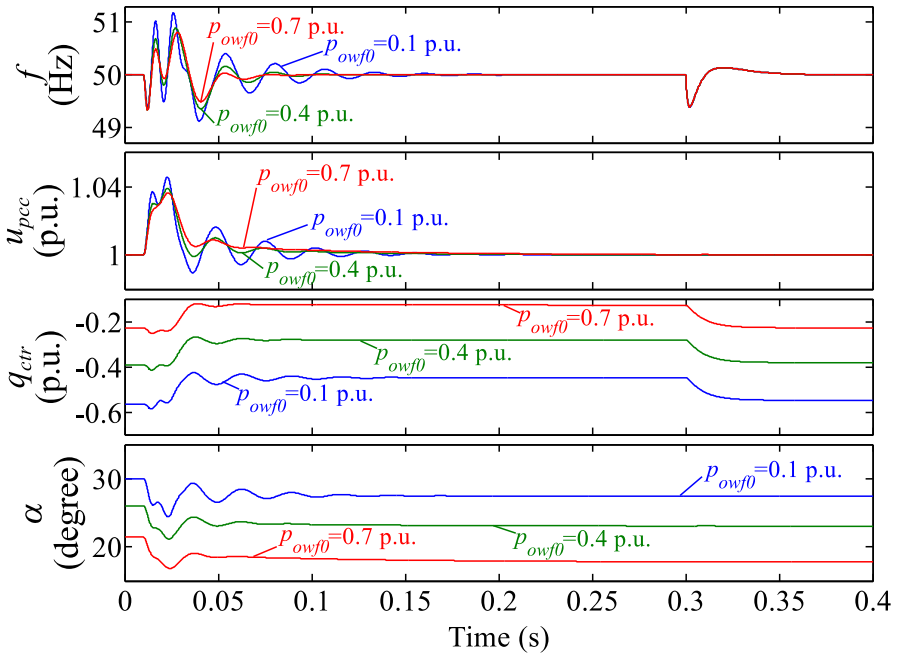

Figure 3.8: AVM simulation results during active- and reactive- power changes of the thyristor-rectifier-based HVDC connection of the OWF with centralized voltage and frequency control (frequency, PCC voltage, controlling reactive power and firing angle).

As it can be observed in Figure 3.8, both AC voltage and frequency are maintained at their corresponding reference values 1 p.u. and 50 Hz. By analyzing both the steady-state conditions and the active-power change response, it can be concluded that the higher the active power level of the system the lower the firing angle set by the centralized voltage controller and the higher the reactive power to be injected for the frequency control.

The reactive power increment of q_{owf} at t=0.3 s mainly affects the frequency, given that the transient of the PCC bus voltage magnitude is negligible. It is worth mentioning that the voltage control provides certain coupling between these variables because in the diode-rectifier case u_{pcc} remained invariable in the reactive power change.

The stability analysis presented in Section 3.4.2 (Figure 3.6) showed that the system is more damped when the active power is increased. The results in Figure 3.8, where the response oscillates more for lower active power levels, are therefore consistent with the aforementioned analysis.

It should be pointed out that the reactive power to be injected for the frequency control takes high values in both study cases. As it was established when the system parameters were presented, the model is based on the HVDC Benchmark model [1] which uses a large passive capacity (reactive power compensation and harmonic filters). However, this passive AC capacity can be reduced [7], so q_{ctr} will take lower values.

3.6 Proposed control and AVM validation

The centralized voltage and frequency control proposed in this chapter has been derived, designed and analyzed by means of the proposed AVM of the OWF layout presented in Figure 3.2. Therefore, it is required to validate both the proposed control and the model by using a DSM simulation which has been performed using PSIM. As it is widely extended in modeling, both the small-signal frequency-domain and the large-signal time-domain responses of the diode-rectifier-based and thyristor-rectifier-based controlled systems are compared in the following subsections.

3.6.1 Small-signal frequency-domain validation

On the one hand, the small-signal models obtained in Section 3.4 are used in order to obtain the transfer function which will be studied by means of a FRA. This transfer function is the one with the rectifier DC current as output and the OWF active power as input. This transfer function is chosen because the incoming active power is the main perturbation of this system, which will depend on the wind, while the rectifier DC current indicates the power transferred to the onshore grid. Moreover, p_{owf0}=0.4 p.u. is the steady-state operating point chosen for the analysis.

The AC sweep tool of PSIM has been used in order to obtain the FRA of the DSM while the small-signal model transfer function of the AVM naturally allows the FRA extraction. The resulting Bode diagrams are presented in Figure 3.9a and Figure 3.9b for the diode-rectifier-based and the thyristor-rectifier-based HVDC connected OWFs, respectively.

As it has been stated in the non-controlled AVM validation in Section 2.3.3, the AVM also shows a reasonable accuracy with respect to the DSM when the centralized controlled systems are analyzed. However, when the frequency approaches the rectifier switching frequency (600 Hz for the twelve-pulse rectifier), this accuracy is lost because the AVM assumptions are not solid when the frequency approaches or exceeds the converter switching frequency [8]. Both responses lead to these conclusions.

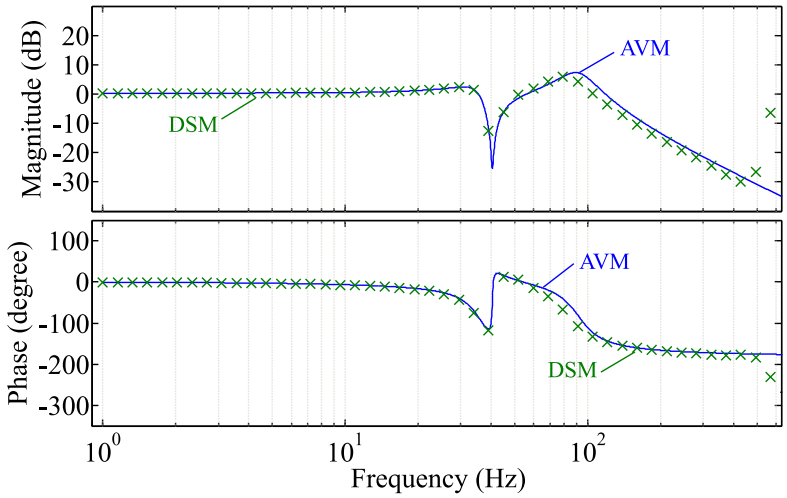

(a) Diode-rectifier-based HVDC connection of the OWF with centralized frequency control.

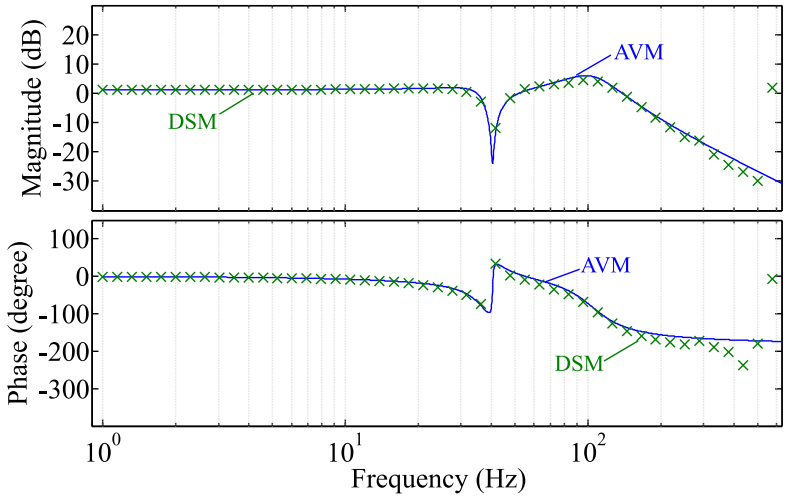

(b) Thyristor-rectifier-based HVDC connection of the OWF with centralized voltage and frequency control.

Figure 3.9: Frequency response of the transfer function between the rectifier DC current and the OWF active power with the proposed AVM and the DSM representation.

3.6.2 Large-signal time-domain validation

This section allows the comparison of the large-signal time-domain simulation of both the AVM and the DSM responses to the power changes scheduled in the AVM simulations in Section 3.5 (p_{owf} and q_{owf} increments of 0.2 p.u. and 0.1 p.u. at t=0.01 s and t=0.3 s, respectively). The AVM simulations are performed in Matlab/Simulink while the DSM ones are performed in PSIM. For the sake of clarity, just the simulations with the initial operating point set at p_{owf0}=0.4 p.u. are compared. The results for both the AVM and the DSM are presented in Figure 3.10a for the diode-rectifier-based HVDC-connected OWF and in Figure 3.10b for the thyristor-rectifier-based HVDC-connected OWF.

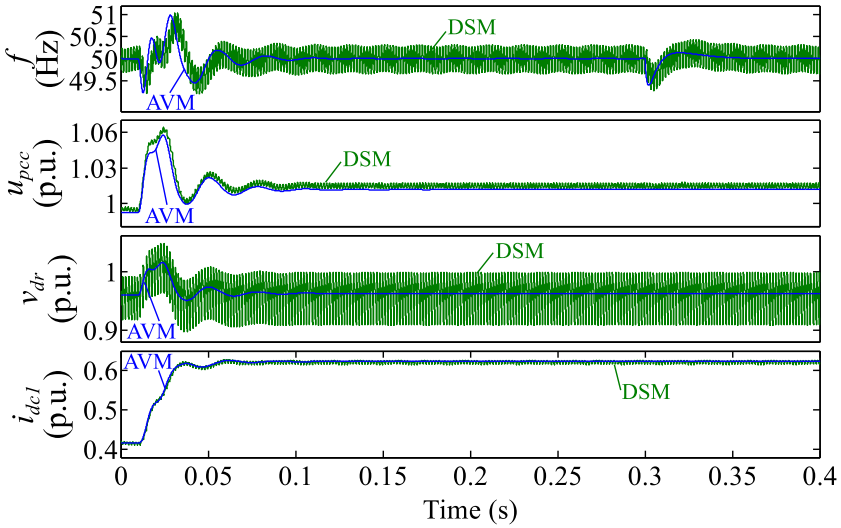

(a) Diode-rectifier-based HVDC connection of the OWF with centralized frequency control (PCC bus frequency and voltage magnitude, and rectifier DC voltage and current from top to bottom).

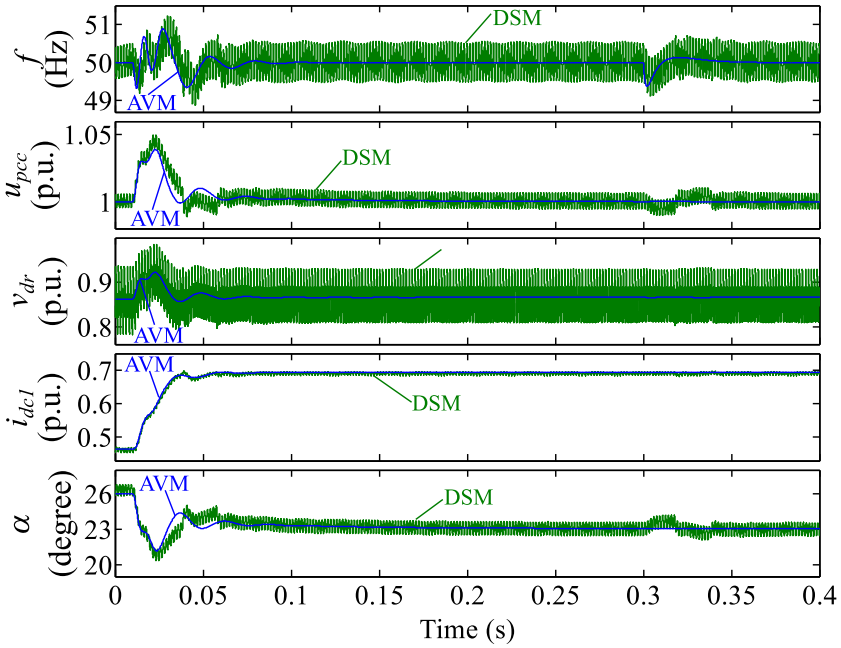

(b) Thyristor-rectifier-based HVDC connection of the OWF with centralized voltage and frequency control (PCC bus frequency and voltage magnitude, rectifier DC voltage and current, and thyristor firing angle from top to bottom).

Figure 3.10: Comparison of the simulation results during active- and reactive- power changes with the proposed AVM and the DSM representation.

Figure 3.10a shows the PCC bus frequency and voltage magnitude, and the rectifier DC voltage and current from top to bottom. As in the previous studies, Figure 3.10b shows the thyristor firing angle in addition to the aforementioned variables. Figure 3.10 shows a reasonable accuracy of the AVM dynamic response compared to the DSM one. It also demonstrates a proper performance of the centralized voltage and frequency

control when it is applied to DSMs, what validates the proposal. Finally, it is worth noting that the decoupling between the reactive power change at t=0.3 s and the PCC voltage magnitude response which could be concluded from the AVM is also validated by the detailed switching simulation. In Figure 3.7 (diode rectifier), the decoupling was concluded while in Figure 3.8 (thyristor rectifier) it was addressed that there was a negligible coupling which is not as negligible in the DSM simulation in Figure 3.10b.

3.7 Fault response analysis

This section carries out the fault response analysis of the DSM of both the diode-rectifier-based HVDC-connected OWF with frequency control and the thyristor-rectifier-based HVDC-connected OWF with voltage and frequency control. The DSM simulations are performed in PSIM. A 100 ms-fault at the PCC bus is scheduled at t=0.4 s when the active power level of the system is 0.6 p.u. The following subsections present the obtained results.

3.7.1 Diode-rectifier-based HVDC connection with frequency control

The fault analysis results of the diode-rectifier-based HVDC-connected OWF with frequency control are presented in Figure 3.11. PCC frequency, PCC voltage magnitude and rectifier DC voltage and current are shown from top to bottom in Figure 3.11. During the fault, the PCC voltage drops to zero. Thus, the diode rectifier is blocked and the HVDC link voltage oscillates at its natural frequency. After the fault is cleared, the OWF voltage is recovered and frequency is driven to the reference value by the centralized frequency control. Naturally, the fault response widely depends on the FRT response of WTGSs. Specifically, p_{owf} is driven to zero during the fault and ramped up after the fault clearance. The effects of this ramped response can be observed in the rectifier DC current trend after the fault clearance. Finally, it is worth mentioning that the frequency is not a explicit signal of the DSM. Therefore, a PLL is used just for measuring purposes.

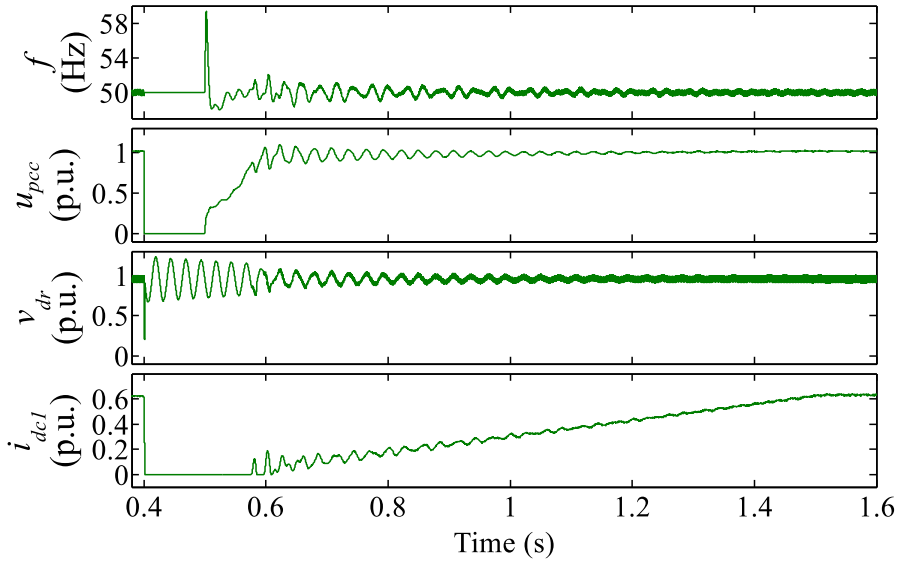

Figure 3.11: Response of the diode-rectifier-based HVDC connection of the OWF to a 100 ms fault at the PCC bus with centralized frequency control (frequency, PCC voltage and rectifier DC voltage and current).

3.7.2 Thyristor-rectifier-based HVDC connection with voltage and frequency control

The fault analysis results of the thyristor-rectifier-based HVDC-connected OWF with voltage and frequency control are presented in Figure 3.12. This Figure shows the PCC frequency and voltage magnitude, the rectifier DC voltage and current, and the thyristor firing angle from top to bottom. The conclusions addressed in Section 3.7.1 can be applied to these results, except for the additional voltage control performed in this case. During the fault, it can be observed in Figure 3.12 that the centralized voltage controller increases the firing angle trying to recover the PCC voltage magnitude. However, the fault does not allow this recovery and the controller reaches saturation (α=45°). After the fault clearance, both the voltage and frequency controls are recovered and the firing angle reaches its pre-fault value.

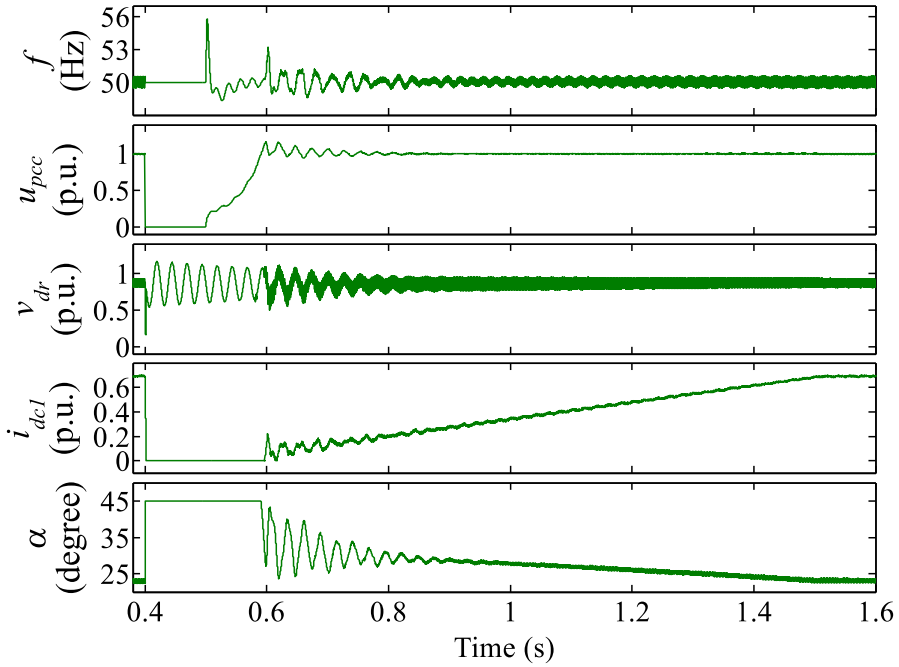

Figure 3.12: Response of the thyristor-rectifier-based HVDC connection of the OWF to a 100 ms fault at the PCC bus with centralized voltage and frequency control (frequency, PCC voltage, rectifier DC voltage and current and firing angle).

3.8 Conclusions

This chapter has presented a centralized voltage and frequency control which allows the operation of an OWF connected to an LCC-rectifier-based HVDC link. Both the diode rectifier and the thyristor rectifier are considered.

The proposed control is based on the rectifier AVM proposed in Chapter 2. It is demonstrated that the reactive power balance at the capacitor bank placed at the PCC controls the frequency while the active power balance controls the PCC voltage magnitude. It is also proved that although the voltage control cannot be performed with a diode-rectifier-based HVDC link, the PCC voltage magnitude will be bounded within acceptable limits.

Given that the proposed control derivation, the controllers design and the simulations have been carried out by using the proposed AVM, the controlled systems have been validated by their response comparison to a DSM built in PSIM. Both the small-signal frequency-domain and the large-signal time-domain validations are performed. Moreover, fault studies have been presented and they demonstrate the ability of the centralized control to recover the frequency and voltage magnitude after the fault clearance.

Furthermore, a fixed reference frequency is used in this centralized proposal, avoiding the disadvantages of PLLs. It is internally defined in the control, so any value

could be used. This suggests the possibility of studying frequencies which are differnt from the standard ones or even using a variable frequency. Diverse objectives could be defined in order to optimize the frequency of the OWF AC grid. For example, it is concluded in [9] that a power increase can be achieved by applying the appropriate variable frequency in the OWF.

3.9 Bibliography

[1] M Szechtman, T Wess, and C. Thio. "A benchmark model for HVDC system studies". In: *AC and DC Power Transmission, 1991., International Conference on*. IET. 1991, pp. 374–378 (cit. on pp. 51, 66).

[2] T. Ostrem et al. "Grid connected photovoltaic (PV) inverter with robust phase-locked loop (PLL)". In: *Transmission & Distribution Conference and Exposition: Latin America, 2006. TDC'06. IEEE/PES*. IEEE. 2006, pp. 1–7 (cit. on p. 52).

[3] S. L. Sanjuan. *Voltage oriented control of three-phase boost PWM converters: design, simulation and implementation of a 3-phase boost battery charger*. Chalmers University of Technology, 2010 (cit. on p. 52).

[4] J. L. Rodriguez-Amenedo, S. Arnalte, and J. C. Burgos. "Automatic generation control of a wind farm with variable speed wind turbines". In: *Energy Conversion, IEEE Transactions on* 17.2 (2002), pp. 279–284 (cit. on p. 54).

[5] F. Díaz-González et al. "Participation of wind power plants in system frequency control: Review of grid code requirements and control methods". In: *Renewable and Sustainable Energy Reviews* 34 (2014), pp. 551–564 (cit. on p. 54).

[6] E.-E. ENTSO-E. *Network Code for Requirements for Grid Connection Applicable to all Generators*. 2013. URL: https://www.entsoe.eu/fileadmin/user_upload/_library/resources/RfG/130308_Final_Version_NC_RfG.pdf (visited on 05/23/2018) (cit. on p. 64).

[7] R. Blasco-Gimenez et al. "LCC-HVDC connection of offshore wind farms with reduced filter banks". In: *IEEE Transactions on Industrial Electronics* 60.6 (2013), pp. 2372–2380 (cit. on p. 66).

[8] J. Jatskevich, S. D. Pekarek, and A. Davoudi. "Parametric average-value model of synchronous machine-rectifier systems". In: *IEEE transactions on energy conversion* 21.1 (2006), pp. 9–18 (cit. on p. 66).

[9] O. Gomis-Bellmunt et al. "Maximum generation power evaluation of variable frequency offshore wind farms when connected to a single power converter". In: *Applied Energy* 87.10 (2010), pp. 3103–3109 (cit. on p. 72).

Chapter 4

Decentralized frequency control of OWFs connected to Diode Rectifiers

4.1 Introduction

This chapter presents the proposed decentralized frequency control for OWFs which are connected to the onshore grid by a diode-rectifier-based HVDC link. As it was stated in Chapter 1, there is an increasing interest in providing the solution which uses the diode instead of the thyristor LCC-rectifier technology in the HVDC-link connection. This is due to the fact that the diode rectifier is the most reliable rectifier solution. It lacks of auxiliary equipment which will require power supply and it has a reduced number of electric components [1, 2]. Therefore, it is ideal for rough offshore environments and requires very low maintenance. Compared to thyristors, diodes do not need

protection for firing, monitoring electronics and they are not exposed to failure events during the recovery time [1, 2]. Moreover, DRUs proposed by Siemens [1, 2] combine the diode rectifier, the transformer and the DC smoothing reactor inside the oil tank, what substantially reduces this equipment volume.

The proposed decentralized control achieves the synchronization of the WTGSs without the need of communications while the reactive power provided by the WTGSs is equally shared. The capacitor of the WTGS output filter is used for the inner control at each of the WTGSs. First, an advantage of this decentralized control proposal is that active power is not used for the frequency control. Therefore, the active-power control channel of the WTGS can use the classical control which seeks to yield maximum energy. The inner or low-level control strategy consists of orientating the output-filter-capacitor voltage vector of the WTGS to its individual reference axis. Then, all these individual reference axes are synchronized by affecting them through a Q/f droop which is performed at each WTGS. This droop not only guarantees the synchronization which is required for the frequency control but also equalizes the reactive power level of all the WTGSs of the OWF. This strategy (QSS) is quite important because the reactive power demand of both the OWF AC grid and the diode rectifier might be really high and the only way to satisfy it is to share it among the WTGSs. Otherwise, the WTGSs could easily exceed their capability limits.

This decentralized control strategy has a variable steady-state frequency. These variations are bounded between acceptable limits. It is worth mentioning that both the reactive power demand and the acceptable frequency deviations are considered in order to define the droop gain. Even though the frequency deviation is acceptable, a secondary frequency control is also proposed because constant frequency can be achieved while keeping the QSS.

First, the control fundamentals of the decentralized frequency control are presented in Section 4.2. Here, OWF equivalent layouts with a single-aggregated WTGS and two-aggregated WTGSs are used. Then, the proposed decentralized frequency control and its additional secondary frequency control are presented in Section 4.3. Section 4.4 shows the stability analysis of the proposed control. Finally, simulation results which include startup, operation and fault response are shown in Section 4.5. Here, and OWF layout with six-aggregated WTGSs is used.

4.2 Control fundamentals

There are two control fundamentals on which the decentralized control is based: the direct frequency control (DFC) and the QSS. Two different OWF layouts with a single-aggregated and two-aggregated WTGSs are used in the following subsections in order to present both control fundamentals.

4.2.1 Direct frequency control

The DFC strategy is based on the centralized frequency control proposed in Section 3.3.1. Even though this strategy has been presented at an OWF level, it will be used in this decentralized frequency control at a WTGS level.

For further demonstration of this DFC strategy, the equivalent OWF layout shown in Figure 4.1 is used. For the sake of clarity, it considers a single-aggregated WTGS. This OWF layout is only analyzed, but not simulated in this Thesis. In Figure 4.1, the WTGS (450 MW rated power) is modeled by its power outputs, the rectifier and transformer are modeled by the AVM proposed in Section 2.3.2 and the HVDC cable is represented by its resistance r_{dc} as presented in Section 2.2.

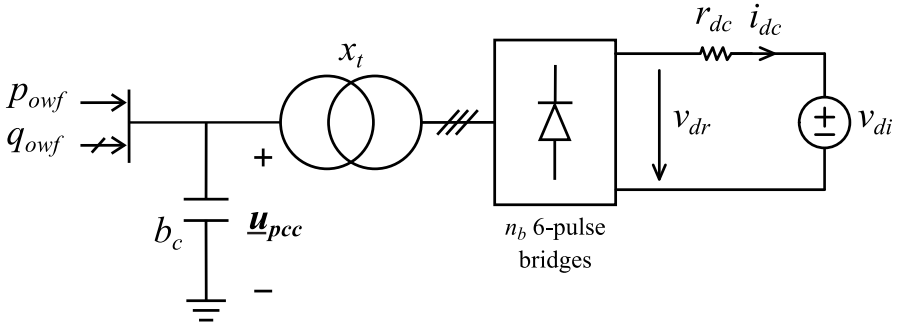

Figure 4.1: OWF equivalent with a single aggregated WTGS and an HVDC composed of a resistive cable, the inverter and a diode rectifier.

As it was stated in Section 3.3.1, the reactive power balance at the capacitor bank represented by its susceptance b_c allows the frequency control of the capacitor bank voltage vector with respect to the dq synchronous reference frame. Moreover, the voltage magnitude dynamics depends on the active power balance at the capacitor bank and it does not need to be controlled. However, it has a bounded variation.

There are two main differences between the use of this control concept here and in the centralized frequency control. First, this DFC is applied at a WTGS level in the decentralized control, so the incoming reactive power from the WTGS (q_{owf} in Figure 4.1) can be used for the frequency control. This implies that the additional reactive power injection used in Section 3.3.1 is not needed. Therefore, the direct frequency controller is the one shown in Figure 4.2. Second, even though it has been stated that the centralized frequency control is able to maintain a variable reference frequency, it has not been tested. However, in the decentralized frequency control, each of the WTGSs will follow a variable reference frequency which will allow the synchronization of all the WTGSs injections in the OWF grid.

The two dynamic equations used for the aforementioned control concept are the two first equations in (2.46): $\frac{b_c u_{pcc}}{\omega_0}\frac{du_{pcc}}{dt}=p_{owf}-p_r$ and $\frac{b_c u_{pcc}^2}{\omega_0}\frac{d\delta}{dt}=-q_{owf}+q_r-q_c$. The DFC is further analyzed by performing a small-signal study around a steady-state

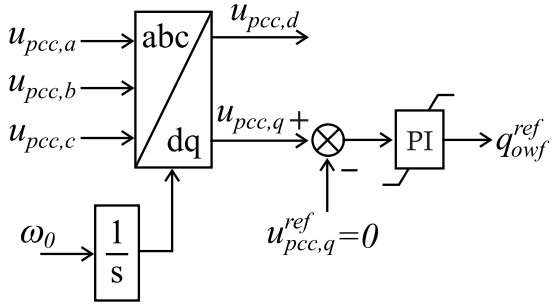

Figure 4.2: Direct frequency controller.

point in these two equations. If the first equation is linearized, the result is as follows:

$$\frac{b_c u_{pcc0}}{\omega_0}\frac{d\Delta u_{pcc}}{dt} + k_{p,link}\Delta u_{pcc} = \Delta p_{owf} \tag{4.1}$$

where $k_{p,link}\Delta u_{pcc} = \Delta p_r$ is derived following. The Kirchhoff voltage law considered in the HVDC link in Figure 4.1 is shown in (4.2). By multiplying all its terms by the DC current, the value of this current i_{dc} can be obtained and it is shown in (4.3). Then, the combination of (2.15) (zero α because of diodes) and (4.3) leads to the expression in (4.4). Finally, the small-signal increments considered in (4.4) lead to the equation (4.5), where $k_{p,link}$ is addressed. Note that the constant DC voltage operation mode of the inverter eliminates Δv_{di}.

$$v_{di} + r_{dc}i_{dc} - v_{dr} = 0 \quad \rightarrow \quad r_{dc}i_{dc}^2 + v_{di}i_{dc} - \underbrace{v_{dr}i_{dc}}_{p_r} = 0 \tag{4.2}$$

$$i_{dc} = -\frac{v_{di}}{2r_{dc}} + \frac{\sqrt{v_{di}^2 + 4r_{dc}p_r}}{2r_{dc}} \tag{4.3}$$

$$u_{pcc} = v_{di} + (r_\mu + r_{dc})i_{dc} = v_{di} + (r_\mu + r_{dc})\left(-\frac{v_{di}}{2r_{dc}} + \frac{\sqrt{v_{di}^2 + 4r_{dc}p_r}}{2r_{dc}} \right) \tag{4.4}$$

$$\Delta u_{pcc} = \frac{\Delta p_r}{k_{p,link}} \quad \rightarrow \quad \Delta p_r = k_{p,link}\Delta u_{pcc} \quad ; \quad k_{p,link} = \frac{\sqrt{v_{di}^2 + 4r_{dc}p_{r0}}}{r_{dc} + r_\mu} \tag{4.5}$$

According to (4.1), the complete transmission of the active power by the HVDC link is demonstrated in steady-state, given Δp_r=Δp_{owf}. It is also demonstrated that the PCC voltage magnitude and the active power increment Δp_{owf} are related by a first order transfer function. Furthermore, this transfer function gain establishes that just a small increment of the voltage magnitude is achieved by a large active-power increment. The block diagram which corresponds to (4.1) is shown in Figure 4.3.

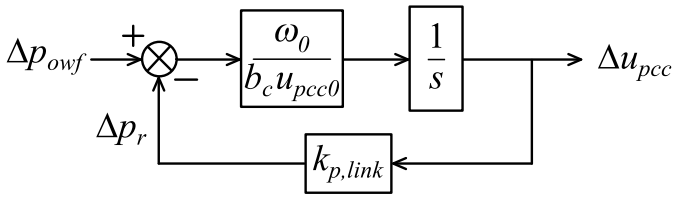

Figure 4.3: Block diagram of the relation between the active-power increment and the PCC voltage magnitude increment.

The independent input of the system in Figure 4.1 is p_{owf}. Thus, this study analytically demonstrates why the voltage magnitude does not need to be controlled. It is clamped between two limits which correspond to maximum and minimum active power transmitted through the HVDC link.

If the second dynamic equation $\left(\frac{b_c u_{pcc}^2}{\omega_0}\frac{d\delta}{dt}=-q_{owf}+q_r-q_c\right)$ is now linearized, the term Δq_{owf} should be considered. Its equation can be obtained from the DFC strategy shown in Figure 4.2. This equation uses the equation of $\Delta u_{pcc,q}$ in (3.8) and it is presented in (4.6). Note that k_p^{dfc} and k_i^{dfc} are the proportional and integral parameters of the PI controller in Figure 4.2.

$$\Delta q_{owf} = u_{pcc0}\left(k_p^{dfc}\Delta\delta + k_i^{dfc}\omega_0\int\Delta\delta dt\right) \tag{4.6}$$

The linearization leads to the equation in (4.7).

$$\frac{b_c u_{pcc0}}{\omega_0^2}\frac{d^2\Delta\delta}{dt^2} + \frac{k_p^{dfc}}{\omega_0}\frac{d\Delta\delta}{dt} + k_i^{dfc}\Delta\delta = \frac{k_{q,link} - 2b_c u_{pcc0}}{b_c u_{pcc0}}(\Delta p_{owf} - k_{p,link}\Delta u_{pcc}) \tag{4.7}$$

where $k_{q,link}$ is derived from (2.15), (2.18), (2.20), (2.21), (4.4) and (4.5) as follows:

$$\Delta q_r = \tan\varphi_0\Delta p_r + \frac{p_{r0}}{\cos^2\varphi_0}\Delta\varphi = \tan\varphi_0\Delta p_r + \frac{k_{\alpha,\mu}u_{pcc0}\cos\varphi_0 i_{dc0}}{\cos^2\varphi_0}\Delta\varphi \tag{4.8}$$

$$\Delta\varphi = \frac{\frac{r_\mu \overbrace{\Delta i_{dc}}^{\frac{\Delta u_{pcc}}{r_{dc}+r_\mu}}}{u_{pcc0}} - \frac{r_\mu i_{dc0}\Delta u_{pcc}}{u_{pcc0}^2}}{k_{\alpha,\mu}\sin\varphi_0} = \frac{r_\mu\left(\frac{1}{u_{pcc0}(r_\mu + r_{dc})} - \frac{i_{dc0}}{u_{pcc0}^2}\right)\Delta u_{pcc}}{k_{\alpha,\mu}\sin\varphi_0} \tag{4.9}$$

$$\Delta q_r = \underbrace{\left(\tan\varphi_0 k_{p,link} + \frac{2i_{dc0}r_\mu v_{di}}{u_{pcc0}(r_{dc}+r_\mu)\sin(2\varphi_0)}\right)}_{k_{q,link}}\Delta u_{pcc} = k_{q,link}\Delta u_{pcc} \tag{4.10}$$

It is worth noting the similarity between (4.7) and the synchronous-generator swing equation. This equation, which results from the study of the synchronous-generator

classical model connected to an infinite bus [3], is as follows:

$$\frac{2H}{\omega_0}\frac{d^2\Delta\delta'}{dt^2} + \frac{k_D}{\omega_0}\frac{d\Delta\delta'}{dt} + k_S\Delta\delta' = \Delta p_m \tag{4.11}$$

where H represents the inertia constant, k_D is the damping torque coefficient and $k_S{=}\dfrac{e'_0 u_\infty \cos\delta'_0}{x_{eq}}$ is the synchronizing torque coefficient. δ' and e' are the generator internal voltage angle and magnitude, respectively, and the infinite bus voltage has zero angle and magnitude u_∞. x_{eq} represents the total reactance between the infinite bus and the generator internal bus and p_m represents the mechanical power provided to the generator.

The comparison of (4.7) and (4.11) yields that the independent term of both equations is a function of the power input of the corresponding system, given the relation in (4.1). Furthermore, several assignments between the other terms can be established as follows:

$$H = \frac{b_c u_{pcc0}}{2\omega_0} \tag{4.12}$$

$$k_D = k_p^{dfc} \tag{4.13}$$

$$k_S = k_i^{dfc} \tag{4.14}$$

According to (4.12), the inertia of the system in Figure 4.1 is provided by the capacitor bank with susceptance b_c. Nevertheless, the inertia of the synchronous generator is of a higher magnitude order than the one in the system. In (4.13) and (4.14), it is demonstrated that the system DFC PI controller gains k_p^{dfc} and k_i^{dfc} provide equivalent damping and synchronizing components, respectively. The ability of the DFC to align the capacitor bank voltage vector alog the dq synchronous reference frame is proved by the equivalent synchronizing component. It is worth mentioning that the damping coefficient of a synchronous generator is lower than the value of k_p^{dfc}. Thus, the system with the DFC is well damped.

4.2.2 Reactive power sharing strategy

The advantages and the need of an equal reactive power level for the WTGSs of the OWF (QSS) are justified in this subsection. The OWF layout presented in Figure 4.4 is used for this study.

The WTGSs in Figure 4.4 (225 MW rated power each one) are modeled as a power injection (p_k and q_k). Each of the WTGSs is connected to the PCC bus through and inductive line (x_k which considers both the line and the transformer short-circuit reactances). The current injected is denoted by its dq components $i_{k,d}$ and $i_{k,q}$ and the

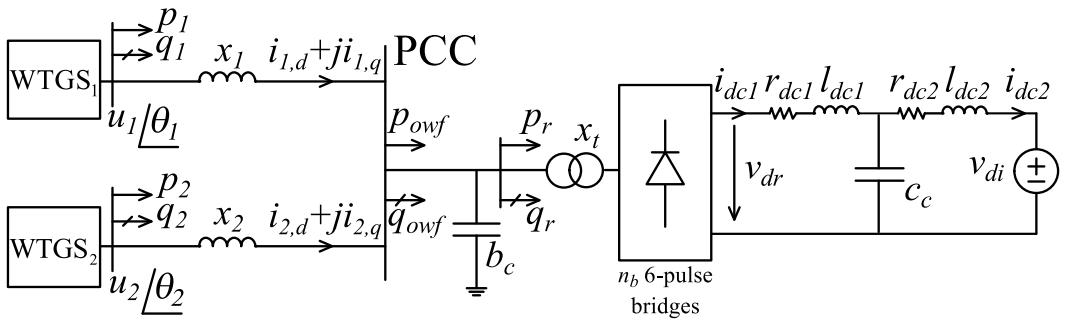

Figure 4.4: OWF equivalent with two aggregated WTGSs and an HVDC composed of a T-modeled cable, the inverter and a diode rectifier.

WTGS terminal voltage magnitude and angle are u_k and θ_k, respectively. Therefore, p_k and q_k are the active and reactive powers injected by the WTGS, respectively. The total active and reactive powers incoming from the OWF to the PCC bus are addressed as p_{owf} and q_{owf}, respectively. The PCC bus has a capacitor bank connected (with susceptance b_c) which represents the reactive power compensation and the harmonic filters at fundamental frequency [4]. The rectifier and its transformer are represented by means of the classic model presented in Section 2.3.1 and they draw the active and reactive powers p_r and q_r, accordingly. The HVDC link is modeled using the inverter DC source and the T-modeled cable which have been presented in Section 2.2.

A static study of the OWF layout in Figure 4.4 is analyzed in this subsection. The steady-state point studied considers the PCC bus voltage vector the angle reference. Thus, the PCC voltage vector in steady-state is $\underline{\boldsymbol{u}_{\boldsymbol{pcc0}}}=\underline{u_{pcc0}\angle 0^\circ}$ and the values of p_{10} and p_{20} are known. Given that there are no losses in the offshore grid of Figure 4.4, (4.15) can be obtained. Then, equations (2.3), (2.17), (2.18), (2.21) and (4.4) can be used considering r_{dc}=r_{dc1}+r_{dc2} in order to get the values of u_{pcc0}, $i_{1,d0}$, $i_{2,d0}$ and q_{r0}. Then, (4.16) can be used to obtain the value of q_{owf0} and (4.17) can be used to get the values of the q component of the WTGSs voltage vectors because of the zero angle of $\underline{\boldsymbol{u}_{\boldsymbol{pcc0}}}$.

$$p_{owf0} = p_{r0} = p_{10} + p_{20} = u_{pcc0}i_{1,d} + u_{pcc0}i_{2,d} \tag{4.15}$$

$$q_{owf0} = q_{r0} - b_c u_{pcc0}^2 \tag{4.16}$$

$$u_{k,q0} = x_k i_{k,d0} \qquad (k = 1, 2) \tag{4.17}$$

Therefore, there are six unknown variables: $u_{1,d0}$, $u_{2,d0}$, $i_{1,q0}$, $i_{2,q0}$, q_{10} and q_{20}. However, the system just provides five additional equations which are as follows:

$$q_{k0} = u_{k,q0} i_{k,d0} - u_{k,d0} i_{k,q0} \qquad (k = 1, 2) \tag{4.18}$$

$$u_{k,d0} = u_{pcc0} - x_k i_{k,q0} \qquad (k = 1, 2) \tag{4.19}$$

$$q_{owf0} = -u_{pcc0}(i_{1,q0} + i_{2,q0}) \tag{4.20}$$

This implies that the other variables can be obtained once one of them is fixed or an additional equation is considered. This means that if the reactive power level of one WTGS is predetermined, the reactive power level of the other must be the one which is required to close the reactive power balance at the PCC bus. This approach is not robust because the reactive power limits of the WTGSs can be easily exceeded. Actually, the application of this study to a system with more than two WTGSs results in being able to set the reactive power level of all the WTGSs except one of them, which would close the reactive power balance at the PCC bus.

Therefore, an additional equation provided by some strategy must be considered to avoid a single unit closing the reactive power balance. The study of this strategy is carried out for the system in Figure 4.4, whose parameters are detailed in Table 4.1.

Table 4.1: Parameters of the OWF layout with two-aggregated WTGSs used in the decentralized frequency control studies.

Parameter	**Value**
Base	f_0=50 Hz ; $S_{base,AC}$=450 MVA ; $V_{base,AC}$=220 kV
n_b	2 six-pulse bridges
x_t/n_b	0.12 p.u.
b_c	0.2 p.u.
r_{dck}	0.003186 p.u.=2.5 Ω $(k = 1, 2)$
l_{dck}	0.2 p.u.=0.5 H $(k = 1, 2)$
c_c	6.409 p.u.=26 μF
c_{dc}	0.15 p.u. of WTGS base
x_f	0.15 p.u. of WTGS base
b_f	0.05 p.u. of WTGS base
x_k	0.13 p.u. $(k = 1, 2)$
v_{di}	0.9654 p.u.

The reactive power level of $WTGS_2$ (q_{20}) is studied for a sweep of the active powers produced (p_{10} and p_{20}) from 0.01 p.u. to 1 p.u. with diverse reactive power strategies applied in $WTGS_1$. Particularly, the strategies tested for $WTGS_1$ are unitary power factor (PF), PF equal to 0.95 leading and lagging, and the QSS (q_{10}=q_{20}). The results are obtained by solving equations (2.3), (2.17), (2.18), (2.21), (4.4), (4.15) to (4.20) and

the equation that sets q_{10} according to each of the studied strategies. These results are presented in Figure 4.5, where $WTGS_1$ PF is addressed as PF_1. The WTGS reactive power limits, which are set to PF equal to 0.95 at rated power ($\pm$32.87 %), are also depicted in Figure 4.5. It should be pointed out that the per-unit values shown in the figures along this Thesis consider the WTGS rating as the base power.

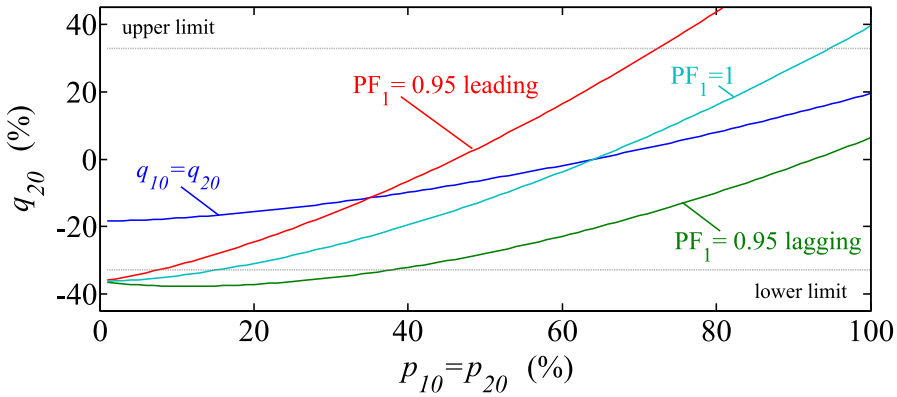

Figure 4.5: Steady-state reactive power level of $WTGS_2$ with diverse reactive power strategies in $WTGS_1$ for a sweep in the active power produced.

The results in Figure 4.5 demonstrate that conventional reactive power strategies are not acceptable because the reactive power limits of the WTGSs would be exceeded. Note that this drawback would be even more pronounced in a real OWF which is composed of a high number of WTGSs. It should be pointed out that the study cases presented in Figure 4.5 lead to voltage magnitudes of the WTGSs (u_{10} and u_{20}) which are between 0.9 p.u. and 1.1 p.u., which are acceptable values [5].

However, the QSS maintains both the WTGSs voltages and reactive power levels within limits. It also provides a single OWF steady-state solution, so it can be considered as the most appropriated reactive power strategy. Actually, it indicates that all the OWF WTGSs are responsible for closing the reactive power balance at the PCC bus, but not only one.

4.3 Decentralized frequency control

The decentralized frequency control proposed in this Thesis is presented in this section. The WTGS control is first detailed. Then, the WTGSs synchronization strategy is described. Finally, the secondary frequency control is also presented because it allows the achievement of a constant frequency control. Proofs of concept of both the decentralized frequency control and the decentralized frequency control with secondary regulation will be also shown in this section. It should be pointed out that the control is performed using the WTGS base $S_{WTGSbase,AC}$.

4.3.1 WTGS control

The WTGS model is the one which has been presented in Section 2.4 and can be seen in Figure 4.6. The WTGS input is the power incoming from the BEC and its FEC control is detailed in Figure 4.6. The diverse three phase voltage and current vectors are transformed into the DQ synchronous frame of the WTGS by means of the transformation angle ϕ_k. Then a current controller and a voltage controller are used in order to determine the voltage vector to be applied by the FEC $\underline{v_k}$ which is again transformed into the three-phase system. Moreover, the reactive power ouput of the WTGS is calculated by means of $\underline{i_{ok}}$ and $\underline{u_k}$ (q_k=$u_{k,Q}i_{ok,D}$−$u_{k,D}i_{ok,Q}$).

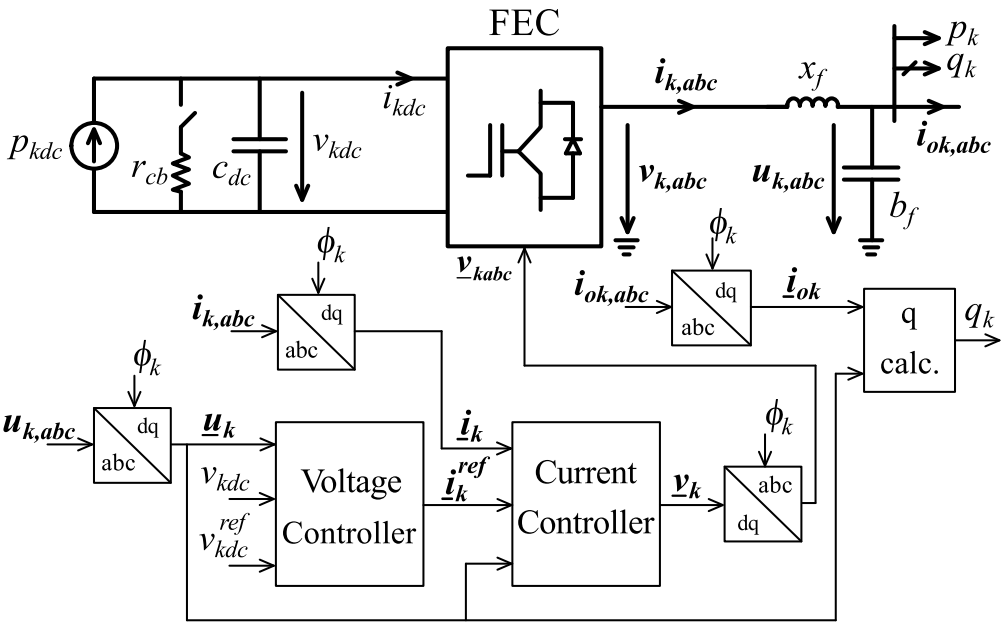

Figure 4.6: WTGS FEC control scheme for the decentralized frequency control.

The WTGS control is based on the DFC which has been addressed in Section 4.2.1. The output voltage vector $\underline{u_k}$ is the voltage vector which is aligned to the DQ synchronous frame of the WTGS. This DQ synchronous frame k rotates at frequency ω_k and has a transformation angle ϕ_k which will be obtained by the synchronization method presented in Section 4.3.2 and Section 4.3.3.

The voltage and current controllers depicted in Figure 4.6 are presented in Figure 4.7. Two control channels can be observed in Figure 4.7. The Q-component channel attempts to align the voltage vector $\underline{u_k}$ with the DQ synchronous frame of the WTGS ($u_{k,Q} = 0$), following the DFC strategy. Then, the $u_{k,Q}$ controller provides the reactive current reference $i_{k,Q}^{ref}$ through PI_v controller. The D-component channel performs the conventional DC voltage control at the FEC in order to supply the incoming power to the FEC DC link. This means maintaining the FEC DC voltage at its reference value v_{kdc}^{ref}. Given that the control can reach zero $u_{k,Q}$ with negative $u_{k,D}$, v_{kdc} error sign is properly adjusted. PI_dc controller provides the active current reference $i_{k,D}^{ref}$ and the

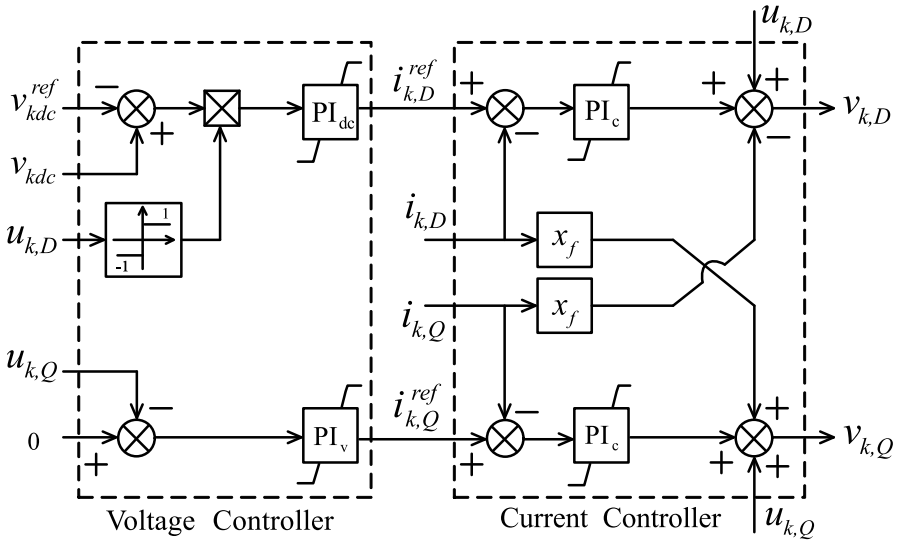

Figure 4.7: Voltage and current controllers of the WTGS FEC control scheme for the decentralized frequency control.

current controllers are PI_c in both control channels. It is worth noting that keeping unchanged the active-power control channel is an objective of this Thesis.

4.3.2 WTGSs synchronous operation control

The OWF layout analyzed in Section 4.2.1 only has a single aggregated WTGS which controls the frequency and the angle. However, an OWF has more than one WTGS and synchronous operation is then required. As it will be shown following, the QSS will produce the right angle differences among the WTGSs bus voltages and, thus, the same frequency.

The WTGSs synchronous operation control strategy is depicted in Figure 4.8. It uses a Q/f droop in order to synchronize all the WTGSs. It is worth noting that ω_0 equals the reference frequency of the system and it is an internal constant value of the WTGS control.

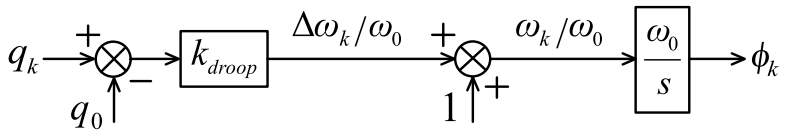

Figure 4.8: WTGSs synchronous operation control scheme of the decentralized frequency control.

The product of the difference $q_k - q_0$ and the constant k_{droop} produces the frequency increment over the reference ω_0. The objective of the QSS, an equal reactive power level of the WTGSs, is achieved by setting the same value for k_{droop} and q_0 in all the WTGSs. During transients, the frequencies will move and the angle differences will be modified until they reach the steady-state. Therefore, this decentralized frequency control is able

to reach WTGSs synchronous operation (same $\Delta\omega_k$) and the right angle differences which lead to the QSS (same q_k) without the need of a communication channel.

It is worth noting that ϕ_k is the DQ transformation angle used in the WTGS control shown in Figure 4.6. Considering that the angle between the stationary system and a reference frame at frequency ω_0 is ϕ_0, ϕ_k=ϕ_0+θ_k (see Figure 4.9). Note that there are two synchronous reference frames in Figure 4.9: the external dq synchronous reference frame which rotates at the reference frequency ω_0 and the internal DQ synchronous frame of the WTGS which rotates at frequency ω_k. The angle between the external and the internal frames is addressed as θ_k, as it can be observed in Figure 4.9. Note that due to the WTGS control strategy based on the DFC, $\underline{\boldsymbol{u_k}}$ is aligned with the DQ synchronous frame.

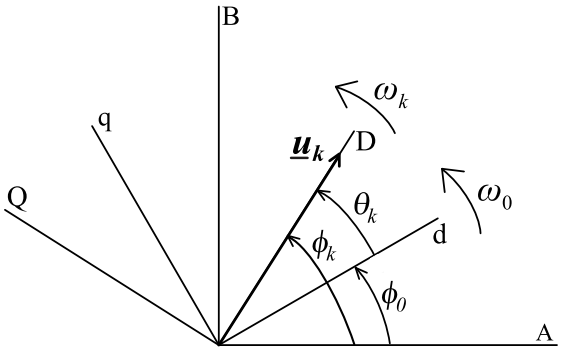

Figure 4.9: Vector diagram of the WTGS voltage vector in the stationary, WTGS DQ synchronous and dq synchronous reference systems.

As a proof of concept, the OWF layout presented in Figure 4.4 is simulated by using the decentralized frequency control strategy. The WTGSs are modeled as it has been described in Section 2.4 and it can be seen in Figure 4.6, but without the crowbar protection. This system is simulated in Matlab/Simulink by considering dynamic models of the WTGSs and the HVDC link, the classic AVM of the rectifier and transformer and the fundamental frequency static model of the grid [6]. The system parameters can be found in Table 4.1 while the control parameters are shown in Table 4.2. The PI controllers are addressed through their proportional gain k and their time constant τ.

Table 4.2: Decentralized frequency control parameters in the WTGS base.

Parameter	**Value**
PI_{dc}	k_{dc}=3.5 p.u. of WTGS base ; τ_{dc}=0.15 s
PI_{v}	k_{v}=1 p.u. of WTGS base ; τ_{v}=0.15 s
PI_{c}	k_{c}=5 p.u. of WTGS base ; τ_{c}=0.005 s
k_{droop}	0.0167 p.u./p.u. of WTGS base
q_0	0 p.u. of WTGS base
k_{sec}	300 p.u. of WTGS base s^{-1}

The simulation is performed with both WTGSs at 0.5 p.u. of initial active power. Active power changes are scheduled t=0.1 s and t=2.5 s. At t=0.1 s, p_{1dc} is increased to 0.75 p.u. and p_{2dc} is decreased to 0 p.u. Then, at t=2.5 s, both WTGS DC powers are increased to 1 p.u.

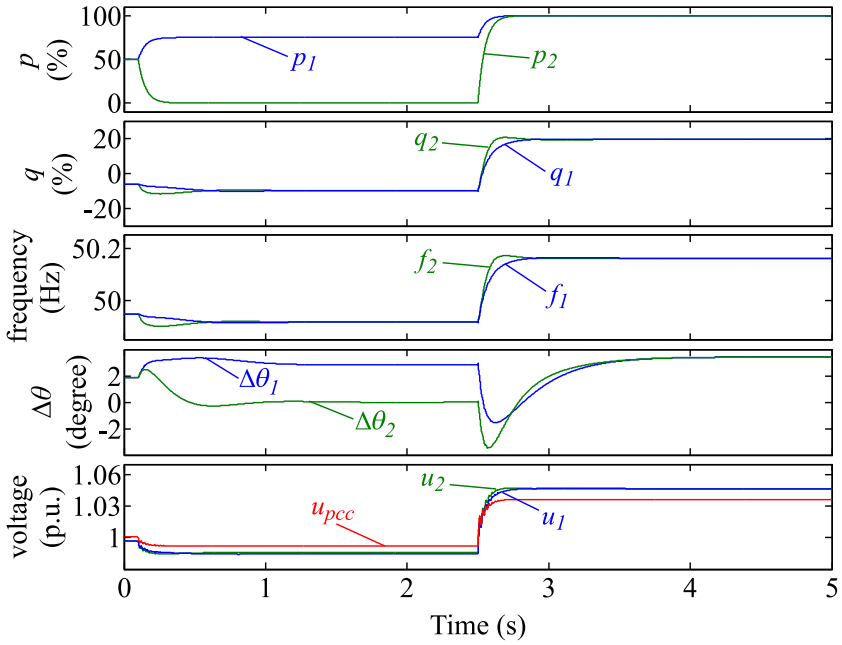

Figure 4.10: WTGSs active and reactive powers, frequency, voltage angle difference and voltage magnitude under active power changes and decentralized frequency control in the two-aggregated WTGSs OWF layout.

These simulation results are shown in Figure 4.10. From top to bottom, active power, reactive power, frequency, voltage angle difference and voltage magnitude of each of the WTGSs are presented. Note that the voltage angle difference is considered between the WTGS terminal voltage and the PCC bus voltage. Moreover, the PCC bus voltage magnitude u_{pcc} is also shown. According to Figure 4.10, WTGSs reach the same reactive power level in steady-state. They also achieve synchronous operation with a frequency deviation which is within acceptable limits [5]. It can be observed that the higher the total active power transmitted through the HVDC link, the higher the voltage magnitudes of the offshore AC grid and the higher the reactive power level of the WTGSs. It is worth noting that these voltage magnitudes are clamped within the range limited by 0.95p.u. and 1.05 p.u. The synchronization method is clarified by Figure 4.10. WTGSs voltage angles change during the transients until the values required by the OWF power flow are achieved, thanks to the slightly different transient frequencies of each WTGS. Therefore, this proof of concept demonstrates the ability of the proposed strategy to satisfactorily achieve the control objectives.

4.3.3 Secondary frequency control

As it has been addressed in Section 4.3.2, the decentralized frequency control leads to OWF frequency deviations. However, a secondary frequency control can be applied in order to maintain constant frequency if it is required, leading to the decentralized frequency control with secondary regulation.

In this secondary regulation, a master WTGS is assigned. It generates a variable reference signal q_0 which is sent to the other WTGSs in order to drive the WTGS frequency ω_k to its reference value ω_0. This control strategy is shown in Figure 4.11. As it can be observed, q_0 is generated through an integral controller with constant k_{sec}. The other WTGSs receive the signal q_0 by means of a communication channel.

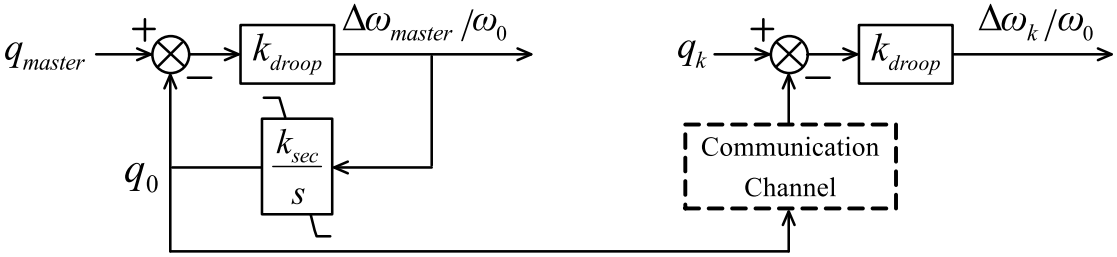

Figure 4.11: Control scheme of the decentralized frequency control with secondary regulation.

As it was previously carried out in Section 4.3.2, the proof of concept is also performed for the decentralized frequency control with secondary regulation. The same simulation is applied to the same system, so the only change is the control strategy, whose parameters can be found in Table 4.2. A time delay of 0.1 s is used to simulate the communication channel and the results are presented in Figure 4.12.

Figure 4.12 shows active power, reactive power, frequency, voltage angle difference and voltage magnitude of each of the WTGSs from top to bottom. As it can be observed in Figure 4.12, the decentralized frequency control with secondary regulation guarantees the synchronous operation and the QSS in steady-state while constant frequency is also achieved. However, this control requires communications among the WTGSs and the dynamics of its results in Figure 4.12 are slower than the ones in Figure 4.10. This is due to the integral secondary control together with the communication delay.

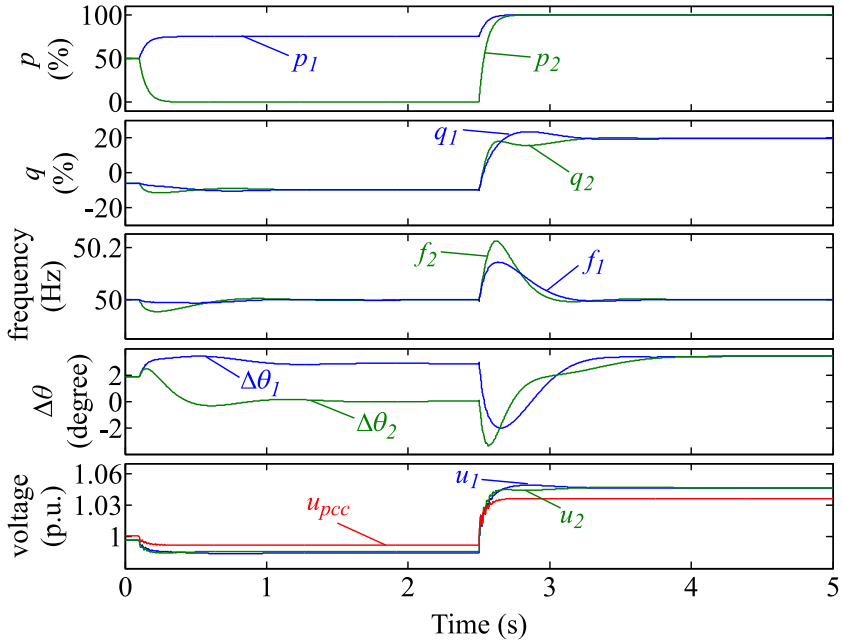

Figure 4.12: WTGSs active and reactive powers, frequency, voltage angle difference and voltage magnitude under active power changes and decentralized frequency control with secondary regulation in the two-aggregated WTGSs OWF layout.

4.4 Stability Analysis

The stability analysis of the decentralized frequency control is performed in this section. Specifically, the OWF layout which is considered is the two-aggregated WTGSs equivalent presented in Figure 4.4 which uses the type-4 WTGS presented in Section 2.4. For the sake of simplicity, only the stability analysis of the decentralized frequency control without secondary control will be carried out.

First, the WTGS small-signal model is presented. Then, it will be interconnected through the OWF admittance matrix to the small-signal model of the HVDC link and transformer which has been presented in Section 2.3.1.1.

4.4.1 WTGS small-signal model

The WTGS model is connected to the offshore grid by means of the impedance z_g=r_g+jx_g to a grid bus whose voltage vector is $\underline{\boldsymbol{u}}_{\boldsymbol{g}}$=$u_{g,d}$+$ju_{g,q}$. Given that the reactance x_k=0.13 p.u. represents both the line and the transformer short-circuit impedance, z_g will be considered just the transformer reactance which is 0.12 p.u. while the line reactance 0.01 p.u. remains in the offshore AC grid.

The aforementioned connection consists of the Thévenin equivalent presented in Figure 4.13. Note that it is in the external dq synchronous reference frame of the grid,

given that it is statically considered in this section. Therefore, the model will have transformations from the internal DQ frame to the external dq frame, as shown in Figure 4.9. Moreover, the WTGS control presented in Section 4.3 is performed in the WTGS base $S_{WTGSbase,AC}$, so a base transformation will be considered because the interconnection in Figure 4.13 is carried out at the global base of the grid $S_{base,AC}$.

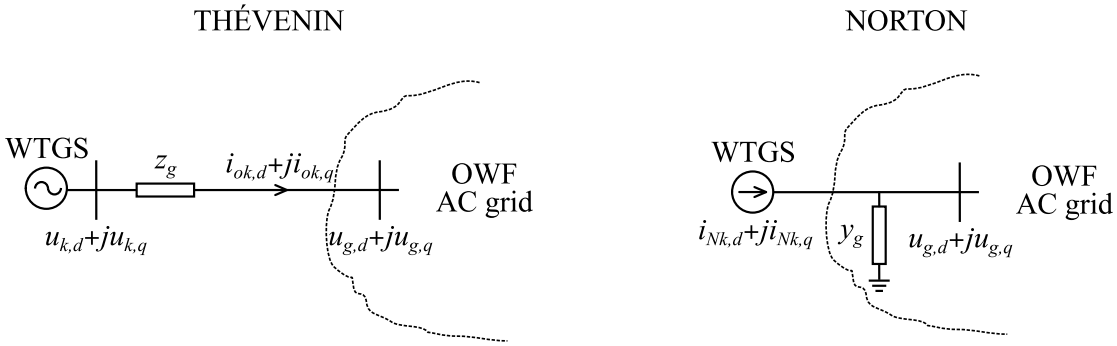

Figure 4.13: Thévenin and Norton equivalents of the WTGS to be connected to the offshore AC grid in the small-signal studies of the decentralized frequency control.

However, the Norton equivalent will be used for the small-signal interconnection. This way, the WTGS model has the grid voltage vector as input and provides the injected current. For this purpose the admittance $y_g{=}\dfrac{1}{z_g}{=}g_g{+}jb_g$ is added to the offshore grid bus and the Norton current injection vector $\underline{\boldsymbol{i}}_{\boldsymbol{Nk}}{=}i_{Nk,d}{+}ji_{Nk,q}$ is considered, as it is shown in Figure 4.13.

Then, the small-signal model can be derived with the aforementioned considerations. Each WTGS has ten states. First five of them correspond to the FEC DC voltage v_{kdc}, the filter current components $i_{k,D}$ and $i_{k,Q}$, and the WTGS voltage components $u_{k,D}$ and $u_{k,Q}$. The other five are derived from the decentralized frequency control presented in Section 4.3.2. These are composed of the angle θ_k and the states of the PI controllers: x_{kdc}, x_{kv}, x_{kcD} and x_{kcQ} for PI_{dc}, PI_{v}, D-channel PI_{c} and Q-channel PI_{c}, respectively. Note that θ_k is decided to be the state instead of ϕ_k, given that they have the same dynamics but θ_k will be used to transform variables between the dq and the DQ synchronous frames.

The inputs of the model are the grid voltage components $u_{g,d}$ and $u_{g,q}$ and the WTGS DC power p_{kdc}. The outputs are the Norton current components $i_{Nk,d}$ and $i_{Nk,q}$ addressed in (4.21).

$$i_{Nk,d} = \frac{S_{WTGSbase,AC}}{S_{base,AC}}\left(\underbrace{(u_{k,D}\cos\theta_k - u_{k,Q}\sin\theta_k)}_{u_{k,d}}g_g - \underbrace{(u_{k,D}\sin\theta_k + u_{k,Q}\cos\theta_k)}_{u_{k,q}}b_g\right)$$

$$i_{Nk,q} = \frac{S_{WTGSbase,AC}}{S_{base,AC}}(u_{k,d}b_g + u_{k,q}g_g) \tag{4.21}$$

The dynamic equations of the model, which are derived from the equations of the reactances, capacitances and the decentralized frequency controllers, are as follows:

$$\frac{dv_{kdc}}{dt} = \frac{\omega_0}{c_{dc}v_{kdc}}(p_{kdc} \underbrace{-v_{k,D}i_{k,D} - v_{k,Q}i_{k,Q}}_{-FEC\ active\ power})$$

$$\frac{di_{k,D}}{dt} = \frac{\omega_0}{x_f}(v_{k,D} - u_{k,D} + x_f i_{k,Q})$$

$$\frac{di_{k,Q}}{dt} = \frac{\omega_0}{x_f}(v_{k,Q} - u_{k,Q} - x_f i_{k,D})$$

$$\frac{du_{k,D}}{dt} = \frac{\omega_0}{b_f}(i_{k,D} - i_{ok,D} + b_f u_{k,Q})$$

$$\frac{du_{k,Q}}{dt} = \frac{\omega_0}{b_f}(i_{k,Q} - i_{ok,Q} - b_f u_{k,D})$$

$$\frac{d\theta_k}{dt} = \omega_0 k_{droop}(\underbrace{u_{k,Q}i_{ok,D} - u_{k,D}i_{ok,Q}}_{q_k} - q_0)$$

$$\frac{dx_{kdc}}{dt} = \frac{k_{dc}}{\tau_{dc}}(v_{kdc} - v_{kdc}^{ref})$$

$$\frac{dx_{kv}}{dt} = \frac{k_v}{\tau_v}(\underbrace{0}_{u_{k,Q}^{ref}} - u_{k,Q})$$

$$\frac{dx_{kcD}}{dt} = \frac{k_c}{\tau_c}\left(\underbrace{k_{dc}(v_{kdc} - v_{kdc}^{ref}) + x_{kdc}}_{i_{k,D}^{ref}} - i_{k,D}\right)$$

$$\frac{dx_{kcQ}}{dt} = \frac{k_c}{\tau_c}\left(\underbrace{k_v(0 - u_{k,Q}) + x_{kv}}_{i_{k,Q}^{ref}} - i_{k,Q}\right) \tag{4.22}$$

where:

$$v_{k,D} = k_c(i_{k,D}^{ref} - i_{k,D}) + x_{kcD} - x_f i_{k,Q} + u_{k,D}$$

$$v_{k,Q} = k_c(i_{k,Q}^{ref} - i_{k,Q}) + x_{kcQ} + x_f i_{k,D} + u_{k,Q}$$

$$i_{ok,D} = (u_{k,D} \underbrace{-u_{g,d}\cos\theta_k - u_{g,q}\sin\theta_k}_{-u_{g,D}})g_g - (u_{k,Q} \underbrace{+u_{g,d}\sin\theta_k - u_{g,q}\cos\theta_k}_{-u_{g,Q}})b_g$$

$$i_{ok,Q} = (u_{k,D} - u_{g,D})b_g + (u_{k,Q} - u_{g,Q})g_g \tag{4.23}$$

Therefore, the WTGS small-signal model can be obtained and it is shown in (4.24). Its inputs, outputs and states are $\boldsymbol{\Delta u}$=$[\Delta u_{g,d}, \Delta u_{g,q}, \Delta p_{kdc}]^{\mathsf{T}}$, $\boldsymbol{\Delta y}$=$[\Delta i_{Nk,d}, i_{Nk,q}]^{\mathsf{T}}$ and $\boldsymbol{\Delta x}$=$[\Delta v_{kdc}, \Delta i_{k,D}, \Delta i_{k,Q}, \Delta u_{k,D}, \Delta u_{k,Q}, \Delta\theta_k, \Delta x_{kdc}, \Delta x_{kv}, \Delta x_{kcD}, \Delta x_{kcQ}]^{\mathsf{T}}$, respectively.

$$\frac{d\boldsymbol{\Delta x}}{dt} = \boldsymbol{A}\boldsymbol{\Delta x} + \boldsymbol{B}\boldsymbol{\Delta u}$$

$$\boldsymbol{\Delta y} = \boldsymbol{C}\boldsymbol{\Delta x} + \boldsymbol{D}\boldsymbol{\Delta u} \tag{4.24}$$

where $\boldsymbol{A}$, $\boldsymbol{B}$, $\boldsymbol{C}$ and $\boldsymbol{D}$ are as follows:

$$\boldsymbol{A} = \begin{bmatrix} a_{11} & a_{12} & a_{13} & a_{14} & a_{15} & 0 & a_{17} & a_{18} & a_{19} & a_{110} \\ a_{21} & a_{22} & 0 & 0 & 0 & 0 & a_{27} & 0 & a_{29} & 0 \\ 0 & 0 & a_{33} & 0 & a_{35} & 0 & 0 & a_{38} & 0 & a_{310} \\ 0 & a_{42} & 0 & a_{44} & a_{45} & a_{46} & 0 & 0 & 0 & 0 \\ 0 & 0 & a_{53} & a_{54} & a_{55} & a_{56} & 0 & 0 & 0 & 0 \\ 0 & 0 & 0 & a_{64} & a_{65} & a_{66} & 0 & 0 & 0 & 0 \\ a_{71} & 0 & 0 & 0 & 0 & 0 & 0 & 0 & 0 & 0 \\ 0 & 0 & 0 & 0 & a_{85} & 0 & 0 & 0 & 0 & 0 \\ a_{91} & a_{92} & 0 & 0 & 0 & 0 & a_{97} & 0 & 0 & 0 \\ 0 & 0 & a_{103} & 0 & a_{105} & 0 & 0 & a_{108} & 0 & 0 \end{bmatrix}$$

$$\boldsymbol{B} = \begin{bmatrix} 0 & 0 & b_{13} \\ 0 & 0 & 0 \\ 0 & 0 & 0 \\ b_{41} & b_{42} & 0 \\ b_{51} & b_{52} & 0 \\ b_{61} & b_{62} & 0 \\ 0 & 0 & 0 \\ 0 & 0 & 0 \\ 0 & 0 & 0 \\ 0 & 0 & 0 \end{bmatrix}$$

$$\boldsymbol{C} = \begin{bmatrix} 0 & 0 & 0 & c_{14} & c_{15} & c_{16} & 0 & 0 & 0 & 0 \\ 0 & 0 & 0 & c_{24} & c_{25} & c_{26} & 0 & 0 & 0 & 0 \end{bmatrix}$$

$$\boldsymbol{D} = \begin{bmatrix} 0 & 0 & 0 \\ 0 & 0 & 0 \end{bmatrix} \tag{4.25}$$

where the non-defined terms are as follows:

$$a_{11} = \frac{-\omega_0}{c_{dc} v_{kdc0}} k_c k_{dc} i_{k,D0}$$

$$a_{12} = \frac{\omega_0}{c_{dc} v_{kdc0}} (k_c i_{k,D0} - v_{k,D0} - x_f i_{k,Q0})$$

$$a_{13} = \frac{\omega_0}{c_{dc} v_{kdc0}} (k_c i_{k,Q0} - v_{k,Q0} + x_f i_{k,D0})$$

$$a_{14} = \frac{-\omega_0}{c_{dc} v_{kdc0}} i_{k,D0} = a_{19} = \frac{a_{17}}{k_c}$$

$$a_{15} = \frac{-\omega_0}{c_{dc} v_{kdc0}} (i_{k,Q0}(1 - k_c k_v))$$

$$a_{18} = \frac{-\omega_0}{c_{dc} v_{kdc0}} k_c i_{k,Q0} = k_c a_{110}$$

$$a_{21} = \frac{\omega_0}{x_f} k_c k_{dc} = -k_{dc} a_{22} = k_{dc} a_{27} = k_c k_{dc} a_{29}$$

$$a_{33} = \frac{-\omega_0}{x_f} k_c = \frac{a_{35}}{k_v} = -a_{38} = -k_c a_{310}$$

$$a_{42} = \frac{\omega_0}{b_f} = \frac{-a_{44}}{g_g} = \frac{a_{45}}{b_c + b_g} = \frac{-a_{46}}{\left(\frac{\partial i_{ok,D}}{\partial \theta_k}\right)_0}$$

$$a_{53} = \frac{\omega_0}{b_f} = \frac{-a_{55}}{g_g} = \frac{-a_{54}}{b_c + b_g} = \frac{-a_{56}}{\left(\frac{\partial i_{ok,Q}}{\partial \theta_k}\right)_0}$$

$$a_{64} = \omega_0 k_{droop} (-i_{ok,Q0} + u_{k,Q0} g_g - u_{k,D0} b_g)$$

$$a_{65} = \omega_0 k_{droop} (i_{ok,D0} - u_{k,Q0} b_g - u_{k,D0} g_g)$$

$$a_{66} = \omega_0 k_{droop} \left(u_{k,Q0} \left(\frac{\partial i_{ok,D}}{\partial \theta_k}\right)_0 - u_{k,D0} \left(\frac{\partial i_{ok,Q}}{\partial \theta_k}\right)_0 \right)$$

$$a_{71} = \frac{k_{dc}}{\tau_{dc}}$$

$$a_{85} = \frac{-k_v}{\tau_v}$$

$$a_{91} = \frac{k_c}{\tau_c} k_{dc} = -k_{dc} a_{92} = k_{dc} a_{97} = -k_{dc} a_{103} = k_{dc} a_{108} = \frac{-k_{dc}}{k_v} a_{105}$$

$$b_{13} = \frac{\omega_0}{c_{dc} v_{kdc0}}$$

$$b_{41} = \frac{\omega_0}{b_f}(g_g \cos\theta_{k0} + b_g \sin\theta_{k0})$$

$$b_{42} = \frac{\omega_0}{b_f}(g_g \sin\theta_{k0} - b_g \cos\theta_{k0})$$

$$b_{51} = \frac{\omega_0}{b_f}(b_g \cos\theta_{k0} - g_g \sin\theta_{k0})$$

$$b_{52} = \frac{\omega_0}{b_f}(b_g \sin\theta_{k0} + g_g \cos\theta_{k0})$$

$$b_{61} = \omega_0 k_{droop}\Big(u_{k,Q0}(-g_g \cos\theta_{k0} - b_g \sin\theta_{k0}) - u_{k,D0}(-b_g \cos\theta_{k0} + g_g \sin\theta_{k0})\Big)$$

$$b_{62} = \omega_0 k_{droop}\Big(u_{k,Q0}(-g_g \sin\theta_{k0} + b_g \cos\theta_{k0}) - u_{k,D0}(-b_g \sin\theta_{k0} - g_g \cos\theta_{k0})\Big)$$

$$c_{14} = k_{base}(g_g \cos\theta_{k0} - b_g \sin\theta_{k0})$$

$$c_{15} = k_{base}(-g_g \sin\theta_{k0} - b_g \cos\theta_{k0})$$

$$c_{16} = k_{base}\Big((-u_{k,D0} \sin\theta_{k0} - u_{k,Q0} \cos\theta_{k0})g_g - (u_{k,D0} \cos\theta_{k0} - u_{k,Q0} \sin\theta_{k0})b_g\Big)$$

$$c_{24} = k_{base}(b_g \cos\theta_{k0} + g_g \sin\theta_{k0})$$

$$c_{25} = k_{base}(-b_g \sin\theta_{k0} + g_g \cos\theta_{k0})$$

$$c_{26} = k_{base}\Big((-u_{k,D0} \sin\theta_{k0} - u_{k,Q0} \cos\theta_{k0})b_g + (u_{k,D0} \cos\theta_{k0} - u_{k,Q0} \sin\theta_{k0})g_g\Big) \quad (4.26)$$

where:

$$\left(\frac{\partial i_{ok,D}}{\partial \theta_k}\right)_0 = (u_{g,d0} \sin\theta_{k0} - u_{g,q0} \cos\theta_{k0})g_g - (u_{g,d0} \cos\theta_{k0} + u_{g,q0} \sin\theta_{k0})b_g$$

$$\left(\frac{\partial i_{ok,Q}}{\partial \theta_k}\right)_0 = (u_{g,d0} \sin\theta_{k0} - u_{g,q0} \cos\theta_{k0})b_g - (u_{g,d0} \cos\theta_{k0} + u_{g,q0} \sin\theta_{k0})g_g$$

$$k_{base} = \frac{S_{WTGSbase,AC}}{S_{base,AC}} \quad (4.27)$$

4.4.2 OWF layout small-signal model

The small-signal models of the WTGS and the HVDC link and transformer which have been presented in Section 4.4.1 and Section 2.3.1.1, respectively, are used to build the small-signal model of the two-aggregated WTGSs OWF layout. For this purpose,

the aforementioned models are interconnected by using the admittance matrix of the grid, as it is established in [3]. The only requirement is that the small-signal models need the terminal voltage as input and the injected current as output. Moreover, the grid admittance matrix must be modified in the WTGSs buses due to the Norton equivalent considered, as it has been stated in Section 4.4.1.

The WTGS small-signal model has 10 state variables while the HVDC link one has 3 state variables. Therefore, the global system has 23 state variables. This small-signal model depends on the active power injection of each of the two WTGSs. It has been checked that the eigenvalues stability criterion is satisfied for all the possible combinations of active powers generated by the WTGSs by sampling each of them in 100 1%-intervals from 1 % to 100 %. However, the number of combinations is really high to show these results. For the sake of clarity, a specific part of the previous study is shown here, where both WTGSs are generating the same active power. These results are presented in Figure 4.14, where the arrow indicates the color code used for the generated active power increment.

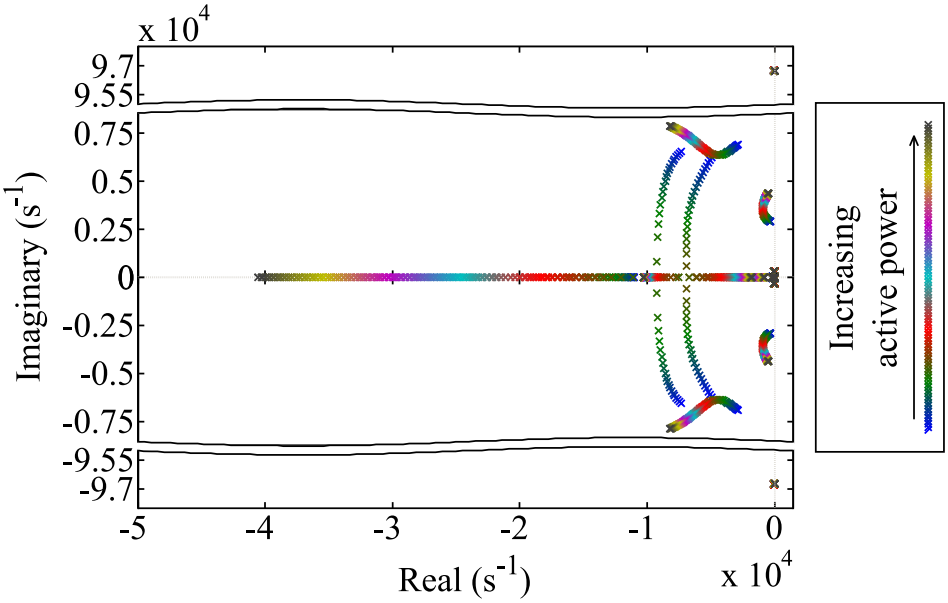

Figure 4.14: Eigenvalues of the two-aggregated WTGSs OWF layout with the decentralized frequency control for diverse active power levels (arrow indicates increasing the active power generated).

As it can be observed in Figure 4.14, the system is stable due to the non-positive real part of the eigenvalues. However, the high amount of state variables makes difficult to analyze the system. Therefore, Figure 4.15 shows zoomed views of the most relevant eigenvalues of the system, which are the ones closer to the imaginary axis. Furthermore, the dominant eigenvalues of the state variables which move with the active power increment are also presented in Figure 4.15.

In Figure 4.15a, the dominant state of the eigenvalues which move is the PI_v controller state. The arrows show that the higher the active power generated, the higher

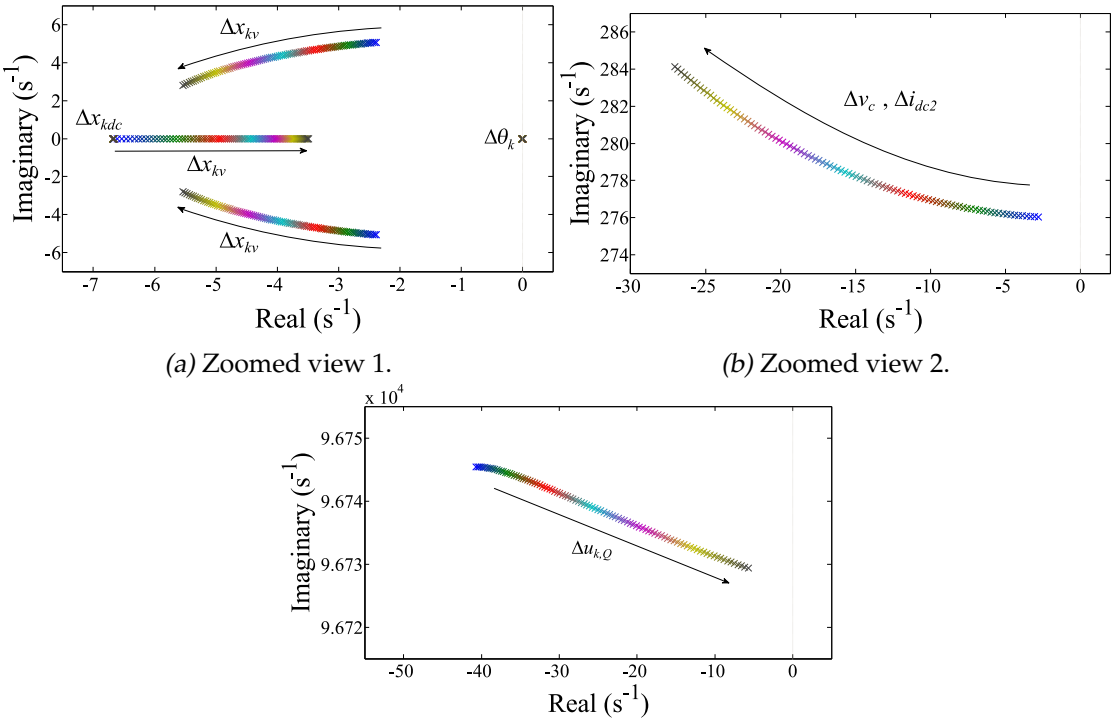

(a) Zoomed view 1.

(b) Zoomed view 2.

(c) Zoomed view 3.

Figure 4.15: Zoomed views of the eigenvalues of the two-aggregated WTGSs OWF layout with the decentralized frequency control for diverse active power levels (arrows indicate increasing the active power generated).

the damping of the complex eigenvalues analyzed there. It should be pointed out that there are two eigenvalues which do not depend of the active power generated in Figure 4.15a. The first one is located at the origin of the system and its dominant state variable is $\Delta\theta_k$. The second one is over the real axis at the position $-6.67\ \mathrm{s}^{-1}$, being its dominant state Δx_{kdc}.

Figure 4.15b and Figure 4.15c show the movement of other two complex eigenvalues when the generated active power is increased. For the sake of clarity, just the positive imaginary eigenvalue is shown in these figures. The two dominant states in Figure 4.15b correspond to the HVDC link (Δv_c and Δi_{dc2}), while the dominant state in Figure 4.15c belongs to the WTGSs ($\Delta u_{k,Q}$). In Figure 4.15b, the damping improves when the active power is increased, with the eigenvalues moving far from the imaginary axis. However, the opposite variation can be observed in Figure 4.15c.

4.5 Simulation results

The OWF model which is used to validate the decentralized control proposal by using a DSM simulation in PSIM is presented in Figure 4.16. It uses the type-4 WTGS model presented in Section 2.4. This OWF layout represents an OWF which has 90

WTGSs rated 5 MW. The WTGSs are distributed in three clusters which have independent line feeders and three strings with 10 WTGSs per string. Each of the aggregated WTGSs is rated 75 MW. T_1 steps up from 0.69 kV to 33 kV which are in turn stepped up to 220 kV by T_2. These transformers are modeled by their short-circuit impedance $r_{Tk} + jx_{Tk}$ (being k the identification number of the transformer). Note that the short-circuit resistance r_t of the diode rectifier transformer has also been considered in this model. π-models are used for the OWF cables and the harmonic filters (filter 1 and filter 2 in Table 4.3) are single tuned filters at the main harmonics of the twelve-pulse rectifier: 11 and 13, respectively. They are tuned considering a reactive power of 13.388 MVAr at fundamental frequency and a quality factor of 1000 [7]. Control parameters can be found in Table 4.2 while the system parameters of the OWF layout in Figure 4.16 are presented in Table 4.3.

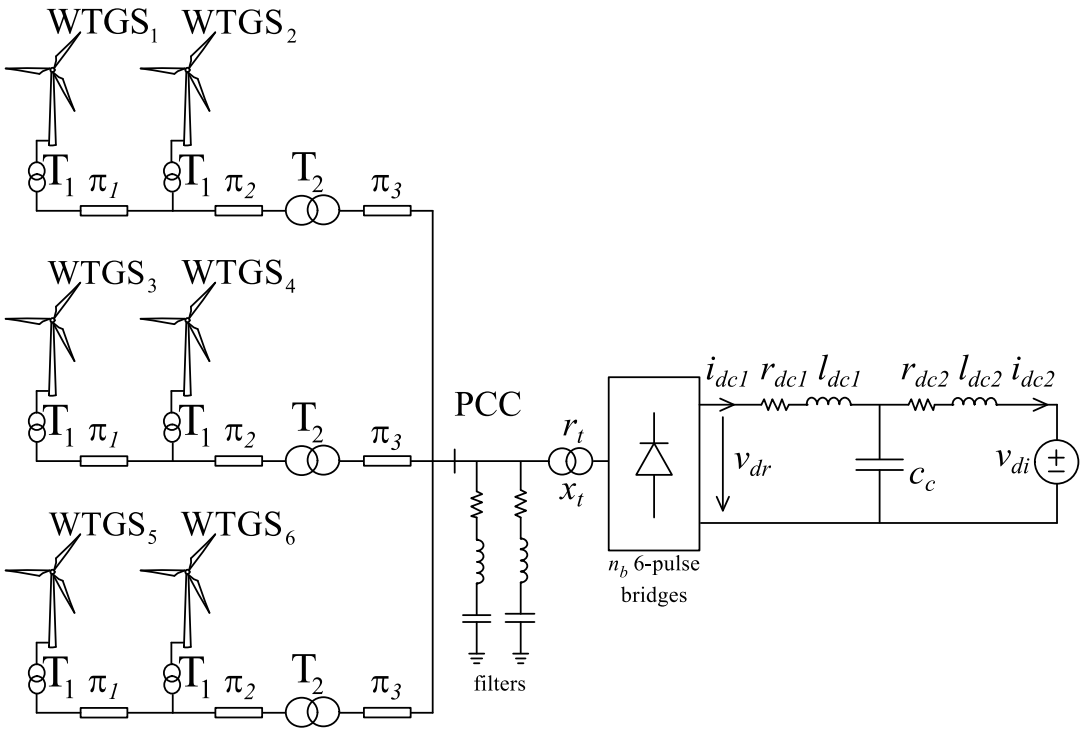

Figure 4.16: OWF equivalent with six aggregated WTGSs and an HVDC composed of a T-modeled cable and a diode rectifier.

Before the simulation, a steady-state analysis is performed to check the operation points. At full load, each WTGS supplies a reactive power of 0.205 p.u. and the offshore AC-grid highest voltage is 1.077 p.u. At low load, the reactive power absorbed by each WTGS is 0.2607 p.u., being 0.9107 p.u. the lowest voltage in the offshore AC-grid. Therefore, the operation points are between acceptable limits [5].

The simulation carries out both the startup and the fault response of the system. For the startup, $WTGS_1$ starts receiving power from the BEC at t=0.1 s with a constant rate of 1 p.u./s. Then, $WTGS_2$ to $WTGS_6$ also startup in the same conditions with a

Table 4.3: Parameters of the OWF layout with six-aggregated WTGSs used in the decentralized frequency control simulation.

Parameter	Value
Base	f_0=50 Hz ; $S_{base,AC}$=450 MVA ; $V_{base,AC}$=220 kV
n_b	2 six-pulse bridges
x_t/n_b	0.12 p.u. (x_t/r_t=80)
r_{dck}	0.003186 p.u.=2.5 Ω ($k = 1, 2$)
l_{dck}	0.2 p.u.=0.5 H ($k = 1, 2$)
c_c	6.409 p.u.=26 μF
c_{dc}	0.15 p.u. of WTGS base
x_f	0.15 p.u. of WTGS base
b_f	0.05 p.u. of WTGS base
r_{cb}	20 mΩ
x_k	0.13 p.u. ($k = 1, 2$)
$x_{T1}/6$	0.07 p.u. of transformer base (x_{T1}/r_{T1}=80)
$x_{T2}/3$	0.1 p.u. of transformer base (x_{T2}/r_{T2}=80)
cable π_1	r=0.02826 p.u. x=0.03038 p.u. b=0.003011 p.u.
cable π_2	r=0.02776 p.u. x=0.0787 p.u. b=0.005237 p.u.
cable π_3	r=0.001882 p.u. x=0.0111 p.u. b=0.0642 p.u.
filter 1	R=0.3286 Ω L=0.0951 H C=0.8805 μF
filter 2	R=0.2774 Ω L=0.0679 H C=0.8805 μF
v_{di}	0.9654 p.u.

0.1-s delay between each WTGS startup. The final operation points reached by the WTGSs after the startup correspond to 0.9 p.u., 0.75 p.u., 0.6 p.u., 0.45 p.u., 0.3 p.u. and 0.15 p.u. from $WTGS_1$ to $WTGS_6$, respectively. At t=2.5 s, a 300-ms fault is scheduled at the PCC bus. During the fault, the incoming active power to the FEC is driven to zero and it is increased with a constant rate of 1 p.u./s once the fault is cleared. Current is controlled during the fault to provide the FRT response of the WTGS. Furthermore, crowbar overvoltage protection is activated when the FEC DC voltage is over 1.25 p.u. and deactivated when it goes under 1.2 p.u. These simulation results are shown in Figure 4.17 and Figure 4.19 for the decentralized frequency control and the decentralized frequency control with secondary regulation, respectively.

After the startup and fault simulation, active power changes are carried out in order to show the control performance when the WTGSs are generating the same amount of active power. Even thoguh this simulation is just the continuation of the previous one, the results are separated in two figures for the sake of clarity. Specifically, from t=5.5 s to t=6.5 s, the WTGSs DC powers are reduced at constant rates until 0.02 p.u. Likewise, the WTGSs DC powers are increased at constant rates until 1 p.u. from t=7.5 s to t=8.5 s.

The corresponding results of this simulation case are shown in Figure 4.18 and Figure 4.20 for the decentralized frequency control and the decentralized frequency control with secondary regulation, respectively.

4.5.1 Decentralized frequency control

The simulation results of the six-aggregated OWF layout with the decentralized frequency control are presented in Figure 4.17. Startup, normal operation and fault response are shown in Figure 4.17. From top to bottom, Figure 4.17 shows the WTGSs active and reactive powers, their FECs DC voltages and the PCC bus frequency and phase voltage. The decentralized frequency control is able to startup the system, provided that the FECs DC buses are fed. A steady-state operation at 49.92 Hz is reached while the WTGSs have the same reactive power level which does not exceed the reactive power limits. The fault response mainly depends on the FEC response to the voltage sag and synchronous operation is recovered after the fault is cleared. The crowbar actuation can be observed in the WTGSs DC voltages during the first milliseconds of the fault. Finally, it is worth mentioning that frequency is measured by means of a PLL in Section 4.5, so it is affected by its dynamics.

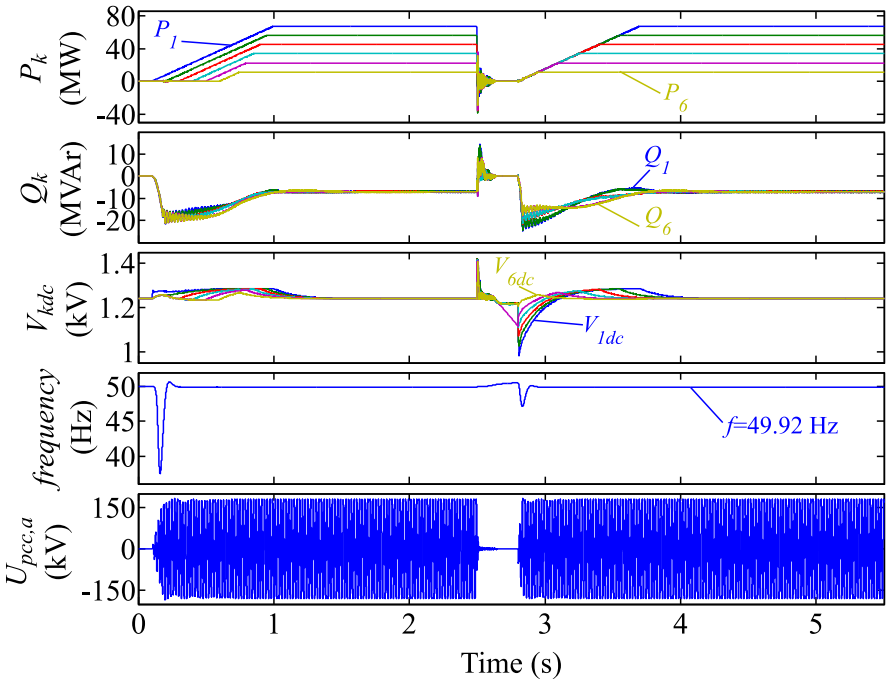

Figure 4.17: WTGSs active power, reactive power and DC-bus voltage, PCC frequency and phase voltage responses to startup procedure and fault under decentralized frequency control in the six-aggregated WTGSs OWF layout. Simulation 1.

After the simulation shown in Figure 4.17, active power changes are performed in the WTGSs. The results are shown in Figure 4.18, which shows the same variables as Figure 4.17. The results in Figure 4.18 show how the offshore AC grid frequency varies

depending on the total active power transmitted through the HVDC link, while this is not evident in Figure 4.17. Moreover, these simulation results indicate the frequency deviation, which is between 49.78 Hz at low load and 50.16 Hz at full load including the transients.

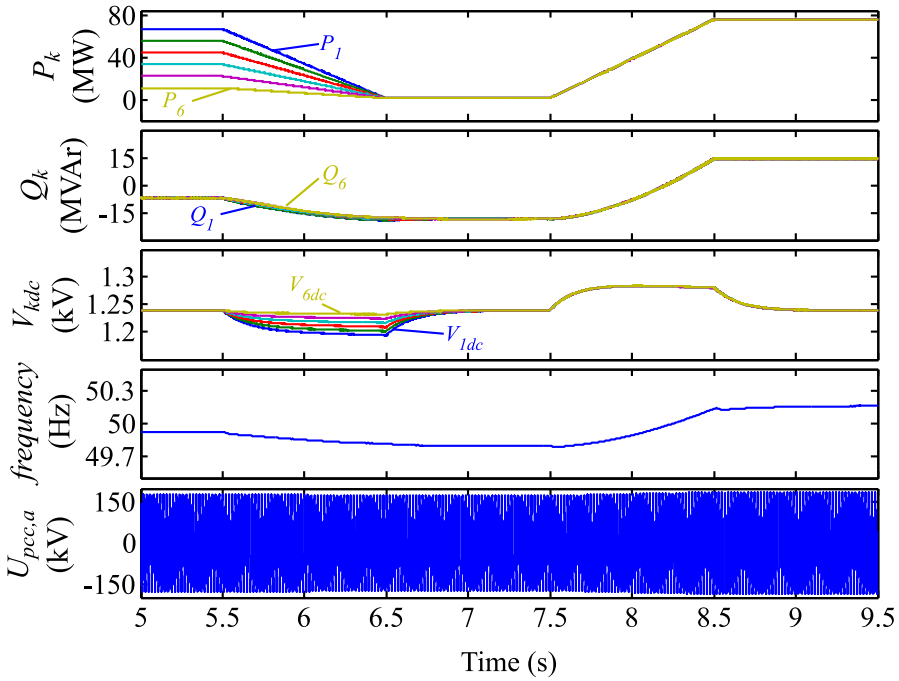

Figure 4.18: WTGSs active power, reactive power and DC-bus voltage, PCC frequency and phase voltage responses to active power changes under decentralized frequency control in the six-aggregated WTGSs OWF layout. Simulation 2.

4.5.2 Decentralized frequency control with secondary regulation

The same simulation that has been performed in Section 4.5.1 is carried out using the decentralized frequency control with secondary regulation. As it was performed in Section 4.3.3, the communication delay is simulated by means of a time delay of 0.1 s and $WTGS_1$ is the master unit. Active and reactive powers, their FECs DC voltages and the PCC bus frequency and phase voltage results are shown in Figure 4.19 from top to bottom. As it can be observed, the frequency is maintained at its reference value 50 Hz after both the startup and the fault. It can be also observed that the system response is slowed down with the secondary frequency control due to the integral action. Finally, the decentralized frequency control with secondary regulation is also able to startup the offshore grid, operate the system and recover voltage once the fault is cleared.

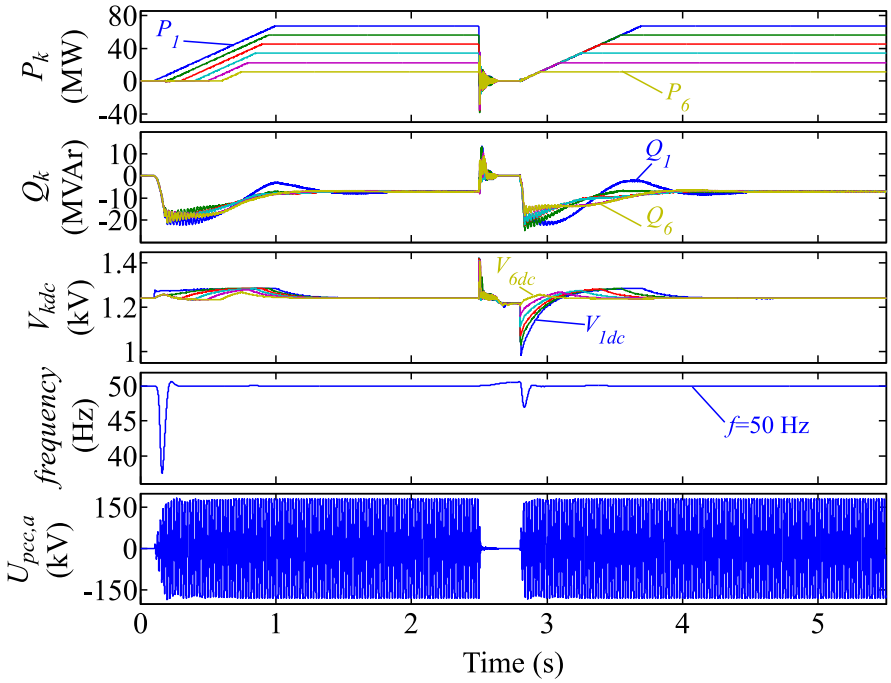

Figure 4.19: WTGSs active power, reactive power and DC-bus voltage, PCC frequency and phase voltage responses to startup procedure and fault under decentralized frequency control with secondary regulation in the six-aggregated WTGSs OWF layout. Simulation 1.

As it was stated in Section 4.5.1, after the startup and fault shown in Figure 4.19, active power changes are performed in the WTGSs DC inputs. This active power changes are the same ones which have been applied in the simulation of Section 4.5.1 but using the decentralized frequency control with secondary regulation. The results in Figure 4.20 demonstrate that frequency is maintained at the reference value in steady-state, by comparing Figure 4.18 and Figure 4.20. Furthermore, results in Figure 4.20 clearly show that the reactive power level of the master WTGS deviates more from the steady-state value than in the other WTGSs. This effect could be expected because the communication delay makes the master WTGS assume a higher reactive power deviation and it can be slightly observed by comparing Figure 4.18 and Figure 4.19.

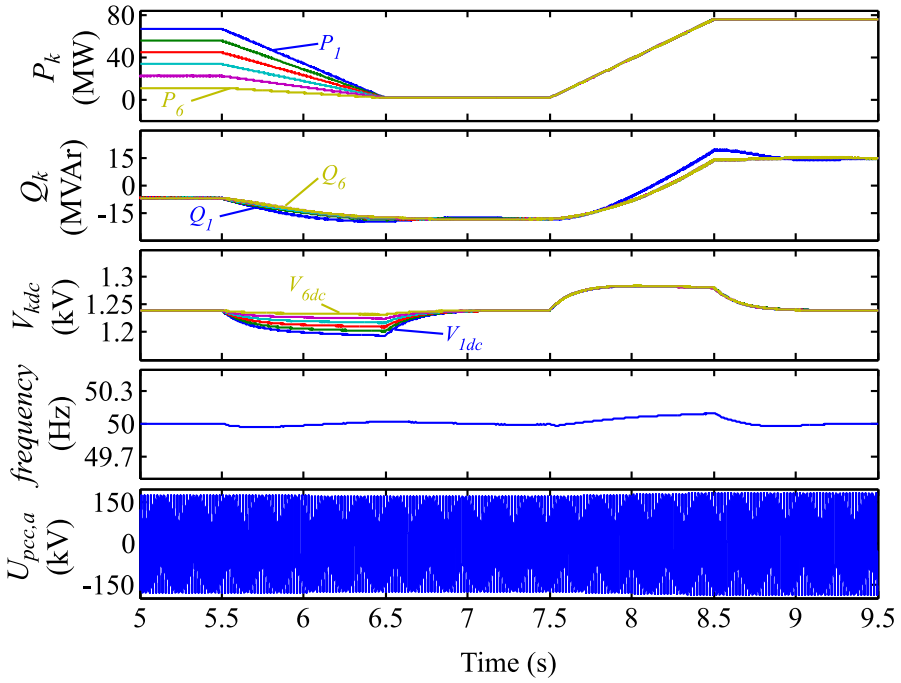

Figure 4.20: WTGSs active power, reactive power and DC-bus voltage, PCC frequency and phase voltage responses to active power changes under decentralized frequency control with secondary regulation in the six-aggregated WTGSs OWF layout. Simulation 2.

4.6 Conclusions

This chapter has presented a decentralized frequency control which allows the synchronous operation of the WTGSs of an OWF which is connected to the onshore grid by means of a diode-rectifier-based HVDC link.

The frequency control is based on the DFC, which aligns the voltage at the WTGS output filter capacitor to an internal frame of the WTGS. This control strategy just uses the WTGS reactive power for this purpose, so its active power control channel remains unchanged, which is one of the specifications of the control system design. Then, the synchronous operation of the WTGSs is achieved by the use of a Q/f droop which synchronizes the WTGSs voltages without the need of communications among the WTGSs. Simultaneously, the Q/f droop strategy leads to an equal reactive power level of the WTGSs of the OWF. This is also an objective of the proposed control strategy in order to avoid the WTGSs exceeding their reactive power limits.

Moreover, the stability of the proposed control has been checked by the analysis of the small-signal model of an OWF equivalent layout. Additionally, a secondary frequency control has also been proposed for constant frequency operation, if required. However, if the Q/f droop gain is properly designed, the frequency deviations are acceptable and this control feature could be avoided, provided that it implies the use of communications among the WTGSs.

Both control proposals have been checked by a DSM simulation in PSIM. Startup, operation and fault response have been simulated and the control performance achieves the control objectives.

Although type-4 WTGSs have been used to validate this control proposal in both the stability and the simulation studies, type-3 WTGSs can be also used. Type-3 WTGSs can be controlled as a voltage source [8] which in turn means that they can behave as type-4 WTGSs. Therefore, this decentralized frequency control could be applied to an OWF based on type-3 WTGSs.

4.7 Bibliography

[1] P Menke et al. "Breakthrough in DC grid access technology for large scale offshore wind farms". In: *EWEA offshore, Copenhagen, Denmark* (2015), pp. 1–5 (cit. on pp. 73, 74).

[2] P Menke et al. "2nd Generation DC Grid Access for Large Scale Offshore Wind Farms". In: *14th International Wind Integration Workshop, Brüssel*. 2015 (cit. on pp. 73, 74).

[3] P. Kundur, N. J. Balu, and M. G. Lauby. *Power system stability and control*. Vol. 7. McGraw-hill New York, 1994 (cit. on pp. 78, 93).

[4] M. Guan et al. "Synchronous generator emulation control strategy for voltage source converter (VSC) stations". In: *IEEE Transactions on Power Systems* 30.6 (2015), pp. 3093–3101 (cit. on p. 79).

[5] E.-E. ENTSO-E. *Network Code for Requirements for Grid Connection Applicable to all Generators*. 2013. URL: `https://www.entsoe.eu/fileadmin/user_upload/_library/resources/RfG/130308_Final_Version_NC_RfG.pdf` (visited on 05/23/2018) (cit. on pp. 81, 85, 95).

[6] L. M. Castro, E. Acha, and C. R. Fuerte-Esquivel. "A novel VSC-HVDC link model for dynamic power system simulations". In: *Electric Power Systems Research* 126 (2015), pp. 111–120 (cit. on p. 84).

[7] Y.-S. Cho and H. Cha. "Single-tuned passive harmonic filter design considering variances of tuning and quality factor". In: *Journal of International Council on Electrical Engineering* 1.1 (2011), pp. 7–13 (cit. on p. 95).

[8] S. Arnaltes, J. L. Rodriguez-Amenedo, and M. E. Montilla-DJesus. "Control of Variable Speed Wind Turbines with Doubly Fed Asynchronous Generators for Stand-Alone Applications". In: *Energies* 11.1 (2017), p. 26 (cit. on p. 101).

Chapter 5

Conclusions

This chapter addresses the main contributions of this Thesis. Then, the original contributions are also described in Section 5.2. Moreover, the diverese publications which have been produced are shown in Section 5.3. Finally, Section 5.4 presents the financing sources which have supported this Thesis.

5.1 General conclusions

This Thesis presents control solutions for the operation of OWFs connected to the onshore grid through an HVDC link with LCC-based rectifier. Due to the advantages in terms of computing time and continuous nature of average-value modeling in power electronics studies, a novel AVM has been used for the control derivation, design and simulation. Actually, an AVM of an LCC-rectifier station has been proposed in Chapter 2, where the modeling of the elements in the system has also been addressed.

The proposed AVM has the WTGS operation variables as inputs: the produced active and reactive powers. Moreover, the state variables are the PCC voltage vector magnitude and angle, which are the variables to be controlled in the OWF to allow the LCC-rectifier operation. These are the main advantages of the proposed AVM, whose dynamic equations show that the active power balance at the PCC bus drives the voltage magnitude variations while the corresponding reactive power balance drives the frequency variations.

Therefore, the proposed AVM allows the derivation of the centralized voltage and frequency control strategy presented in Chapter 3. This centralized control is split

in two categories: the frequency control for a diode-rectifier-based HVDC connection and the voltage and frequency control for a thyristor-rectifier-based HVDC connection. Even though the OWF AC grid voltage magnitude cannot be controlled if the diode rectifier is used, it is demonstrated that it is bounded between acceptable limits according to grid codes.

Since the centralized frequency control derivation, design, stability analysis and simulation are carried out by the proposed AVM, both the proposed model and control are also validated against the results of a DSM implemented in PSIM. This validation is performed considering both the small-signal frequency-domain and the large-signal time-domain responses. Moreover, the appropriate fault response of the controlled systems is checked, being voltage and frequency recovered once the fault is cleared.

A decentralized frequency control has been presented in Chapter 4, which allows the connection of OWFs to the onshore grid through diode-rectifier-based HVDC links. For this purpose, the terminal voltage of each of the WTGSs is aligned with the the internal frame of the corresponding WTGS. Then, the synchronous operation of the WTGSs is achieved by using a Q/f droop. This Q/f droop simultaneously achieves the control objective which consists of reaching an equal reactive power level at the WTGSs without the need of communications among them. The stability of this control proposal has also been checked by small-signal analysis.

The proposed decentralized frequency control produces acceptable frequency deviations. A secondary frequency control is still proposed because it maintains constant frequency by taking advantage of communications among the WTGSs. Both decentralized control proposals are simulated by a DSM in PSIM to check the appropriate startup, operation and fault response performance of the controlled systems.

None of the proposed controls modifies the active power control channel of the WTGSs, which is a specification of the control system. Also, the control proposals do not rely on PLL measurements, so they are not subject to grid disturbances or measurement noise. Moreover, the proposed controls can be applied to both type-3 and type-4 WTGSs, although it has only been tested in type-4 WTGSs. The centralized control proposal should be enhanced in order to have the OWF startup capability, while the decentralized control proposal is able to startup the OWF. Therefore, the objectives of this Thesis have been achieved by the proposals which have been presented.

5.2 Original contributions

The main original contributions of this Thesis are:

- An LCC rectifier substation AVM which includes the AC capacitor bank dynamics and clearly demonstrates that the OWF voltage is driven by the active power balance while the frequency is driven by the reactive power balance.

- Frequency control solutions which do not rely on PLL measurements and remain unchanged the active power control channel of the WTGSs.
- A centralized frequency control solution which allows the operation of the OWF connected to an LCC-rectifier-based HVDC link.
- A decentralized frequency control which simultaneously synchronizes the WTGSs operation and equally shares the OWF reactive power demand among the WTGSs.
- An analytical demonstration of the limited variation of the OWF AC voltage magnitude which indicates that the voltage control is not required and that the power injected to the PCC bus is automatically delivered to the HVDC link.
- Stability studies which demonstrate that the operation with the proposed controls is stable.

5.3 Publications

The diverse publications throughout this Thesis are sorted by the date of publication. They are also separated in three different categories: journal papers, conference papers and patent applications.

5.3.1 Journal papers

- Cardiel-Alvarez, M. A., Rodriguez-Amenedo, J. L., Arnaltes, S., and Montilla-DJesus, M. E. *"Modeling and Control of LCC Rectifiers for Offshore Wind Farms Connected by HVDC Links"*. IEEE Transactions on Energy Conversion, vol. 32, no. 4, pp. 1284-1296, April 2017.
- Cardiel-Alvarez, M. A., Arnaltes, S., Rodriguez-Amenedo, J. L., and Nami, A. *"Decentralized Control of Offshore Wind Farms Connected to Diode-based HVDC Links"*. IEEE Transactions on Energy Conversion, February 2018.

5.3.2 Conference papers

- Rodriguez-Amenedo, J. L., Arnaltes, S., Cardiel-Álvarez, M. Á., and Montilla-DJesus, M. *"Direct Voltage and Frequency Control of an Offshore Wind Farm Connected through LCC-HVDC Link"*. In Power Electronics and Applications (EPE'17 ECCE Europe), 2017 19th European Conference on (pp. 1-10). IEEE, September 2017.

5.3.3 Patent applications

- S. Arnaltes Gómez, J. L. Rodríguez Amenedo, M. Á. Cardiel Álvarez. *"Método para el control distribuido de la frecuencia en un parque eólico offshore"*. Patent Application P201731257, 25/10/2017.

5.4 Funding

The financing sources which have been received during this Thesis are:

- Pre-doctoral research training contract (PIPF) supported by Univerisdad Carlos III de Madrid, from 08/09/2014 to 07/09/2018.
- Mobility Scholarship for researchers in foreign research centers (Industry or Academia) supported by Univerisdad Carlos III de Madrid and ABB AB. Destination: ABB Corporate Research Center, Västerås, Sweden. From 14/08/2017 to 14/01/2018.
- Research project funded by the Spanish Government. Plan Estatal de Investigación :"Integración de la Energía Eólica Marina en el Sistema Eléctrico Español mediante Enlaces de Corriente Continua Multiterminal". ENE2013-47296-C2-1-R, from 01/01/2014 to 31/03/2017.

Acronyms

AC alternating current. xiii, xv, xvii, 4–12, 21, 22, 24–29, 31–33, 35, 37, 38, 42–45, 50–52, 54, 63, 65, 66, 72, 74, 80, 81, 85, 87, 88, 92, 95–97, 104, 105

AVM average-value model. ix, x, xiii, xiv, xvii, 13, 14, 21–27, 31–39, 42–45, 49–52, 63–69, 71, 75, 84, 103, 104

BEC back-end converter. 11, 44, 82, 95

DC direct current. xiii, xiv, 5–12, 22–29, 32, 33, 37, 42–45, 51, 54, 57, 63, 66–71, 74, 76, 79, 82, 85, 88, 96–99

DFC direct frequency control. 74, 75, 77, 78, 82, 84, 100

DFIG doubly-fed induction generator. 4

DRU diode rectifier unit. 12, 74

DSM detailed switching model. xiii, xiv, 14, 22, 23, 42–45, 50, 66–69, 71, 94, 101, 104

EESG electrically excited synchronous generator. 4

FEC front-end converter. xv, 11, 44, 45, 82, 83, 88, 89, 96–98

FRA frequency response analysis. 42, 66

FRT fault ride-through. 4, 69, 96

GPS Global Positioning System. 11, 12

GSC generator-side converter. 11

GTO turn-off thyristor. 5

HVAC high voltage alternating current. ix, xiii, 1, 4, 5

HVDC high voltage direct current. ix–xi, xiii–xv, xvii, 1, 4–9, 11–14, 21–23, 28, 29, 37, 39, 40, 42, 43, 45, 49–54, 57, 59, 61–71, 73, 75–77, 79, 84, 85, 87, 92–95, 98, 100, 103–105

IGBT insulated gate bipolar transistor. 5

LCC line-commutated converter. ix, x, xiii, xiv, xvii, 1, 5–7, 13, 21–28, 31, 32, 37, 39, 42, 43, 45, 49–73, 103–105

LSC line-side converter. 11

MMC modular multilevel converter. 6, 9, 12

MPPT maximum power point tracking. 10

OWF offshore wind farm. ix–xi, xiii–xvii, 1–14, 21, 22, 24, 32, 35, 37, 45, 49–101, 103–105

OWPP offshore wind power plant. 3

P/f droop active-power / frequency droop. 8

P/V droop active-power / voltage droop. 11, 12

PCC point of common coupling. xiii, xiv, 7–11, 24, 26, 27, 31–38, 45, 50–54, 57, 60, 63–65, 68–71, 76–81, 85, 96–98, 103, 105

PF power factor. 80, 81

PI proportional-integral. 7, 51, 53, 56, 57, 60, 77, 78, 82–84, 88, 93

PLL phase-locked loop. 10–12, 52, 69, 71, 97, 104, 105

PMSG permanent magnet synchronous generator. 4

Q/f droop reactive-power / frequency droop. 11, 12, 74, 83, 100, 104

Q/V droop reactive-power / voltage droop. 8, 9

QSS reactive power sharing strategy. 13, 74, 78, 80, 81, 83, 84, 86

RMS root mean square. 26

SCIG squirrel-cage induction generator. 4

STATCOM static compensator. 7, 9, 10, 53

THD total harmonic distortion. xvii, 25

TSO transmission system operator. 3, 4

VOC voltage-oriented control. 8, 10, 11, 52

VSC voltage-source converter. ix, xvii, 1, 5, 6, 8–12, 22

WECS wind-energy conversion system. 4

WECU wind-energy conversion unit. 4

WTGS wind turbine generator system. ix–xi, xiii–xvii, 1, 4, 5, 7–13, 21, 22, 24, 35, 44, 45, 50–54, 69, 73–75, 78–88, 90, 92–101, 103–105